

**HIGH ACCURACY P- $\rho$ -T MEASUREMENTS UP TO 200 MPA  
BETWEEN 200 K AND 500 K USING A COMPACT SINGLE  
SINKER MAGNETIC SUSPENSION DENSIMETER FOR PURE  
AND NATURAL GAS LIKE MIXTURES**

A Dissertation

by

MERT ATILHAN

Submitted to the Office of Graduate Studies of  
Texas A&M University  
in partial fulfillment of the requirements for the degree of

DOCTOR OF PHILOSOPHY

August 2007

Major Subject: Chemical Engineering

**HIGH ACCURACY P- $\rho$ -T MEASUREMENTS UP TO 200 MPA  
BETWEEN 200 K AND 500 K USING A COMPACT SINGLE  
SINKER MAGNETIC SUSPENSION DENSIMETER FOR PURE  
AND NATURAL GAS LIKE MIXTURES**

A Dissertation

by

MERT ATILHAN

Submitted to the Office of Graduate Studies of  
Texas A&M University  
in partial fulfillment of the requirements for the degree of

DOCTOR OF PHILOSOPHY

Approved by:

Chair of Committee,	Kenneth R. Hall
Committee Members,	Perla B. Balbuena
	Maria A. Barrufet
	Mahmoud M. El-Halwagi
Head of Department,	N.K. Anand

August 2007

Major Subject: Chemical Engineering

## ABSTRACT

High Accuracy P- $\rho$ -T Measurements up to 200 MPa between 200 K and 500 K Using a Compact Single Sinker Magnetic Suspension Densimeter for Pure and Natural Gas Like Mixtures. (August 2007)

Mert Atilhan, B.S., Ege University, Izmir, Turkey;

M.S., Texas A&M University

Chair of Advisory Committee: Dr. Kenneth R. Hall

Highly accurate density data is required for engineering calculations to make property estimations in natural gas custody transfer through pipelines. It is also essential to have accurate pressure-volume-temperature (PVT) data for developing equations of state (EOS). A highly accurate, high pressure and temperature, compact single sinker magnetic suspension densimeter has been used for density measurements. First, the densimeter is calibrated against pure component densities for which very reliable data are available. After validating its performance, the densities of four light natural gas mixtures that do not contain components heavier than hexane and two heavy gas mixtures containing hexane and heavier components having fractions more than 0.2 mole percent were measured. The light mixtures were measured in the temperature range of 250 to 450 K and in the pressure range of 10 to 150 MPa (1450 to 21,750 psi); the heavy mixtures were measured in the range of 270 to 340 K and in the pressure range of 3 to 35 MPa (500 to 5,000 psi). Out of those, the data for only four light natural gas mixtures have been presented in the dissertation due to confidentiality agreements that are still in force. A force transmission error and uncertainty analysis was carried out. The total uncertainty was calculated to be 0.11%. Data calculated in this work is compared with the current industry standard EOS for natural gas systems (AGA8-DC92 EOS) and GERG EOS, which is the most recently developed EOS for natural gas systems. The data measured as a part of this research should be used as reference quality data, either to modify the parameters of AGA8-DC92 EOS and GERG EOS or to develop a more reliable equation of state with wider ranges of pressure and temperature.

## **DEDICATION**

To  
Selma  
and  
Our Families

## ACKNOWLEDGMENTS

I hereby wish to thank Dr. Kenneth R. Hall for giving me the opportunity to work in this project and for his advice, both professional and personal. I appreciate his patience and understanding during the difficult times with the project. I am grateful to Dr. Hall for financially supporting me for the last 5 years and making it possible for me to obtain my degrees at Texas A&M University. I would like to thank my advisory committee members Dr. Maria A. Barrufet, Dr. Perla Balbuena and Dr. Mahuod El-Halwagi for their time and advice.

I greatly appreciate long-distance customer support interactions of Dr. Hans Wilhelm Lösch, Mrs. Cornelia Lösch, Dr. Reza Seif of Rubotherm Präzisionsmesstechnik GmbH, Bochum, Germany. They helped troubleshoot the operation of the unique magnetic suspension densimeter used in this research work at several stages.

Also I would like to gratefully acknowledge the contributions of Dr. Mark O. McLinden and Dr. Eric W. Lemmon of NIST for their technical support in calibrating our apparatus parts and providing us access to NIST-12 and REFPROP programs.

I would like to appreciate the help I received from various people in the department, directly or indirectly related to my research. I would like to express my sincere gratitude to Mr. Randy A. Marek of machine shop helped us with our mechanical works and Mr. Jason W. Caswell of Physics electronic shop for spending countless hours with us advising on electrical and electronic problems and advancements of our experimental setup.

I am indebted to all my colleagues in the research group for the valuable time spent with them. I appreciate the help I received from Dr. Prashant V. Patil during the early stages of my lab experience. I find myself extremely lucky to work with Mr. Diego Cristancho and Mr. Ali Abedi in the same research group. I would like to thank them here for their help, time and friendship.

I would like to express my special thanks to Dr. Saquib Ejaz for his support and advice, for both professionally and personally. I am indebted to him for all his support.

I am especially thankful to Dr. M. Mahmoud El-Halwagi and his family for their warm and compassionate feelings for us. I am grateful to him for his advices in all aspects of life and closeness like an elder brother.

I also owe many thanks to my close friends Haluk Ersin Karaca, Ferdi Karadas and Fatih Mutlu for the long intellectual talks, discussions and advice.

I owe many thanks to my friends and my soccer team members. Without their support, I could not have done what I was able to do.

I am very indebted and grateful to my parents Atilla Atilhan and Nefise Muzaffer Atilhan for their support and understanding. I thank them hereby for teaching me values of this world. Also I would like to express my appreciation to my parent in laws Hamdi and Esmâ Koyunoglu for their support and understanding in all means. I thank my brother Cevat Rifat Atilhan, for being a role model for me at all stages of my life. I also thank my sisters-in-law and brothers-in-law for their support and guidance.

Above all, I find myself fortunate to have such a wonderful wife, Selma Atilhan. She has always been with me wherever, whenever at any circumstances. She makes everything more valuable in my life with her love, patience, support and understanding. I thank her for to advice both professionally and personally in developing my career.

## NOMENCLATURE

<i>a</i>	Calibration constant in the deviation equations of ITS-90 for a PRT or coil radius (in)
<i>A</i>	Cross sectional area of piston cylinder assembly of dead weight gauge (in <sup>2</sup> )
<i>b</i>	Calibration constant in the deviation equations of ITS-90 for a PRT
<i>b<sub>1</sub>, b<sub>2</sub></i>	Elastic distortion coefficients
<i>B</i>	Second virial coefficient (cm <sup>3</sup> /mole) or Constant in the reference function of ITS-90 for a PRT calibration
<i>C<sub>p</sub></i>	Isobaric heat capacity
<i>E</i>	Young's modulus (GPa)
<i>I</i>	Current through platinum resistance thermometer (mA)
<i>L</i>	length representing linear thermal expansion and contraction
<i>m</i>	Mass of sinker (g)
<i>M</i>	Molar mass (kg/kmole) or magnetic moment
<i>M<sub>x</sub></i>	Mass of DWG calibration weights in vacuum (kg)
<i>n</i>	Number of pairs of thermocouples forming a thermopile
<i>N</i>	Number of components in a natural gas mixture or constant in a polynomial equation
<i>P, p</i>	Pressure (MPa) [psia]
<i>R</i>	Resistance of platinum resistance thermometer (ohm) or universal gas constant (8.314 J/mole K)
<i>S</i>	Seebeck coefficient (μV/ °C) or Slope of pressure transducer calibration linear fit
<i>T</i>	Temperature (K)
<i>u</i>	Uncertainty or speed of sound
<i>V</i>	Volume of sinker (cm <sup>3</sup> ) or voltage drop, volt

$W$	Ratio of the resistance of a platinum resistance thermometer at a temperature to its resistance at the triple point of water or balance reading or weight
$x$	Composition as mole fraction

### ***Abbreviations***

AC	Alternating Current
AGA	American Gas Association
AGA8-DC92	Detailed Characterization method of the American Gas Association
BP	British Petroleum
CB	Cricondenbar
CP	Critical Point
CT	Cricondentherm
DC	Direct Current
DMM	Digital Multimeter
DPDT	Double Pole Double Throw
DPI	Differential Pressure Indicator
DWG	Dead Weight Gauge Piston
DWRRA	Deep Water Royalty Relief Act
EOS	Equation of State
FT	Fischer-Tropsch
FTE	Force transmission Error
GERG	European Group for Gas Research
GERG-2004	GERG-2004 EOS for gas mixtures
GoM	Gulf of Mexico
GTL	Gas to Liquids
GTE	Gas to Ethylene



HIP	High Pressure Equipment Company
HP	Hand Pump
IC	Isochore
IEA	International Energy Agency
IPTS-68	International Practical Temperature Scale of 1968
IT	Isotherm
ITS-90	International Temperature Scale of 1990
LNG	Liquefied natural gas
LVDT	Linear variable differential transformer
MMS	Minerals Management Service
MP	Measurement Point
MSD	Magnetic Suspension Densimeter
NIST	National Institute of Standards and Technology
PID	Proportional Integral Derivative
PPM	Parts per Million
PRT	Platinum Resistance Thermometer
PT6K	6,000 psia range Pressure Transducer
PT30K	30,000 psia range Pressure Transducer
SC	Suspension Control
SNG3	Synthetic natural gas mixture 3
SNG5	Synthetic natural gas mixture 5
SSR	Solid State Relay
T	Tee fitting
Ta	Tantalum
Ti	Titanium
V	Valve
ZP	Zero Point

***Greek letters***

$\alpha$	Temperature distortion coefficient ( $K^{-1}$ ) or thermal coefficient of expansion ( $K^{-1}$ ) or balance calibration factor
$\kappa$	Pressure distortion coefficient ( $MPa^{-1}$ )
$\Delta$	Difference or deviation
$X$	Internal temperature period of pressure transducer quartz crystal ( $\mu s$ )
$\rho$	Density ( $kg/m^3$ )
$\sigma$	Standard deviation or deviation at the 68% confidence level or normal stress
$\tau$	Pressure period of vibration of transducer quartz crystal ( $\mu s$ )
$\nu$	Poisson's ratio
$\phi$	Coupling factor
$\varepsilon$	Apparatus fluid specific constant (ppm) or strain (inch/inch)
$\chi$	Magnetic Susceptibility, $m^3/kg$
$\pi_\infty$	Zero pressure cell constant
$\gamma$	Pressure distortion coefficient ( $MPa^{-1}$ )

***Subscripts***

0	Index for constants $B$ and $D$ in reference functions of ITS-90 for PRT calibration
6+	Hexane and components heavier than hexane such as heptane, octane, etc
i	Component number or index for constants in the reference function of ITS-90 for PRT calibration
e-mag	Electromagnet
o	Reference condition of 23 °C for cross sectional area of piston cylinder assembly of dead weight gauge or reference condition of 20 °C and 1 bar pressure for sinker volume

p-mag	Permanent magnet
s	Initial set-point
S	Sinker
v	Vacuum condition

## TABLE OF CONTENTS

	Page
ABSTRACT .....	iii
DEDICATION .....	iv
ACKNOWLEDGMENTS.....	v
NOMENCLATURE.....	viii
TABLE OF CONTENTS .....	xii
LIST OF FIGURES .....	xv
LIST OF TABLES .....	xix
1. INTRODUCTION.....	1
1.1 Energy Consumption: Current and Future Projections.....	1
1.2 Natural Gas Outlook: Supply and Demand.....	3
1.3 Deepwater Gulf of Mexico: The New Frontier for North American Natural Gas.....	7
1.4 Need for Thermodynamic Properties ( $P$ - $\rho$ - $T$ ) and Phase Behavior Data of Natural Gas.....	9
1.5 Objective of Current Research.....	10
1.5.1 Overview .....	10
1.5.2 Short Term and Long Term Objectives.....	12
2. DENSITY MEASUREMENT TECHNIQUES .....	14
2.1 Introduction.....	14
2.2 Density Measuring Devices .....	14
2.2.1 Speed of Sound Methods.....	15
2.2.2 Vibrating Devices.....	15
2.2.2.1 Vibrating Wires .....	16
2.2.2.2 Vibrating Tubes.....	16
2.2.3 Expansion Devices: Burnett Method.....	18
2.2.4 Continuously Weighed Pycnometer Method .....	19
2.2.5 Hydrostatic Buoyancy Methods .....	20
2.2.5.1 Classical Methods .....	20
2.2.5.2 Magnetic Suspension Devices.....	21
3. MAGNETIC SUSPENSION DENSIMETERS AND FORCE TRANSMISSION ERROR PHENOMENA.....	22
3.1 Introduction .....	22

	Page
3.2 Two Sinker Densimeters .....	22
3.3 Single Sinker Densimeters .....	24
3.4 Force Transmission Error in Magnetic Suspension Densimeters .....	26
3.4.1 Force Transmission Error in Single Sinker Magnetic Suspension Densimeters .....	27
3.4.2 Force Transmission Error in Two Sinker Magnetic Suspension Densimeters .....	31
 4. EXPERIMENTAL SETUP, CONTROL SYSTEMS AND DATA ACQUISITION OF MAGNETIC SUSPENSION DENSIMETER.....	 32
4.1 Introduction .....	32
4.2 Overview of the MSD System .....	32
4.3 Feed Manifolds and Cylinder Storage.....	32
4.3.1 Pressure Transducer Calibration .....	36
4.3.2 Vacuum System.....	37
4.3.3 Compressor System.....	37
4.4 High Pressure Cell and Balance .....	39
4.5 Temperature Control .....	45
4.5.1 Heat Exchangers around the High Pressure Cell .....	45
4.5.2 Constant Temperature Bath.....	48
4.5.3 Liquid Propane Cooling System .....	49
4.5.4 Temperature Measurement and Methodology .....	52
4.5.5 Temperature Data Acquisition and Control .....	58
4.5.6 DAQ Card Configuration and NI Connector Block Connections.....	58
4.6 Pressure Transducers.....	61
4.7 Magnetic Suspension Densimeter Operations.....	63
4.7.1 Weight Changing Device .....	68
4.7.2 MSD Alignment .....	70
4.7.2.1 Vertical Alignment.....	70
4.7.2.2 Horizontal Alignment.....	71
4.7.3 Sinker Volume Calibration.....	71
4.8 LabView Data Acquisition Programs .....	72
 5. EXPERIMENTAL RESULTS: PURE COMPONENT AND SYNTHETIC NATURAL GAS DENSITY MEASUREMENTS.....	 75
5.1 Introduction .....	75
5.2 Pure Component Gas Density Measurements .....	75
5.2.1 Comparison of Pure Component Data with Literature.....	88
5.3 Synthetic Natural Gas Density Measurements.....	92

	Page
5.3.1 SNG 3 and SNG 5 Measurements .....	93
5.3.2 SNG 4 and SNG 6 Measurements .....	100
5.4 Synthetic Natural Gas Phase Envelope Measurements .....	105
5.5 Comments on SNG Mixture Experiments .....	107
5.6 Natural Gas Mixtures Including Heavy Components .....	107
6. CONCLUSIONS AND RECOMMENDATIONS.....	108
6.1 Conclusions .....	108
6.2 Recommendations .....	110
REFERENCES.....	112
APPENDIX A .....	118
APPENDIX B .....	121
APPENDIX C .....	123
APPENDIX D .....	129
APPENDIX E.....	131
APPENDIX F .....	135
VITA .....	141

## LIST OF FIGURES

	Page
FIGURE 1. Energy consumption and production since 1950 overview including both fossil fuel sources and renewable energy sources. ....	2
FIGURE 2. Energy consumption with respect to different sources. ....	2
FIGURE 3. World Natural Gas Consumption, 1990-2030 .....	3
FIGURE 4. World natural gas consumption by end sector, 2003-2030 .....	4
FIGURE 5. AGA8-DC92 EOS uncertainty regions [17]. ....	11
FIGURE 6. Vibrating tube densimeter scheme. ....	17
FIGURE 7. (a) Basic scheme for two-sinker MSD, (b) Wagner and Kleinrahm's two-sinker MSD [15, 43]. ....	23
FIGURE 8. (a) Basic scheme for single-sinker MSD, (b) Operating modes of single-sinker MSD [15, 43]. ....	25
FIGURE 9. Single Sinker MSD weighing positions. ....	27
FIGURE 10. MSD apparatus constant pressure and temperature dependence. ....	30
FIGURE 11. Experimentally calculated MSD fluid specific constant. ....	30
FIGURE 12. Temperature dependence of intercept for $\epsilon$ (P,T) equation. ....	31
FIGURE 13. MSD system overview with main and ancillary equipments .....	33
FIGURE 14. Compressing manifold flow diagram. ....	34
FIGURE 15. Manifold 2 flow diagram .....	35
FIGURE 16. Diagram for Ruska DWG and DPI facility. ....	37
FIGURE 17. Haskel compressor and nitrogen drive. ....	38
FIGURE 18. The Entire MSD. Scaled figure scanned from Rubotherm manual [56]. ...	39
FIGURE 19. Weighing balance, weighing balance frame and balance base plate .....	40
FIGURE 20. Concrete blocks, aluminum platform and weighing balance. ....	41
FIGURE 21. Electromagnet shaft and hook assembly. ....	42
FIGURE 22. Cross section of the weighing balance cell for METTLER balance [44].	44
FIGURE 23. Heat exchanger shields and vacuum chamber schematics. ....	46
FIGURE 24. Heating/Cooling shield -2 with heating tape 1 and 2 connections made. ....	47

	Page
FIGURE 25. High pressure MDS cell with PRT and thermopile connections made. ....	47
FIGURE 26. PolyScience ® constant temperature bath and its connections to MSD. ....	49
FIGURE 27. Schematic diagram of the propane cooling system. ....	50
FIGURE 28. Schematic of heat exchanger of propane cooling system. ....	52
FIGURE 29. Liquid propane tank. ....	53
FIGURE 30. Liquid nitrogen/ liquid propane heat exchanger (a), liquid propane tank (b). ....	53
FIGURE 31. Constant current source. ....	55
FIGURE 32. Constant current source current reversing procedure. ....	56
FIGURE 33. Overview of the data acquisition and control system. ....	59
FIGURE 34. DAQ card connector block. ....	59
FIGURE 35. Picture of temperature control system box. ....	60
FIGURE 36. Circuitry and connection diagram of temperature control system box. ....	61
FIGURE 37. Schematic of pressure transducer thermo-stating system. ....	63
FIGURE 38. Cross-section of MSD high pressure measuring cell (units in mm). ....	64
FIGURE 39. Operation of MSD (a) Magnetic levitation off; (b) magnetic levitation is set to ZP position; (c) magnetic levitation is set to MP position. ....	66
FIGURE 40. Position sensor box. ....	67
FIGURE 41. Illustration of weighing balance actual curve vs. ideal weighing curve. ....	68
FIGURE 42. Weight changing device (Ta weight on the left, Ti weight on the right). ....	69
FIGURE 43. Nitrogen density deviations from NIST-12 Database, 2005. ....	78
FIGURE 44. Nitrogen density deviations from NIST-12 Database, 2006. ....	80
FIGURE 45. Nitrogen density deviations from NIST-12 Database, high pressure, 2007. ....	83
FIGURE 46. Nitrogen density deviations from NIST-12 Database, all points, 2007. ....	83
FIGURE 47. Carbondioxide density deviations from NIST-12 Database, 2006. ....	84



	Page
FIGURE 48. Carbondioxide density deviations from NIST-12 Database, all points, 2007. ....	87
FIGURE 49. Methane density deviations from NIST-12, all points, 2005.....	88
FIGURE 50. Literature nitrogen deviations from NIST-12 database for temperatures between 260 K and 280 K [39, 66-69].....	89
FIGURE 51. Literature nitrogen deviations from NIST-12 database for temperatures between 330 K and 350 K [39, 66-69].....	89
FIGURE 52. Literature methane deviations from NIST-12 database for temperatures between 260 K and 273.15 K [68, 70-73].....	90
FIGURE 53. Literature methane deviations from NIST-12 database for temperatures between 323 K and 350 K [70-74].....	90
FIGURE 54. Literature carbon dioxide deviations from NIST-12 database for temperatures between 240 K and 313 K [76]. ....	91
FIGURE 55. Literature carbon dioxide deviations from NIST-12 database for temperatures between 323 K and 470 K [76]. ....	91
FIGURE 56. Density deviations for SNG 3 from AGA8-DC92 EOS. ....	95
FIGURE 57. Density deviations for SNG 3 from GERG-2004 EOS. ....	95
FIGURE 58. Density deviations for SNG 5 from AGA8-DC92 EOS. ....	97
FIGURE 59. Density deviations for SNG 5 from GERG-2004 EOS. ....	97
FIGURE 60. Density deviations for SNG 4 from AGA8-DC92 EOS. ....	102
FIGURE 61. Density deviations for SNG 4 from GERG-2004 EOS. ....	102
FIGURE 62. Density deviations for SNG 6 from AGA8-DC92 EOS. ....	104
FIGURE 63. Deviations for SNG 6 from GERG-2004 EOS. ....	104
FIGURE 64. Experimental phase envelope points and PR EOS predictions for SNG mixtures. ....	106
FIGURE E.1. Temperature control program screenshot. ....	131
FIGURE E.2. Automatic balance control and data acquisition program screenshot. ....	132
FIGURE E.3. Pressure transducer program screenshot. ....	133

	Page
FIGURE E.4. Manual balance control program screenshot.....	134
FIGURE F.1. M91C1 mixture measurements uncertainties due to temperature. ....	137
FIGURE F.2. M91C1 mixture measurements uncertainties due to pressure. ....	138
FIGURE F.3. M91C1 percentage uncertainty caused by temperature, pressure and compositions. ....	139

## LIST OF TABLES

	Page
TABLE 1 World Natural Gas Reserves by Country as of January 1, 2006 .....	5
TABLE 2 Variable resistor values determined for different temperature ranges .....	68
TABLE 3 Pure component compositions, impurities and manufacturers .....	76
TABLE 4 Pure nitrogen experimental density and % deviation from NIST-12 database, 2005 .....	77
TABLE 5 Pure nitrogen experimental density and % deviation from NIST-12 database, 2006 .....	78
TABLE 6 Pure nitrogen experimental density and % deviation from NIST-12 database, 2007 .....	80
TABLE 7 Pure carbondioxide experimental density and % deviation from NIST- 12 database, 2006 .....	84
TABLE 8 Pure carbondioxide experimental density and % deviation from NIST- 12 database, 2007 .....	85
TABLE 9 Pure methane experimental density and % deviation from NIST-12 database, 2005 .....	87
TABLE 10 SNG 3 mixture compositions. ....	93
TABLE 11 SNG 5 mixture compositions. ....	93
TABLE 12 SNG 3 experimental P- $\rho$ -T data (after correction term) .....	94
TABLE 13 SNG 5 experimental P- $\rho$ -T data (after correction term) .....	96
TABLE 14 American Gas Association (1992) data regions. ....	98
TABLE 15 Ranges of gas mixture characteristics for AGA8-DC92 EOS .....	99
TABLE 16 Total number of experimental points and their corresponding AGA8- DC92 EOS regions for SNG 3 and SNG 5 mixtures .....	99
TABLE 17 SNG 4 mixture compositions. ....	100
TABLE 18 SNG 6 mixture compositions. ....	100
TABLE 19 SNG 4 experimental P- $\rho$ -T data (after correction term) .....	101

	Page
TABLE 20 SNG 6 experimental P- $\rho$ -T data (after correction term).....	103
TABLE 21 Total number of experimental points and their corresponding AGA8- DC92 EOS regions for SNG 4 and SNG 6 mixtures.....	105
TABLE 22 SNG mixtures experimental phase envelope data.....	106
TABLE B.1 Constants in Deviation Equations and Reference Functions of ITS-90. ...	122
TABLE C.1 Parameter values from the calibration report of DWG.....	125
TABLE C.2 Component weights from the calibration report of DWG.....	125
TABLE C.3 Instruments used during pressure transducer calibration.....	126
TABLE C.4 Corrections that are used during pressure transducer calibration.....	127
TABLE D.1 Mettler Toledo balance calibration.....	129
TABLE D.2 Sinker weighings on Mettler Toledo balance pan.....	130
TABLE F.1 M91C1mixture composition and component uncertainties.....	137
TABLE F.2 Percentage uncertainty due to temperature, pressure and compositions....	138
TABLE F.3 Uncertainties due to MSA and balance such as sinker volume, balance weighings, etc.....	140

## 1. INTRODUCTION

### 1.1 Energy Consumption: Current and Future Projections

Energy is critically important to maintain life on earth, sustain our living standards and to attain economic progress. Currently, most energy on earth is derived from fossil based fuels such as coal, oil and natural gas. Among these, natural gas is the cleanest, safest, and most useful.

Natural gas is a mixture of predominantly methane and other paraffinic hydrocarbons such as ethane, propane, butane, pentane etc. and with smaller quantities of nitrogen, carbon dioxide, and non-hydrocarbon gases such as helium, hydrogen sulfide and water. Natural gas is used extensively in residential, commercial and industrial areas and applications, and it is the most widespread energy source used for home heating with about 55 per cent of American homes using gas. Natural gas is distributed by a nationwide network of pipelines for use in the domestic sector for residential space heating and in the industrial sector for electric power generation plants. In electric power generation plants, steam is generated using natural gas in boilers. Steam in turn drives the turbines. Thus, energy as heat is converted into mechanical energy [1].

The world economy should double in size by 2030 with most of the growth taking place in the developing countries. Moreover, world energy needs may grow by 50% with most of the expansion happening in the developing countries [2]. The Energy Information Administration of the US Department of Energy (DOE) states that since 1950 coal, oil and natural gas have become the major sources of energy all around the globe. Figure 1 presents historical data covering demand and consumption of total energy based upon coal, oil and natural gas since 1949 with projections through 2025. Figure 2 shows the consumption trends of coal, oil and natural gas and other energy sources. The annual US energy consumption may increase from approximately 91.5 EJ [86.7 quadrillion Btu] in 2002 to 131.4 EJ [124.5 quadrillion Btu] in 2025 [3]. The consumption of petroleum surpasses that of either natural gas or coal.

---

This dissertation follows the style of Journal of Chemical Thermodynamics.

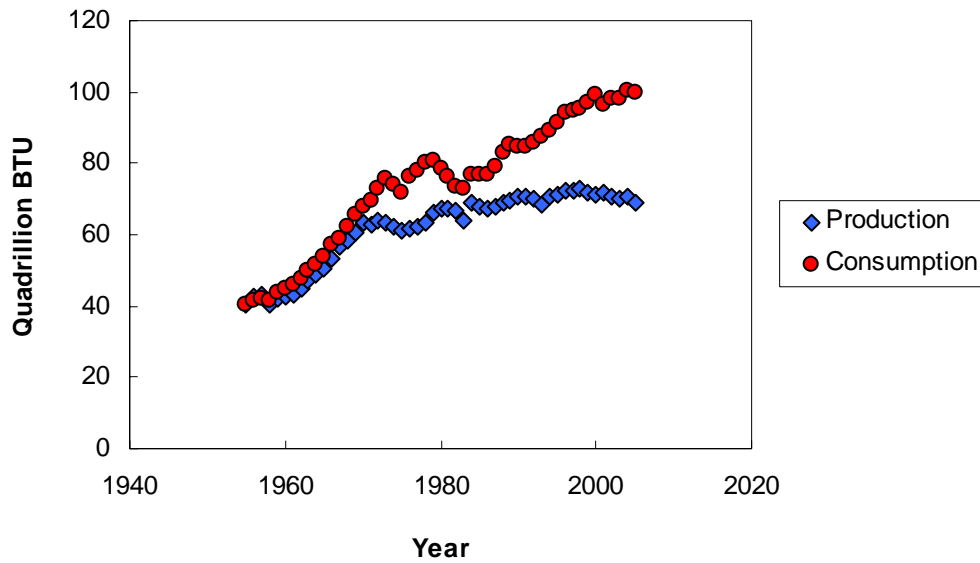


FIGURE 1. Energy consumption and production since 1950 overview including both fossil fuel sources and renewable energy sources.

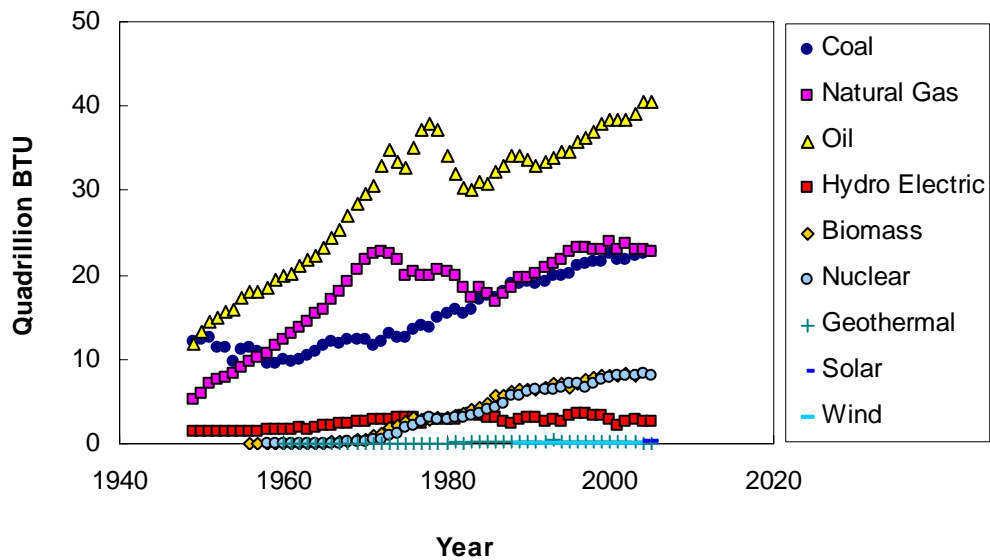


FIGURE 2. Energy consumption with respect to different sources.

## 1.2 Natural Gas Outlook: Supply and Demand

According to DOE, Figure 3, consumption of natural gas worldwide may increase from 95 trillion cubic feet in 2003 to 182 trillion cubic feet in 2030. Natural gas consumption worldwide should increase at an average rate of 2.4% annually from 2003 to 2030, whereas coal increases 2.5% and oil increases 1.4% on a yearly basis. However, natural gas is still more attractive energy source because of environmental concerns as it burns more efficiently than coal. Therefore natural gas should be the fuel of choice in many regions of the world.

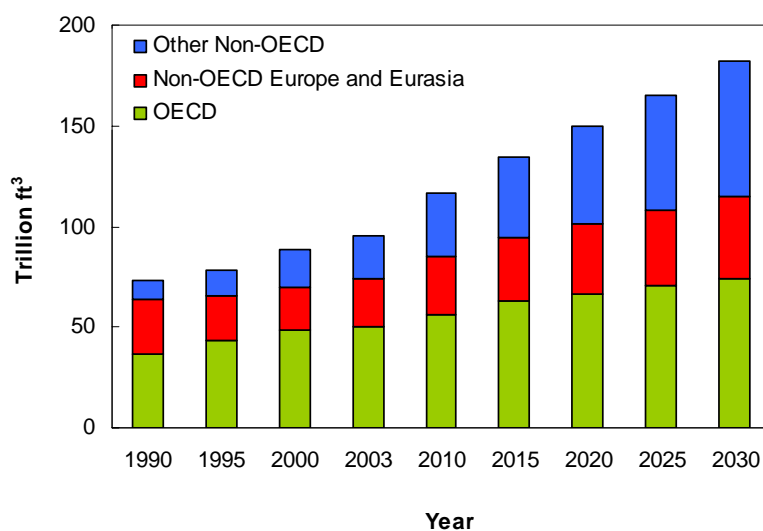


FIGURE 3. World Natural Gas Consumption, 1990-2030.

The largest natural gas consuming sectors in the economy are industrial and electric power generating facilities worldwide (figure 4). In 2003, the industrial sector consumed 44% of the overall natural gas production whereas electricity generation consumed 31%. According to projections, natural gas use should grow by 2.8% per year in the industrial sector and 2.9% per year in the electric power sector from 2003 to 2030. According to projections for the industrial sector, natural gas overtakes oil as the dominant fuel by 2030. In the electric power sector, despite its rapid growth, natural gas remains a distant second to coal in terms of share of total energy use.

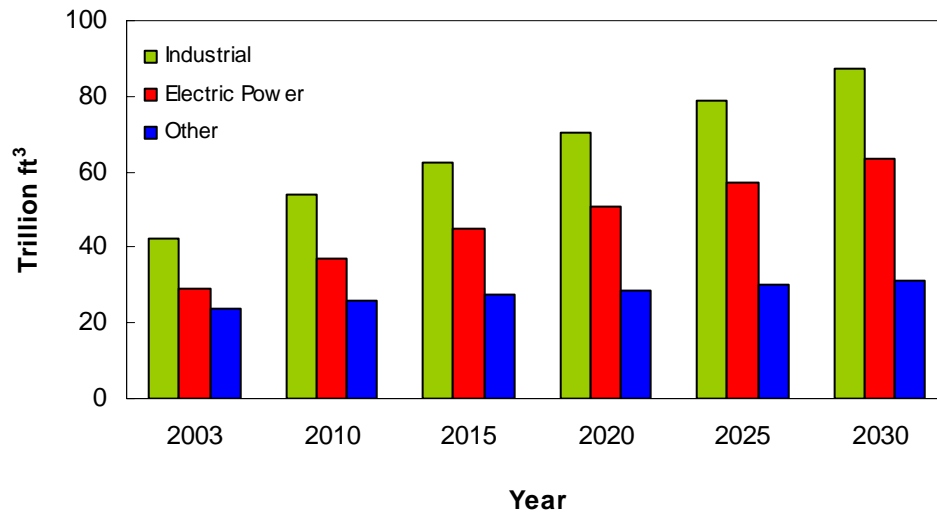


FIGURE 4. World natural gas consumption by end sector, 2003-2030.

As of the first quarter of 2006, proved world natural gas reserves were estimated as 6,112 trillion ft<sup>3</sup> which is 70 trillion ft<sup>3</sup> (about 1%) higher than the estimate for 2005 [4]. Of these reserves, almost 75% are in the Middle East and Eurasia. As shown in Table 1, Russia, Iran, and Qatar have combined reserves that correspond to 58% of the world total natural gas reserves as of 2006. Reserves in the rest of the world are distributed fairly evenly on a regional basis.

Of the total natural gas resource base, almost half of the world current reserves are stranded, usually located too far from pipeline infrastructure or population centers for economical transportation. With new natural gas resources expected through 2025, total natural gas reserve growth accounts for 2,347 trillion ft<sup>3</sup> [5]. More than one-half of the undiscovered natural gas should come from Eurasia, the Middle East, and North Africa; and about 25% should come from a combination of North, Central, and South America.

In addition to the world natural gas reserves, natural gas demands also require projection to adjust energy policies for coming decades. North American natural gas consumption may increase at an average annual rate of 1.1% between 2003 and 2030.



The regional growth rate for natural gas demand is somewhat slower than in past international energy outlook (IEO) reports [6], largely because of the impact of higher

TABLE 1

World Natural Gas Reserves by Country as of January 1, 2006.

<b>Country</b>	<b>Reserves (Trillion ft<sup>3</sup>)</b>	<b>% World Total</b>
World	6,112	100.0
Top 20 Countries	5,510	90.2
Russia	1,680	27.5
Iran	971	15.9
Qatar	911	14.9
Saudi Arabia	241	3.9
United Arab Emirates	214	3.5
United States	193	3.1
Nigeria	185	3.0
Algeria	161	2.6
Venezuela	151	2.5
Iraq	112	1.8
Indonesia	98	1.6
Norway	84	1.4
Malaysia	75	1.2
Turkmenistan	71	1.2
Uzbekistan	66	1.1
Kazakhstan	65	1.1
Netherlands	62	1.0
Egypt	59	1.0
Canada	57	0.9
Kuwait	56	0.9
Rest of World	602	9.8

prices for natural gas in the United States, the largest natural gas consumer in North America. The United States accounted for around 80% of the total consumed natural gas of 27.4 trillion ft<sup>3</sup> in North America in 2003. Despite robust growth in demand for

natural gas in Canada and Mexico, this number may still be 73% of the total in 2030 for United States.

Because of currently high prices in the United States, gas-fired electricity generation plants should not be constructed in the midterm. Currently, Canada is the largest supplier of natural gas for the U.S. with about 90% of the total. Canada should remain the primary source of natural gas imported into the United States until 2010. New LNG plants and LNG transportation networks may eventually replace imports from Canada. More than 30% of the remaining U.S. resources are alternative sources, which include tight sands, shale, and coal-bed methane.

Natural gas also should be the fastest growing fuel in the Organization for Economic Co-operation and Development (OECD) countries in Europe, with demand increasing at an annual average rate of 2%, from 17.8 trillion ft<sup>3</sup> in 2003 to 30.8 trillion ft<sup>3</sup> in 2030. Use of natural gas in electric power generation is expected to be almost 60% for OECD Europe between 2003 and 2030 which means an average annual increase of 4% from 2003 to 2030 exceeding the use of coal or nuclear power by 2020 [6].

The non-OECD Europe and Eurasia areas are more dependent upon natural gas than any other region in the world. Russia is second only to the United States in total natural gas use, and it is the only country in the world where natural gas accounts for more than one-half of total primary energy use. In 2003, Russia consumed 15.3 trillion ft<sup>3</sup> of natural gas, whereas, the other non-OECD Europe and Eurasia countries met about 44% of their combined total energy needs with natural gas in 2003. Increase in natural gas demand in non-OECD Europe and Eurasia persists throughout the projection period until 2030, with an average annual growth rate of 2% [6].

In the rest of the non-OECD countries, significant growth in natural gas use is projected from 2003 to 2030, as strong economic growth and available resources encourage the development of natural gas infrastructure to support demand. In the other non-OECD countries (excluding non-OECD Europe and Eurasia), natural gas demand triples in the IEO2006 reference case, from 21.7 trillion ft<sup>3</sup> to 67.3 trillion ft<sup>3</sup> between 2003 and 2030 [6]. Utilization of natural gas in the Middle East is projected to double

between 2003 and 2030. In addition, natural-gas-rich countries in the region are developing projects to monetize their natural gas resources, in particular through LNG, gas-to-liquids (GTL) and gas-to-ethylene (GTE) projects, which have become active areas of research and interest.

As a result, it is easy to conclude that the trend of natural gas use in industry, electric power plants and in residential areas should continue to increase according to all predictions. Distribution from producing countries to consumers is also a critically important issue. The importance of pipeline networks is politically and economically important. Another important consideration is how to provide an economical means to monetize stranded gas.

For this reason, active research in natural gas transportation using means other than pipelines is critical in terms of determining today's and future energy trends. Natural gas custody transfer is one important area that this work addresses.

### **1.3 Deepwater Gulf of Mexico: The New Frontier for North American Natural Gas**

Currently, energy usage relies heavily upon domestic natural gas production and this trend should continue until advances in clean coal technology provide an acceptable means to generate electricity. Production of gas from many onshore basins has matured and they now produce less than their peak rates. Since 1947, natural gas has been produced from offshore platforms.

The Minerals Management Service (MMS) of the US Department of the Interior classifies offshore platforms according to depth at which they produce. According to the classification, platforms at water depths up to 304.8 m are shallow-water, those greater than 304.8 m but less than 1,524 m are deepwater, and those greater than 1,524 m are ultra-deepwater [7]. The deepwater Gulf of Mexico (GoM) is a crucial oil and gas region and an essential part of North American oil and gas supply. Production of oil and gas in the deepwater GoM dates back to 1979. A sustained and robust expansion of exploration activities has continued since 1995 [7]. Starting from 1995, the US Federal government has passed laws that allow and encourage both major and independent companies to explore and produce oil and gas from deep water in the GoM [8, 9]. With new offshore

platform technologies, semi-submersible, floating or platform based well drilling rigs can drill either vertically or directionally up to 3,048 m of water depth and up to 9,144 m true vertical depth. Before advancements in platform design and construction capabilities from fixed and compliant towers, tension leg platforms, spars, semi-submersible floating production systems, floating production storage and offloading vessels and subsea tieback development systems, deepwater and ultra-deepwater production was not feasible.

Beginning in 2004, 90 hydrocarbon production projects were launched. These new projects added 959 thousand barrels of oil per day and 3.6 billion ft<sup>3</sup> of natural gas per day. Between 1995 and 2003 about 750 exploration wells were drilled and around 15% of those were successful and announced as deepwater discoveries. Overall, there had been a rise of 535% and 620% in production in oil and gas production respectively since 1995. In addition to deepwater discoveries between 2001 and 2003, 11 ultra-deep water discoveries were made in the GoM at 2,500 m or deeper. These ultra-deep discoveries have opened a new frontier.

Because of the huge investment required to obtain successful results, most independents may avoid offshore exploration. Many of the novel pipelines built by private pipeline transportation entities could merge independent production from sub-sea developments. All 'shared' production can be transported to a main pipeline that then proceeds to a regional hub processing facility. Tieback development systems and the hub concept have become popular in deepwater, ultra-deep water [10] and even in shallow-water production as discussed by Baud et al [7]. The presence of a deepwater pipeline network remote requires an onshore network.

The Mardi Gras oil and gas transportation system is an example of such a pipeline network located in the GoM. BP operates the Mardi Gras transportation system, which currently it is the largest capacity deepwater pipeline system. When completed, it can transport more than 1 million bpd of oil and 1.5 bcf/d of natural gas. The five pipelines in the system, with diameters between 16 in and 30 in and a total length of 485 miles occupy water depths of 4,500 ft to 7,300 ft [11].

The deepwater pipeline network notion makes alternative transport concepts such as GTL appear redundant for GoM. However, a GTL plant on floating production storage and offloading (FPSO) vessels would still be economical to link newly-explored, isolated deepwater or ultra-deepwater reservoirs having no connection to pipeline network and uneconomical to connect to the pipeline network [12].

#### **1.4 Need for Thermodynamic Properties ( $P$ - $\rho$ - $T$ ) and Phase Behavior Data of Natural Gas**

Because it is impossible to measure the thermodynamics properties of all systems in nature, we must rely upon mathematical models to extrapolate the available experimental data. In order to develop such models, very accurate experimental data are necessary for selected complex mixtures, such as those that exist in natural gas. For this reason researchers must collect the most important and fundamental thermodynamics properties for such systems. Two of the most important thermodynamics properties are the pressure volume (density) and temperature ( $P\rho T$ ) surface and the phase equilibrium properties of mixtures. Accurate volumetric property data are used in custody transfer operations for natural gas. Also accurate  $P\rho T$  data are necessary for calculating energy functions. On the other hand, phase equilibria data are needed mostly for design calculations involving separation processes. Additionally, very accurate phase equilibrium knowledge is necessary for natural gas transfer through pipelines to avoid condensation in the pipelines. Atilhan et. al. [13] have shown that even widely used equations of state (EOS) such as Peng-Robinson or Redlich-Kwong (RK) cannot predict the retrograde condensation region for simple natural gas-like mixtures that do not contain heavy fractions.

When natural gas rises from the reservoir to the ocean floor at offshore platforms, the stream temperature can drop quickly (perhaps 5 to 10 °C) until it reaches the surrounding ocean temperature. This rapid temperature drop at high pressure along with moisture in the natural gas stream make conditions favorable for gas hydrate formation in the pipeline. Hydrates can cause several serious problems such as: plugging the

pipeline and blowouts [14]. Such problems can be avoided by increasing the temperature and insulating the stream that comes from the ocean bed, or by lowering the pressure of the pipeline. Another possible solution is lowering the dew point of water in the stream by adding polar solvents to the line such as methanol or glycols. In order to apply all these methods, accurate knowledge on  $P\rho T$  behavior of the natural gas stream is necessary.

## **1.5 Objective of Current Research**

### **1.5.1 Overview**

Main objective of this research is to develop  $P\rho T$  data for natural gas-like mixtures that have are complex and cannot be predicted by existing EOS. Because of their importance, density measurements essential for both industrial applications and scientific research. Very accurate  $P\rho T$  data is required not only to calculate custody transfer of natural gas in pipelines but also to develop new EOS for industrial and scientific use. Experimental  $P\rho T$  data is employed to calculate thermal properties of fluids required for industrial process design calculations. Loss of accuracy from density predictions directly impacts processes; therefore only exceptionally good density values ensure good thermal properties [15].

Knowledge of temperature, pressure and composition enables determination of the density from an EOS. The equation most widely used in custody transfer of natural gas is the Detailed Characterization Method or AGA8-DC92 EOS developed by American Gas Association (AGA) in 1992 [16]. This EOS was derived using an extensive and reliable experimental  $P\rho T$  database that included real natural gas mixtures as well as high order hydrocarbon mixtures (mostly binary mixtures of natural gas components). AGA8-DC92 EOS has different accuracy regions as shown in figure 5.

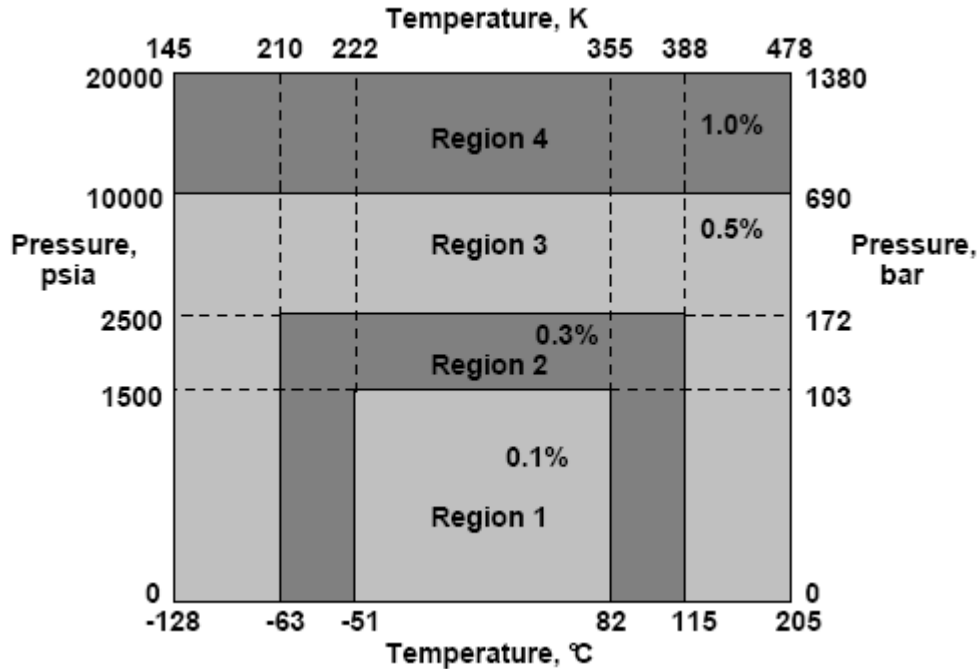


FIGURE 5. AGA8-DC92 EOS uncertainty regions [17].

As seen in figure 5, the maximum uncertainty claimed for the EOS is 0.1% in region 1, 0.3% in region 2, 0.5% in region 3 and 1.0% in region 4. However, the equation is valid only for lean natural gas mixtures over this wide range of conditions, and its ability to describe rich natural gases is untested. The equation cannot perform equilibrium calculations, as it is only valid for gas phase calculations. Also, use of the equation is not recommended near the critical point. The deviations from density measurements are 2 to 2.5% for North Sea natural gas samples at 8 to 17 MPa and 40 to 80 °C [18]. Following this, the Gas Research Institute (GRI) and National Engineering Laboratory (NEL) started a collaborative, joint industry project to extend the range of applicability of AGA8-DC92 for natural gas mixtures to include the gas compositions observed in the North Sea.

The reassessment of AGA8 has taken on added significance lately with deep drilling into the offshore reservoirs in the GoM. The typical compositions observed there differ

from the lean gas samples in the databank used to develop AGA8-DC92 EOS. For example, in region 1, AGA8-DC92 EOS is designed such that heavy alkane fractions (such as the hexane+) should be less than 0.2 mol percent, whereas, GoM samples generally include such heavy components in the range of 0.3 to 0.4 mol percent. The presence of such heavy fractions has a great effect on EOS in predicting density values for the natural gas sample at given temperature and pressure.

### **1.5.2 Short Term and Long Term Objectives**

The current research project for accurate density measurements was inspired by the need to check an existing industry standard EOS. A state-of-the-art, high pressure, high temperature, single-sinker Magnetic Suspension Densimeter (MSD) was used for accurate density measurements. These density data, along with new measurements can be used to develop a new EOS [19, 20]. Another part of the same research project that can help deepwater production operationally is measurement of the vapor-liquid two-phase envelope [21].

Short term and long term objectives are:

- i)* Re-commissioning of the MSD first commissioned by Patil [22].
- ii)* Measurements of ultra-high purity and high purity single component gases at pressures up to 175 MPa in the temperature range 260 to 450 K. Experimental density values can be compared to the NIST-12 pure component database. The results can indicate the performance of the MSD.
- iii)* Experimentally measured densities of simulated natural gas samples that are similar to the expected compositions of GoM samples observed at the production platforms should be compared to AGA8 to check its validity.
- iv)* Measure densities of a wide range of synthetic natural gas mixtures at very high temperatures and pressures to simulate reservoir conditions and build a database.
- v)* Experimental investigations and theoretical calculations from numerous EOS for phase envelopes should be compared to data.
- vi)* An error analysis and total uncertainty analysis will be provided.



- vii)* All the  $P\rho T$  data developed will be used in recalculating the parameters of AGA8-DC92 EOS.
- viii)* A new EOS that can replace AGA8-DC92, GERG2004 [23], will be tested against this accurate  $P\rho T$  database.
- ix)* More pure component data will be collected using the MSD at very high pressures and various different temperatures to investigate the force transmission error (FTE) phenomena in the MSD.
- x)* Finally, a very accurate  $P\rho T$  database will be used to develop a new EOS that can replace AGA 8 for custody transfer of natural gas.

## 2. DENSITY MEASUREMENT TECHNIQUES

### 2.1 Introduction

This section contains reviews of several experimental methods for density measurements, and discusses the relative strengths and weakness of each method. Finally, it contains the philosophy of our experimental approach to  $P\rho T$  studies.

An EOS can describe the thermodynamic state or vapor liquid equilibrium (VLE) of pure fluids and mixtures with accuracy that depends upon the application. The accuracy of an EOS depends upon the experimental data used during development of the equation. Historically, the quality of predictions obtained from EOS has improved dramatically as advanced technologies and new instrumentation have become more common for experimental methods.

Among the thermodynamic properties, density is the most directly predicted property using EOS. The measured densities should be approximated by suitable EOS and the measurements should be traceable to the International System of Units [24].

According to Kleinrahm et. al. [25], the following considerations are important when deciding upon a density measurement technique:

- i)* Large pressure and temperature range for wide operations.
- ii)* Low total uncertainty and high accuracy of the method for the overall range.
- iii)* Simplicity in design and ease of maintenance and operation.
- iv)* Little time required for each data point measurement.

### 2.2 Density Measuring Devices

Several different density-measurement techniques are described in this section, including: speed of sound methods, vibrating body techniques, continuous weighing method and buoyancy-based densimeters.

### 2.2.1 Speed of Sound Methods

Speed of sound measurements can be used to determine the performance of an equation of state for thermodynamics property predictions. By correlating the speed of sound to thermodynamics properties, one can build experimental devices and investigate solid, liquid and gas thermodynamics properties for pure components and mixtures. Densities and isothermal and isentropic compressibility factors result from speed of sound measurements experiments [26].

Based upon a pulse technique described by Daridon et. al. [27], a cylindrical-shaped cell is used to measure ultrasonic waves. In the pulse technique, effects of pressure upon piezo-electric materials are isolated by separating piezo-electric elements from the fluid studied. The speed results from the measurements of the transit time through the sample and the length of passage, which is a function of temperature and pressure. Density comes from:

$$\rho(P,T) = \rho_0(P_0,T_0) + \int_{P_0}^P u^{-2} dP + T \int_{P_0}^P (\alpha^2 / C_p) dP \quad (1)$$

In above equation  $u$  is the sound speed,  $\alpha$  is the isobaric coefficient of thermal expansion,  $C_p$  is the isobaric heat capacity and  $P_0$  is the atmospheric pressure. The sum of these terms gives the density with as a function of pressure at different temperatures.

The first integral, where  $u^{-2}$  can be expressed as a polynomial in pressure with coefficients expressed as polynomials in temperature, can be evaluated along the isotherms considered.

By using thermodynamics relations for  $(\partial\alpha/\partial p)_T$  and  $(\partial C_p/\partial p)_T$ , the second integral can be calculated iteratively. The second integral is a few percent of the first integral. More detailed discussion on numerical evaluations for such measurements appears in [26] and [27].

### 2.2.2 Vibrating Devices

Vibrating tubes and vibrating forks are common density measuring techniques. These devices measure the fluid density of interest by determining the oscillation

frequency of the vibrating element in the fluid. These instruments provide accurate results quickly. However, frequent calibration is necessary for this apparatus to maintain its accuracy [28]. Moreover, when the density of the fluid is vastly different from air or pure water (frequently used as reference fluids because of their well-known thermophysical properties) the uncertainty of the measurements increases as reported by Kuramoto et al. [24].

### **2.2.2.1 Vibrating Wires**

In vibrating wire densimeters, a wire carrying a diamagnetic weight is suspended in the fluid to be monitored. The wire is placed in a robust position in a uniform magnetic field provided by permanent magnet in both vertical and horizontal directions. When an alternating current passes through the power source to the wire, interaction starts with the current and the magnetic field. This leads to induced harmonic motion that is orthogonal to the magnetic field and the wire. If the mass, density and the dimension of all the solid components of the system are known, the resonant frequency of the wire can be determined experimentally under vacuum conditions. If the viscosity of the fluid of interest is known, experimental measurement of resonant frequency of wire velocity provides the fluid density [29, 30].

Although the vibrating wire technique is suitable for a wide range of pure fluid and mixture gas density applications, it suffers from problems such as surface tension on the wire, adsorption on the weight, detailed knowledge need of exact dimensions of the wire and the assembly. However, the device is used widely as a primary densimeter device because it has a simple operating principle and allows development of an exact physical model. Density, in principal, can be calculated directly from the theory.

### **2.2.2.2 Vibrating Tubes**

Vibrating tube densimeters consist of an assembly that includes two thin walled metallic or glass tubes bent in Y or V shapes as shown in figure 6. A permanent magnet and drive coil reside between these two tubes. Generally, a drive coil and a permanent

magnet are placed in the middle of the two tubes. The drive coils and magnet are mounted on the opposite legs of the tubes.

Each coil and magnet on the side leg forms a pick-off circuit. Alternatively, attractive and repulsive magnetic fields between the coils and magnets are provided by sending alternating current to the drive coil.

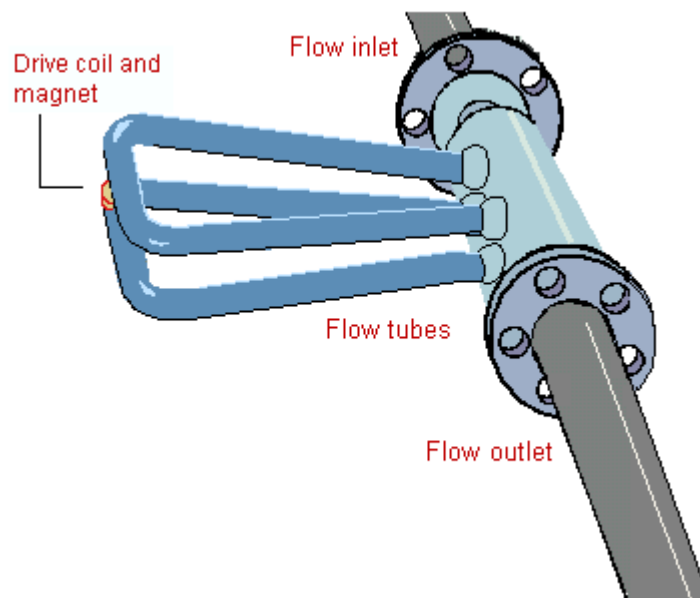


FIGURE 6. Vibrating tube densimeter scheme.

Because the drive coils and the magnets are installed on the opposing side of the tubes, a sine wave generated by the two pick-up circuits represents the motion of one tube relative to the other. The sine waves are in phase if there is no flow in the tube. The density of the fluid is:

$$\rho = K\tau^2 + L \quad (2)$$

where, tube parameters  $K$  and  $L$  are both pressure and temperature dependent and  $\tau$  is the period of vibration. Because it is not possible to determine the temperature and pressure dependence of  $K$  and  $L$ , measurements are performed at the same temperature and

pressure conditions with the sample. A reference fluid of well-known properties is used for this reason.

Finally, the corresponding density difference equation is:

$$\rho - \rho_r = K(\tau^2 - \tau_r^2) \quad (3)$$

where subscript r stands for the reference fluid.

$\tau^2$  and  $\rho$  are not exactly linear, and this must be taken into consideration. The vibrating tube densimeters are designed for rapid operation and they perform very precise measurements of density differences. If one assumes linearity between  $\tau^2$  and  $\rho$ , the highest levels of accuracy expectations are not achieved.

### 2.2.3 Expansion Devices: Burnett Method

Another well-established and widely-used density measurement device is the Burnett apparatus. Burnett [31] suggested a technique to measure the densities of sample fluids without measuring the mass or volume directly. An expansion device contains two cells. During operation, the sample is charged initially into the first cell and, after pressure and temperature measurement, expanded into the second cell. The ratio of the final volume to the original volume equals the ratio of densities before and after the expansion. Only pressure and temperature are measured before and after expansion of the sample from a single volume ( $V_A$ ) into the combination of the original volume and a second volume ( $V_A+V_B$ ).

Some of the gas goes through a sequence of isothermal expansions into a chamber, which is evacuated every time the expansion takes place. Both virial coefficient and gas density can be calculated with this method. The ratio of the densities before and after the expansion is calculated for each expansion:

$$\rho_i = \rho_m \pi_\infty^{m-i} \prod \left[ \frac{1 + \gamma_{ab} P_j}{1 + \gamma_a P_{j-1}} \right] \quad (4)$$

where

$$\pi_\infty = \lim_{P \rightarrow 0} \frac{V_a + V_b}{V_a} \quad (5)$$

In equation 4,  $\gamma_a$  and  $\gamma_{ab}$  are the pressure distortions of the volumes  $V_a$  and  $(V_a + V_b)$  respectively,  $\pi_\infty$  is the zero pressure cell constant,  $\rho_m$  is the density at the lowest pressure and subscripts  $i$  and superscript  $m$  indicate the value after the  $i$ -th and  $m$ -th (last) expansions, respectively.

A serious problem that can affect the Burnett apparatus is adsorption of the sample gas on the inner surfaces of the measuring cell [32]. Also a Burnett apparatus is difficult to automate fully because of frequent valve operations. Because of error accumulation, very high precision is necessary in the pressure measurements, which necessitates use of high-quality dead-weight gauges.

The adsorption affect can be minimized by the using two cells with a surface area ratio almost equal to the volume ratio [33]. Eubank et al. have formulated new adsorption correction schemes, based upon the BET adsorption isotherm [34].

#### **2.2.4 Continuously Weighed Pycnometer Method**

In the continuously weighed pycnometer method, the mass of the sample is determined by direct weighing of the cell. A typical pycnometer consists of a weight measurement system, constant temperature bath, temperature control system and data acquisition system, a volume bellows cell for changing pressure and density without transferring mass, and a high vacuum system [35]. The major component of this method is a constant volume pycnometer suspended from a digital balance. The pycnometer can be filled and evacuated with an extension tube that enables faster measurements and reduces operator errors. The mass of the pycnometer when empty and when filled with fluid is measured by a digital balance. The density of the fluid being measured at constant temperature and pressure is calculated from the measured mass value of the fluid and the known volume of the pycnometer.

One disadvantage of this method is that the long feed tube exposes part of the sample to ambient temperature making it impossible to measure mixture densities when the sample exists as one phase at the cell set point temperature and at room temperature.

## 2.2.5 Hydrostatic Buoyancy Methods

The hydrostatic buoyancy force technique is based upon Archimedes' Principle. Basically, Archimedes' Principle states "when a solid body is immersed in a fluid, it displaces a volume of fluid the weight of which is equal to the buoyancy force exerted by the fluid on the sinker." This means that the buoyancy force is proportional to the density of the fluid in the measuring cell under pressure. This principle can be applied to determine the gas density of any pure fluid or mixture. Historically, improvements have appeared in the application of buoyancy method based densimeters.

### 2.2.5.1 Classical Methods

In classical hydrostatic buoyancy densimeters, an object (sinker hereafter), usually a sphere or cylinder, is suspended from a commercial digital balance by a thin wire. The fluid is kept in a pressure cell at constant temperature using a temperature control mechanism. The sinker is submerged in the fluid and weight of the sinker is constantly monitored. According to Archimedes' principal, the apparent loss in the true weight of the sinker is equal to the weight of the displaced fluid. Density of the fluid results from:

$$\rho = \frac{m_v - m_a}{V_s(T, P)} \quad (6)$$

In above equation  $m_v$  is the 'true' mass of the sinker in vacuum,  $m_a$  is 'apparent' mass of the sinker in the fluid and  $V_s$  is the calibrated volume of the sinker, which is a function of temperature and pressure.

In such densimeters, several corrections are necessary to reduce the effect of surface tension between the sample liquid and the immersed part of the wire, and the effect of the buoyant force of air on the masses of the analytical balance. Zero shift of balance readings, buoyancy forces on auxiliary devices, adsorption effects and surface tension may reduce the accuracy of such measurements [36].



### 2.2.5.2 Magnetic Suspension Devices

To overcome limitations in achievable accuracy, the need for frequent calibration of the apparatus with reference fluids, complexity of operation, limitations on temperature and pressure, Kleinrahm and Wagner [25] introduced an MSD based upon magnetic levitation of the sinker in the measuring cell. The novelty of the magnetic suspension coupling was that it used non-physical-contact force transmission between the sinker in the pressurized cell and the weighing balance at atmospheric pressure, thus allowing a cell design that covered a very wide temperature and pressure range [37]. Then, Kleinrahm and Wagner [36] modified the hydrostatic buoyancy force method by introducing an alternative force transmission method in which they levitated two sinkers through a magnetic suspension coupling. By compensation for surface tension, buoyancy, adsorption effects and shifts in zero-point of the balance, a two-sinker MSD improved the accuracy of the density measurements.

Operation of a two-sinker MSD is rather complex and its advantage is not required for medium or high-density measurements encountered in many practical applications. To extend the instrument range towards higher temperatures and pressures, Wagner et al. [32] have developed a single-sinker densimeter. Although the single sinker design is much simpler than that of the two-sinker densimeter, it is still possible to perform high-accuracy density measurements at relatively low gas densities by applying some of the advantageous features of the two sinker device [38]. The single-sinker densimeter also operates based upon Archimedes' principle and the force transmission comes from levitation of the sinker in the measuring housing of the high-pressure cell.

Klimeck *et al.* [39] have concluded that the accuracy of density measurement from a single-sinker densimeter is lower than that from a two-sinker densimeter especially at low densities because it lacks compensation for the adsorption effect. Moreover, the force transmission error has more effect on total density measurement uncertainty than observed in a two-sinker densimeter. Also for small densities, having the load compensation system outside of the measuring cell is less effective than having it inside as with the two-sinker densimeter.

### 3. MAGNETIC SUSPENSION DENSIMETERS AND FORCE TRANSMISSION ERROR PHENOMENA

#### 3.1 Introduction

A hydrostatic balance densimeter combined with magnetic suspension coupling mechanism currently is the most accurate densimeter for collecting  $P$ - $\rho$ - $T$  data over wide ranges of temperature, pressure and density [40]. Buoyancy-based magnetic suspension densimeters using Archimedes' Principle were first introduced by Beam and Clarke in 1962 [41]. In that design, the floating object (sinker) was a magnetic, ferrous material. They used several solenoid coils in the pressure environment to levitate the sinker. The buoyancy force on the sinker was determined from the coil required to lift and suspend the sinker in the density-measuring cell. After Beam and Clarke, Brachthäuser et. al. [42] developed the modern magnetic suspension densimeter equipped with non-magnetic sinkers, coupling of a permanent magnet and an electromagnet connected to a separated digital balance. The Brachthäuser densimeter was initially a single sinker densimeter. Kleinrahm and Wagner [36] designed and developed more complicated two sinker densimeters.

Because the magnets are coupled by a magnetic field, the coupling assembly is affected by nearby magnetic fields and any magnetic field associated with the fluid being measured. This phenomenon is the force transmission error (FTE).

#### 3.2 Two Sinker Densimeters

As mentioned section 3.1, magnetic levitation hydrostatic buoyancy force method based densimeters first introduced by Kleinrahm and Wagner [25, 36]. This initial design included two sinkers. The novelty of this type of apparatus comes from the contactless force transmission of the sinker weight to the digital scale through the permanent magnet and electromagnet. This design allows wide temperature and pressure range operation density measurements [37].

The two sinkers, one a disk or a ring and the other a sphere or a cylinder had the same mass, surface area and surface properties but vastly different volumes.

Schematic for two sinker densimeter is given in figure 7. The density of a fluid was calculated by measuring true masses of the sinkers under vacuum,  $\Delta m_v$ , and the apparent masses of the sinkers in pressure environment,  $\Delta m_a$ . Provided that the volumes of the sinkers,  $V_D$  (disc sinker) and  $V_{SP}$  (sphere sinker) are calibrated and know. So the following equation can be written for density calculations based on the data that is collected from two sinker densimeter.

$$\rho = \frac{\Delta m_a - \Delta m_v}{V_{SP} - V_D} \quad (7)$$

The primary reason of two-sinker magnetic suspension densimeter was conduct very accurate measurements for the saturated liquid and saturated vapor densities of pure fluids. However, due to its design, it can be also used for homogenous liquid and homogenous gas sample measurements. Use of more than one sinker eliminates many problems that are observed in single sinker MSD and other hydrostatic buoyancy force based density measuring devices.

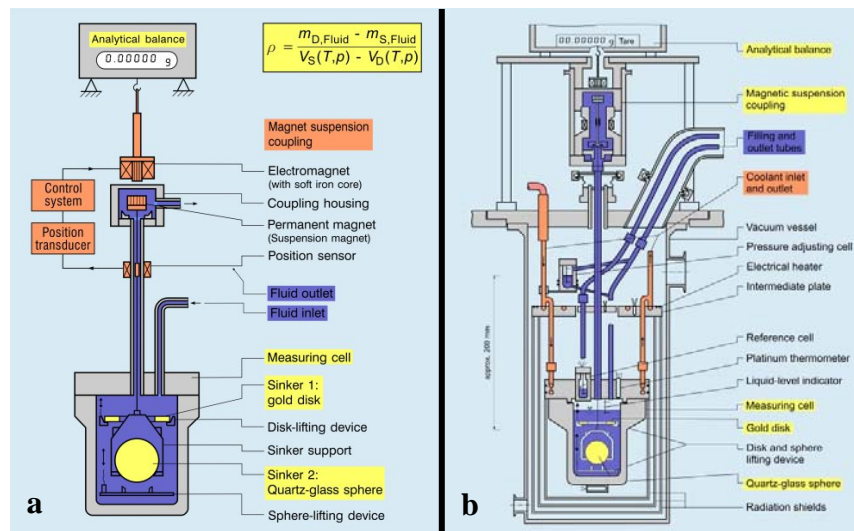


FIGURE 7. (a) Basic scheme for two-sinker MSD, (b) Wagner and Kleinrahm's two-sinker MSD [15, 43].

The biggest advantages of two-sinker MSD are that the use of two sinkers improves the accuracy by compensation of surface tension, buoyancy, adsorption effects and shifts in zero point of the balance [22]. The two-sinker densimeter of Kleinrahm and Wagner [36] had an operating temperature range of 60 to 340 K and a pressure range of up to 12 MPa with an uncertainty in density measurement of  $\pm(0.01 \text{ to } 0.02)\%$  (IUPAC, 2003).

The two-sinker densimeters have been used to measure the several essential pure fluids, for instance methane, carbon dioxide, argon, ethene, ethane, nitrogen, sulphur hexafluoride, dichlorodifluoromethane (R 12), and chlorodifluoromethane (R22) [44].

### 3.3 Single Sinker Densimeters

Just like two-sinker densimeters, single sinker densimeter uses the Archimedes' Principle of buoyancy. In single sinker densimeters overall working principle is the same as two-sinker densimeter while instead of dual sinkers; only one sinker is used to determine the density of the fluid that is measured in the high pressure cell. The single-sinker densimeter has a separate thermostated magnetic suspension coupling housing and a pressure cell for the fluid sample and the sinker.

In mid 90's, European Groups started to use single sinker Densimeter mostly for pure liquid and gas density measurements. In 1995 and 1996, Blanke et. al. investigated vapor-liquid equilibria of pure components and mixtures such as tetrafluoroethane (R134a), 1-Chloro-1-2-2-2-tetrafluoroethane (R124), R125 and difluoromethane (R32) in the temperature range from 120 K to 395 K at pressures up to 5 MPa [45, 46]. They measured vapor and liquid densities separately with the system they developed. They used single sinker Densimeter to measure liquid density and similar type densimeter for gas density measurements which is connected to the first one for temperature control and adjusting and measuring the saturation pressure. They reported total uncertainty in pure component density measurement as 0.02% for the saturated-liquid region and for the saturated-vapor region as 0.1%.

In 1998, Watson et. al. at the National Engineering Lab (NEL) in Glasgow, Scotland, have commissioned a single-sinker densimeter primarily designed for liquid density measurements with in the temperature range of 233 K to 423 K and pressures up

to 30 MPa with total uncertainty in density 0.015% [47]. Later in 1999, Iwagai et. al. have used a single sinker densimeter to measure saturated vapor and saturated liquid densities of R32 and pentafluoroethane with the temperature range of 223 K to 423 K and pressures up to 15 MPa [48]. According to pure CO<sub>2</sub> measurements, the uncertainty is estimated to be 0.03% [15]. In Japan, Kuramoto and Fujii [49] improved the original design of Kinoshita and Fujii [50] in 2001. The single sinker densimeter that Kuramoto and Fujii improved used for very accurate density measurements of reference fluids such as n-nonane, n-tridecane, water and 2, 4-dichlorotoluene which in turn used in calibrating vibrating tube densimeters. This densimeter covers a temperature range of 253 K to 473 K at pressures up to 20 MPa.

A similar compact sinker densimeter that we used in Texas A&M University Thermodynamics Research Group was also built at the University of Valladolid for measuring pure gases and gas mixtures within the temperature range of 233 K to 523 K at pressures up to 20 MPa and densities up to 20 kg m<sup>-3</sup> [51]. Typical schematics of such single sinker MSD is shown in figure 8.

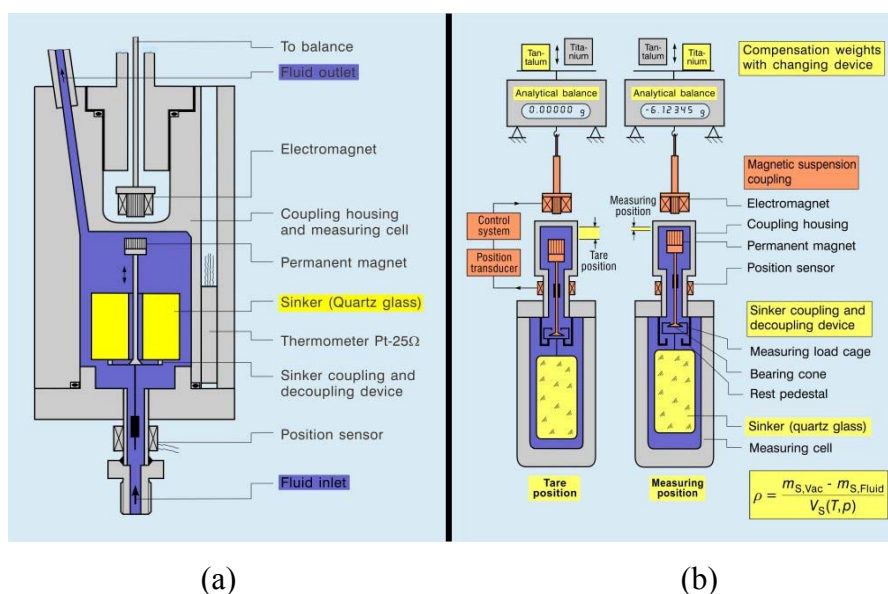


FIGURE 8. (a) Basic scheme for single-sinker MSD, (b) Operating modes of single-sinker MSD [15, 43].

Villamañán and Chamorro reported the total uncertainty in density measurements as  $\pm (0.01\% + 0.004 \text{ kg m}^{-3})$ . Another low pressure single sinker magnetic suspension densimeter specifically used for vapor-liquid equilibrium of binary mixtures of natural-gas components developed in Universität für Bodenkultur in Vienna, Austria by Saleh and Wendland [52]. They have in-situ liquid level indicator in the measuring cell. By knowing the total volume of the measuring cell housing, vapor phase and liquid composition and fractions and total amount of substance, they aimed to obtain saturated-vapor phase density after measuring the density of the saturated-liquid phase density. They measured pure water, CO<sub>2</sub> (saturated-liquid densities), and nitrogen (supercritical gas densities) in the temperature range of 213 K to 373 K at pressures up to 6.7 MPa [52].

In this work we built compact single sinker magnetic suspension densimeter apparatus constructed by Rubotherm Präzisionsmesstechnik GmbH, Germany and its ancillary equipment for density measurements. The apparatus has an accuracy specification from the manufacturer of  $\pm (0.03\% + 0.005 \text{ kg/m}^3)$  for densities in the range (0 to 2,000) kg/m<sup>3</sup> over a temperature range of 193.15 to 523.15 K and a pressure range up to 200 MPa with a maximum pressure at 523.15 K of 130 MPa. Such high pressure and wide temperature range makes our apparatus unique among all magnetic suspension densimeters in use presently, worldwide. Details of the setup will be discussed in section 4 in more detail.

### **3.4 Force Transmission Error in Magnetic Suspension Densimeters**

A magnetic suspension coupling transmits, to the balance, the weight of the sinkers across a coupling housing, which separates the fluid from the atmosphere. The coupling consists of an electromagnet (in air) and a permanent magnet (in the fluid). The permanent magnet is linked with a lifting device to pick up a sinker for weighing. With proper design, the efficiency of this force transmission is nearly one, but the coupling will be slightly influenced by nearby magnetic materials, external magnetic fields, and the fluid being measured. These give rise to a “force transmission error” (FTE) that must be accounted for to realize the full accuracy of this technique. The FTE can refer to

either the error in a weighing carried out using a magnetic suspension coupling or the error in a density determination arising from magnetic effects. The FTE can be divided into two parts. The first arises from the magnetic characteristics of the apparatus itself. The magnetic susceptibility of the fluid surrounding the magnets also influences the FTE. Because the position of the permanent magnet inside the coupling housing varies as the load on the coupling changes, the distribution of fluid around the magnet varies for the different weightings and this will affect the FTE; this is the “fluid-specific effect”.

### 3.4.1 Force Transmission Error in Single Sinker Magnetic Suspension

#### Densimeters

For a single sinker densimeter, the weighing sequences are different from those in a two sinker densimeter because there is only one sinker involved in the density measurement operation. Single sinker operation includes two different measurement positions; zero point (ZP) and measurement point (MP). In ZP position, the permanent magnet is raised by the electromagnet and the sinker stays on the seat in the measuring cell.

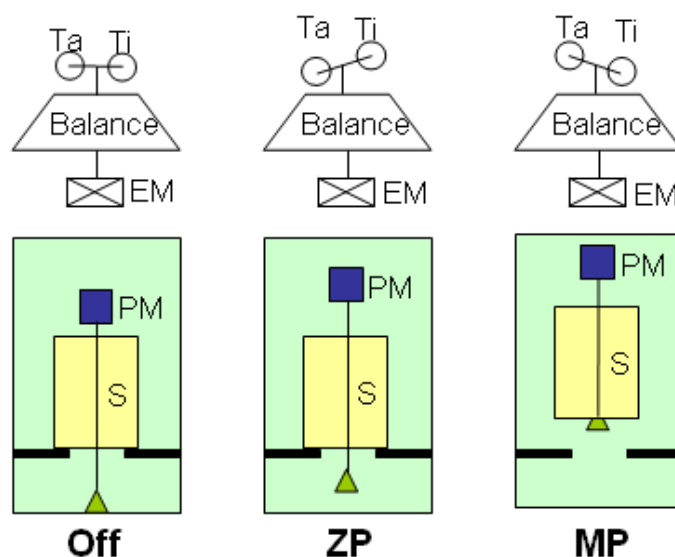


FIGURE 9. Single Sinker MSD weighing positions.

After the tare of the balance in ZP, the system goes to MP in which the sinker is raised by the electromagnet. One compensation weight is placed on the balance pan each time by using an external weight changing device. FTE analysis for single sinker densimeter is similar to that for two sinker densimeters.

In all three positions shown in figure 9, we weigh the electromagnet. A tantalum (Ta) weight is placed on the balance mini pan in ZP position and a titanium (Ti) weight is placed on the balance mini pan in MP position.

$$W_1 = \alpha \left[ \phi (m_{pm} - \rho_f V_{pm}) + m_{em} + m_{c2} - \rho_{air} (V_{em} + V_{c2}) + W_{zero} \right] \quad (8)$$

$$W_2 = \alpha \left\{ \phi \left[ m_s + m_{pm} - \rho_f (V_s + V_{pm}) \right] + m_{em} + m_{c1} - \rho_a (V_{em} + V_{c1}) + W_{zero} \right\} \quad (9)$$

If we subtract equation 9 from equation 8 and solve the equation for  $\rho_f$ , we get:

$$\rho_f = \frac{\phi m_s + (m_{c1} - m_{c2}) + (w_1 - w_2)_f / \alpha + \rho_a (V_{c2} - V_{c1})}{\phi V_s} \quad (10)$$

Volumes of external weights are designed to be the same in order to cancel the air buoyancy on the weights.  $V_{c1} \approx V_{c2}$  applied to equation 10 gives the following equation:

$$\rho_f = \rho_s + \frac{(m_{c1} - m_{c2}) + (W_1 - W_2)_f / \alpha}{\phi V_s} \quad (11)$$

If we make a measurement with a vacuum in the cell,  $\rho_f = 0$  and;

$$\phi_0 = \frac{(m_{c2} - m_{c1}) + (W_2 - W_1)_0 / \alpha}{m_s} \quad (12)$$

and the general empirical formulation for  $\phi$  is:

$$\phi = \phi_0 + \varepsilon (\rho_c \chi) (\rho_s / \rho_c) (\rho_f / \rho_s) \quad (13)$$

Finally; equation 13 is plugged into equation 11 to obtain:

$$\rho_f = \rho_s + \frac{(m_{c1} - m_{c2}) + (W_1 - W_2)_f / \alpha}{\left[ \phi_0 + \varepsilon (\rho_c \chi) (\rho_s / \rho_c) (\rho_f / \rho_s) \right] V_s} \quad (14)$$

If equation 12, which is derived for vacuum conditions, is plugged into equation 14, the most general form of correcting raw density data for single sinker MSD is:



$$\rho_f = \rho_s + \frac{(m_{c1} - m_{c2}) + (W_1 - W_2)_f / \alpha}{\left[ \frac{(m_{c2} - m_{c1}) + (W_2 - W_1)_0 / \alpha}{m_s} + \varepsilon (\rho_c \chi) (\rho_s / \rho_c) (\rho_f / \rho_s) \right] V_s} \quad (15)$$

or;

$$\rho_f = \rho_s - \frac{(m_{c1} - m_{c2}) + (W_1 - W_2)_f / \alpha}{\left[ \frac{(m_{c1} - m_{c2}) + (W_1 - W_2)_0 / \alpha}{\rho_s} - \frac{\varepsilon (\rho_c \chi) (\rho_s / \rho_c) (\rho_f / \rho_s)}{\rho_s} \right]} \quad (16)$$

In equation 15 and 16, mass of external weights, mass of sinker, volume of sinker, density of sinker, magnetic susceptibility and the critical density of the fluid being measured in the measuring cell are known.  $(W_1 - W_2)_0$  and  $(W_1 - W_2)_f$  are obtained directly from the balance readings during the measurements. The balance calibration factor  $\alpha$  is 1.00015 the same as for a two sinker MSD as given in [53]. We applied equation 12 to calculate coupling factors at vacuum conditions. It is 1.000200569 for the single sinker MSD that we have in Texas A&M University.

To evaluate the apparatus constant,  $\varepsilon$ , we have measured pure nitrogen and pure carbon dioxide at several pressures and several isotherms. We use NIST-12 for nitrogen and carbon dioxide to obtain  $\rho_f$  at our measured conditions and solve equation 15 (or 16) for  $\varepsilon$ . For our apparatus, NIST calibrated external weights, mass of sinker, volume of sinker values and sinker density value are:

$$\begin{aligned} m_{c1} &= 41.61804g \\ m_{c2} &= 11.23311g \\ m_s &= 30.39159g \\ \rho_s &= 4508.44 kg/m^3 \end{aligned}$$

Value of  $\rho_s$  adjusted with the pressure is the ambient value. For natural gas mixtures, it is reasonable to assume  $\rho_c \chi$  equals  $-2.5 \cdot 10^{-6}$ . We analyzed the pure component data based upon the equations derived above for a single sinker densimeter. We have observed a temperature and pressure dependency on fluid specific constant  $\varepsilon$  shown in figure 10.

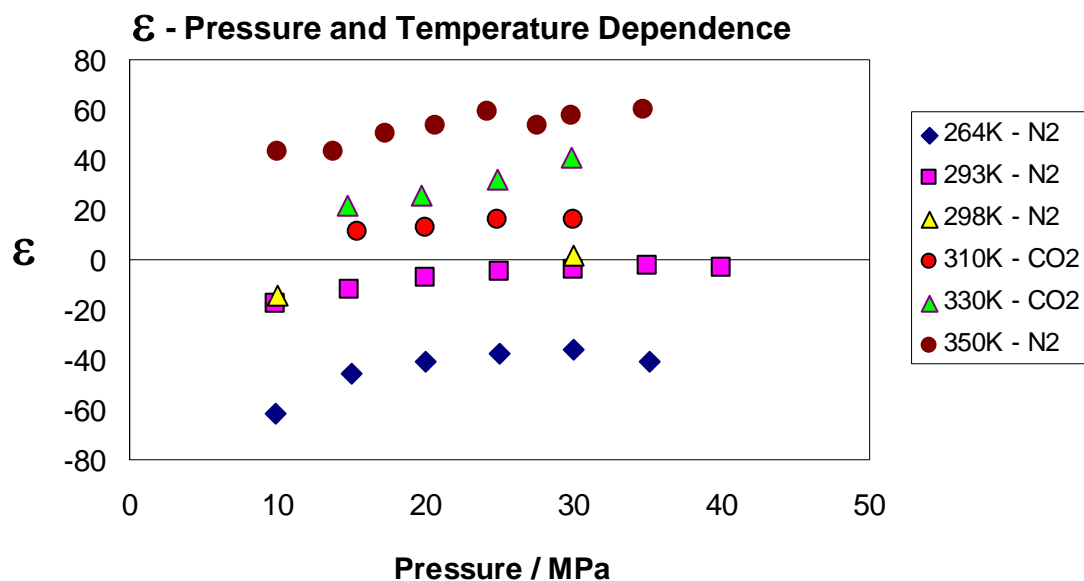


FIGURE 10. MSD apparatus constant pressure and temperature dependence.

We have fit the data and observed that all the plots have same slope and intercepts have linear behavior with temperature. These results are presented in figures 11 and 12.

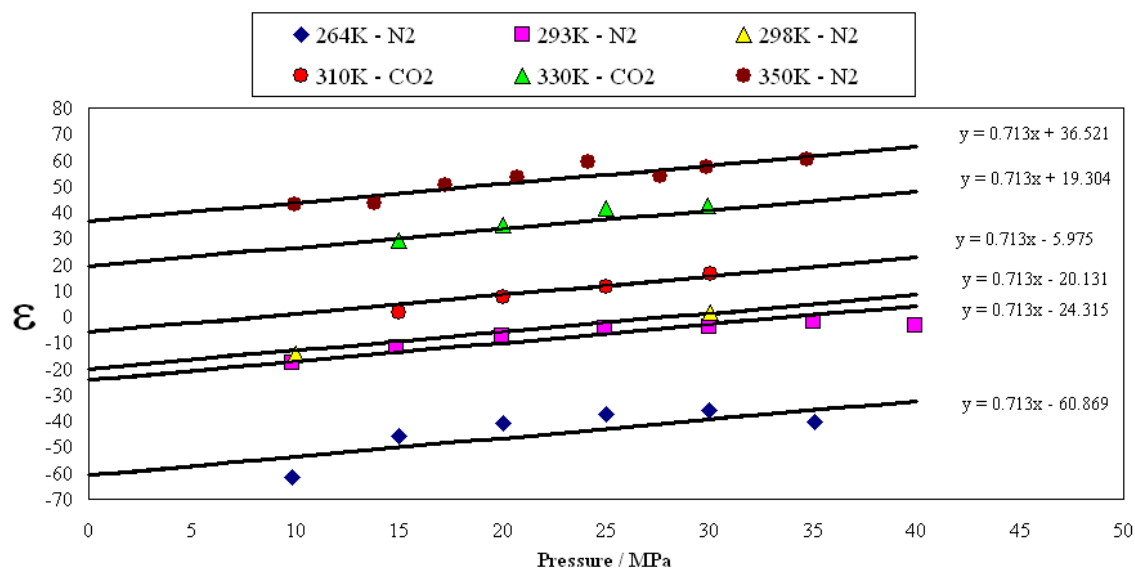


FIGURE 11. Experimentally calculated MSD fluid specific constant.

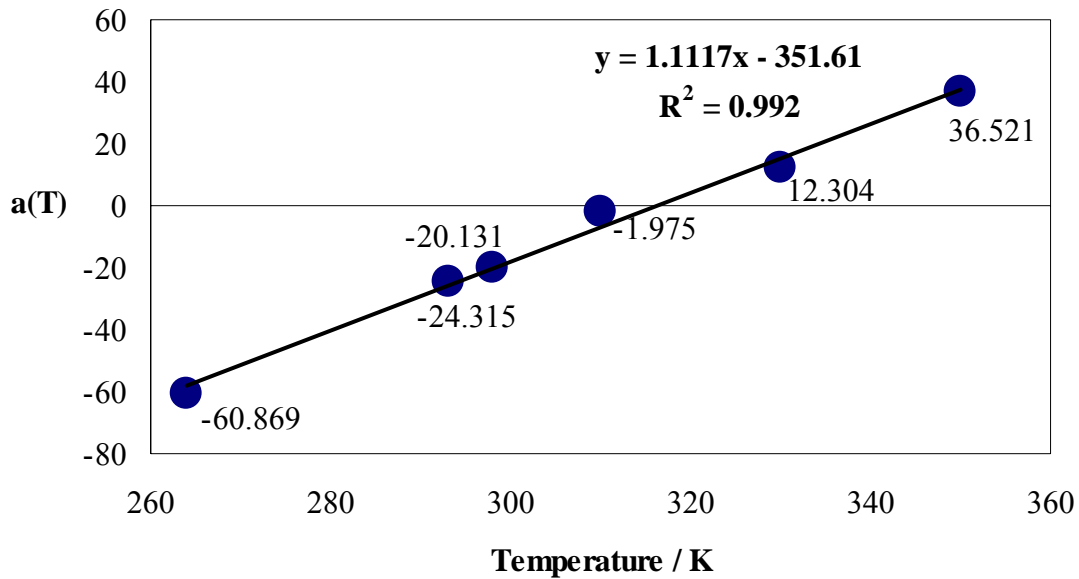


FIGURE 12. Temperature dependence of intercept for  $\varepsilon(P,T)$  equation.

Based upon above figures 10 and 11, we can say that  $\varepsilon$  is a function of temperature and pressure and the intercept for the proposed equation for  $\varepsilon$  has linear temperature dependence. Therefore, we can argue that  $\varepsilon$  at specific temperature and pressure can be calculated from;

$$\varepsilon = 0.713 \times P + 1.1117 \times T - 351.61 \quad (17)$$

where P is in MPa and T is in K. However, the fluid specific error must be tested with an additional sinker. During the application of the derived equations for fluid specific error, the NIST-12 database is used for pure components. This database has experimental data mostly up to 35 MPa. For higher pressures, extrapolated data is used.

### 3.4.2 Force Transmission Error in Two Sinker Magnetic Suspension Densimeters

McLinden et. al. [53] made a detailed analysis of the effect of FTE for the recently developed two sinker MSD previously described [54] in NIST Boulder. Brief analysis of the FTE correction is discussed in Appendix A.

## **4. EXPERIMENTAL SETUP, CONTROL SYSTEMS AND DATA ACQUISITION OF MAGNETIC SUSPENSION DENSIMETER**

### **4.1 Introduction**

We have re-constructed the single-sinker MSD that Patil [22] used previously, after the move of Artie McFerrin Department of Chemical Engineering of Texas A&M University to a new building. This section contains a description of a single sinker magnetic suspension densimeter, its temperature control system and stable magnetic levitation control system. Also, the section contains discussion and photos of the data acquisition scheme and interfaces.

### **4.2 Overview of the MSD System**

The MSD system includes several principal and ancillary instruments. Figure 13 presents a system overview. The principal instruments are: the magnetic suspension coupling system, the high pressure cell, the magnetic levitation control box and the digital balance. The ancillary instruments include: a cylinder storage hot box (block box), feed charging and discharging manifolds, temperature control heat exchangers around the high pressure cell, pressure and temperature measurement systems, a compressor, a vacuum system, a heating/cooling liquid constant temperature circulation bath and a personal computer for data acquisition and control. In addition, a differential pressure indicator (DPI) and a dead weight gauge (DWG) are used for pressure transducer calibrations and a triple point of water (TPW) cell is available to check the calibration of the PRT.

### **4.3 Feed Manifolds and Cylinder Storage**

An insulated and explosion proof steel box with dimensions 1.83 m tall x 0.61 m deep x 0.81 m wide was used to store the natural gas mixture sample cylinders at temperatures above their respective cricondentherms (CT) to prevent condensation and adsorption of the heavier components. The box has a 600 watt heater and an adjustable

analog thermostat that can maintain cylinder temperatures between ambient and 95 °C within  $\pm 2$  °C. The pure gas cylinders for argon, methane, ethane, carbon dioxide, helium and nitrogen were also stored in the hot box.

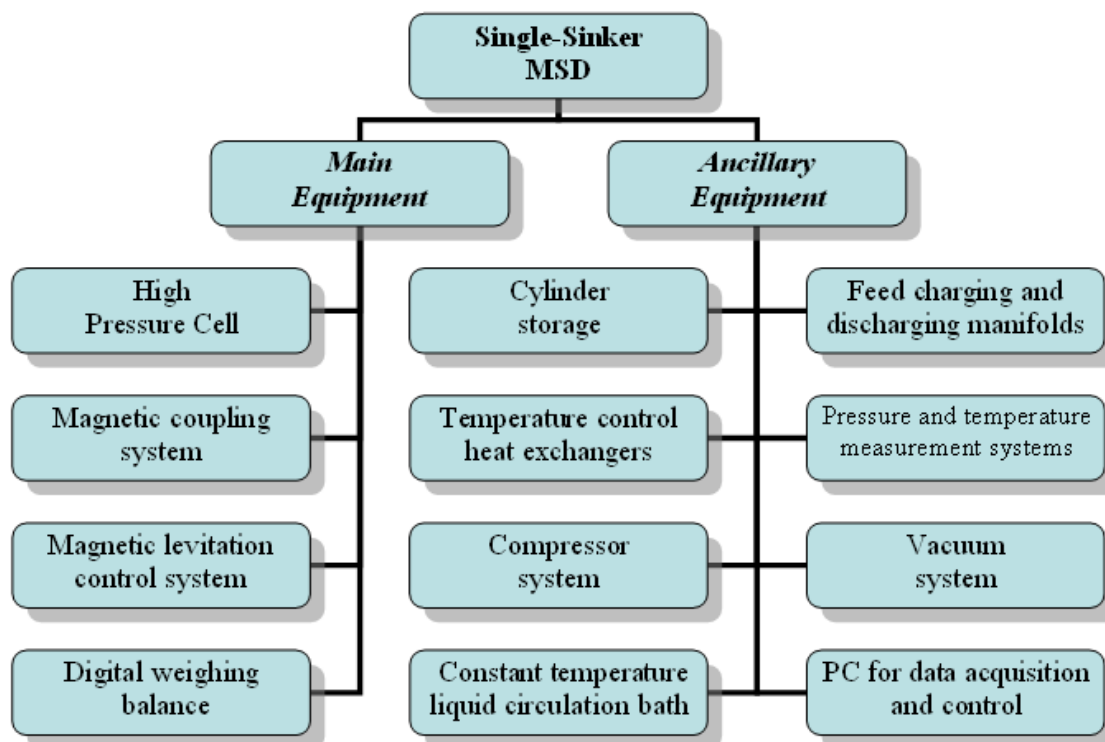


FIGURE 13. MSD system overview with main and ancillary equipments.

The hot box is connected to a gas pressurizing manifold with low pressure Swagelok tubes. This manifold is used to pressurize the gas sample and charge the gas to the measuring cell. A Haskel compressor (DC), model AG-303, compresses the samples up to a maximum pressure of 39,000 psi. Figure 11 is a detailed flow diagram of the gas pressurizing manifold. A bypass valve, V2, isolates the compressor when it is not needed for low pressure measurements.



Other than calibration, during density measurements, V13 is kept closed. Manifold 2 is installed enables pressure monitoring. It contains a vacuum pump (VP2), a hand pump (HP2) and a DHI force balance. Additionally, a vent to atmosphere in this manifold permits checks for offsets of the transducers at atmospheric pressure. From time to time, we use this valve to check the drift of the transducer at ambient pressure. The DHI force balance can be calibrated against standard weights, and it can be used to calibrate the transducers instead of the DWG. Details of the operations of the valves and the procedures for density measurements appear elsewhere [22]. In the current embodiment, the DHI force balance pressure head handles up to 2,000 psi and the 2,000 psi pressure transducer is calibrated using this arrangement. If needed, VP2 can be used to evacuate the system as a backup to VP1 which is the main vacuum pump. Since 2006, VP2 has provided vacuum insulation space for the thermostat. Figure 15 is a detailed flow diagram of the manifold. A three-way valve, VM, isolates the cell from the pressurizing manifold in order to minimize pressure fluctuations inside the MSD cell.

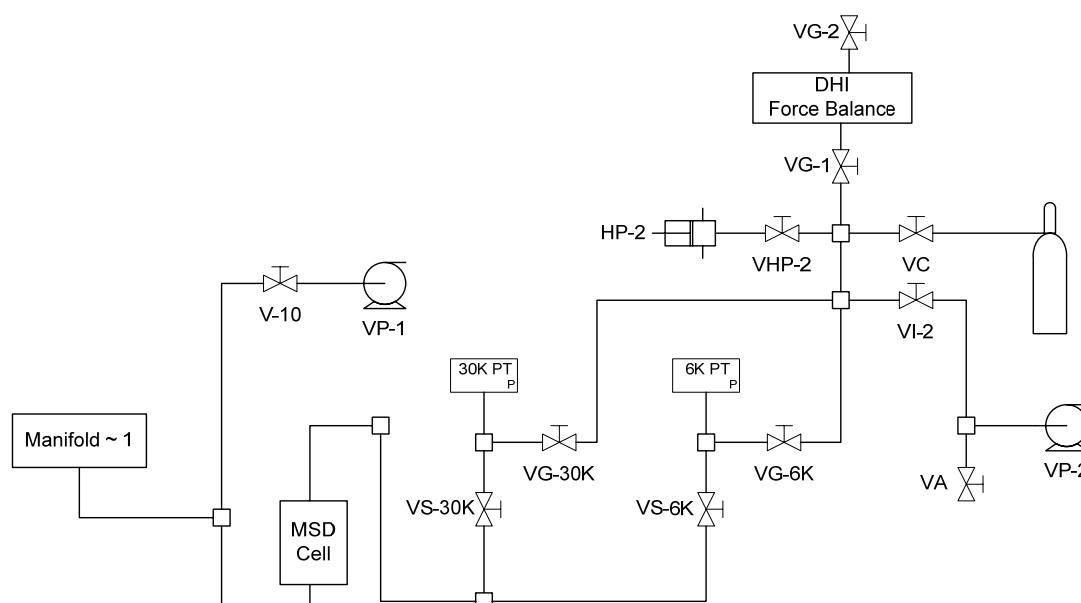


FIGURE 15. Manifold 2 flow diagram.

The single sinker MSD levitates the sinker in the measuring environment using a magnetic coupling of an electromagnet and a permanent magnet. Therefore, any object or instrument that has a magnetic field affects the density measurements and must be kept a minimum 1m radius circle from the magnets. Some of the valves have magnetic stems, and they must be outside of the 1 m radius circle.

#### **4.3.1 Pressure Transducer Calibration**

The pressure transducers require occasional calibrations because from time to time the slope and the offset of the transducer calibration curve might change. For this reason, a DPI and DWG assembly is available for in-situ calibration of the transducers at different temperatures. The gas pressure inside the pressure transducer is balanced with the calibrated weights that are placed on a floating piston in a Ruska DWG.

The DPI is a differential pressure cell and an electronic null indicator designed to detect minute pressure differences in both low- and high-pressure systems. The DPI cell consists of two pressure chambers separated by a thin stainless steel diaphragm. The DPI diaphragm acts as an interface between measured gas on one side (connected through V13) and oil going into DWG on the other side. A differential pressure across the diaphragm causes diaphragm to deflect. The diaphragm assembly positions a core within a coil of a differential transformer located within the upper pressure chamber. The core-coil relationship causes an electrical output that is a function of the diaphragm displacement and the differential pressure. The electrical output is indicated by the Electronic Null Indicator.

Factors such as elastic distortions of the piston and cylinder, temperature of the piston and cylinder, effects of gravity and buoyancy, hydraulic and gaseous pressure gradients from the DPI reference plane to pressure transducer, and liquid surface tension affect the performance of the DWG [44, 55]. Figure 16 is a detailed diagram for the Ruska DWG and DPI facility.



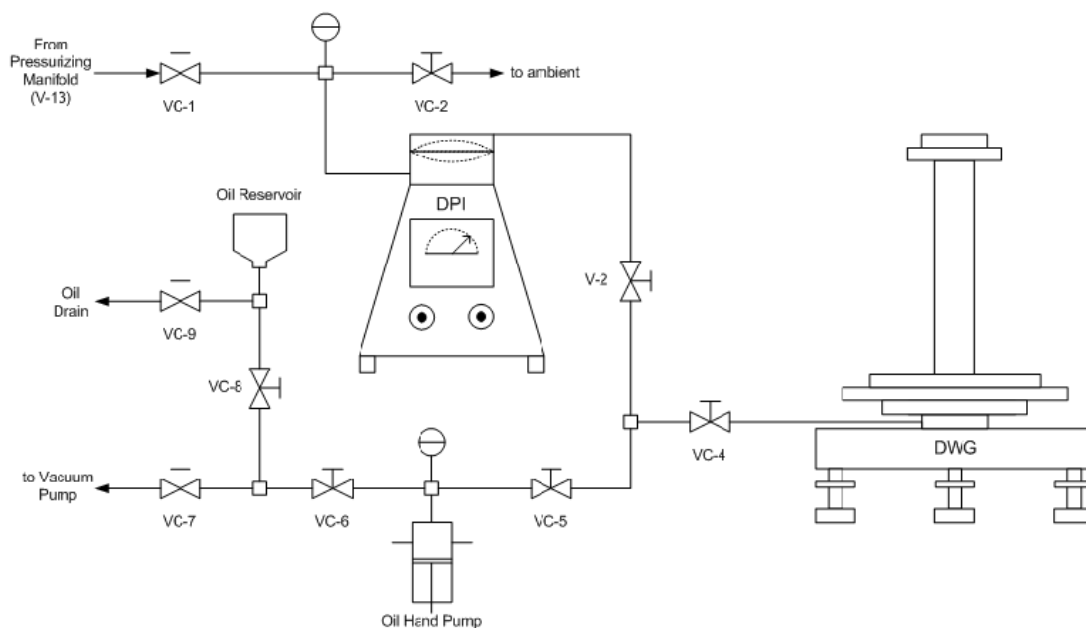


FIGURE 16. Diagram for Ruska DWG and DPI facility.

#### 4.3.2 Vacuum System

The vacuum pumps, VP-1 and VP-2, in Figures 14 and 16 are 0.5 HP Varian model SD-200 mechanical pumps with nominal rotational speeds of 1500 t/min and free air displacement capacities of 10 m<sup>3</sup>/h. VP-1 can create a vacuum of 5 mTorr at its inlet port and is used as a roughing pump to evacuate the MSD high pressure cell by closing V7 and opening VI-1 in Figure 14. A thermocouple vacuum gauge tube is the sensor for vacuum measurement with an analog vacuum gauge controller having a range of 1 to 2,000 mTorr. From time to time (once in 6 months), a molecular sieve trap is activated to absorb any oil that has migrated from vacuum pump to the vacuum pipe system. The molecular sieve particles are regenerated by heating the trap with an axially placed rod heater that caused desorption of the vacuum pump oil while closing valve V-14 and running VP-1.

#### 4.3.3 Compressor System

An oil free, air driven and single stage Haskel compressor, model AG-303 compresses the gas samples.

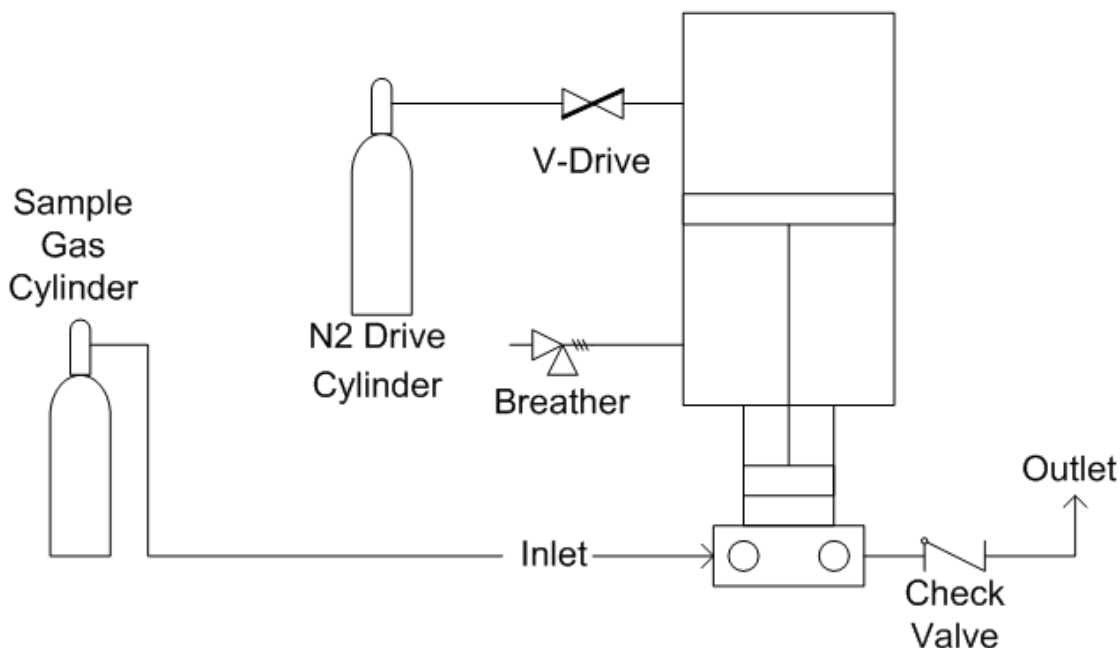


FIGURE 17. Haskel compressor and nitrogen drive.

This compressor can reach a maximum pressure of 39,000 psi using a minimum external air drive pressure of 120 psi to drive the compressor shaft. Better performance results from keeping the drive pressure at 150 psi. Also, the suction side of the compressor requires a minimum of 500 psi. The manufacturer included separate check-valves to prevent back flow of the compressed gas both at the suction side and at the discharge side of the compressor. In August 2006 after deterioration of the original check valve at the compressor discharge line, we installed an external check-valve that has a pressure rating of 60,000 psi. Most of the compressor sample suction line is outside the heated pressurizing manifold. Therefore, Omega rope heaters are used to heat this section to prevent condensation for samples that have high cricondentherms. Figure 17 diagrams the compressor suction line, discharge line and check valves.

#### 4.4 High Pressure Cell and Balance

Figure 18 is the overall scheme for the MSD including the measuring cell and the electronic balance. Dimensions in this figure are from the original single sinker MSD manual and are in mm [56]. The MSD has two main parts, a weighing balance and high-pressure cell. The connection between the balance and the cell is through a shaft-like tube through which the electromagnet (EM) passes.

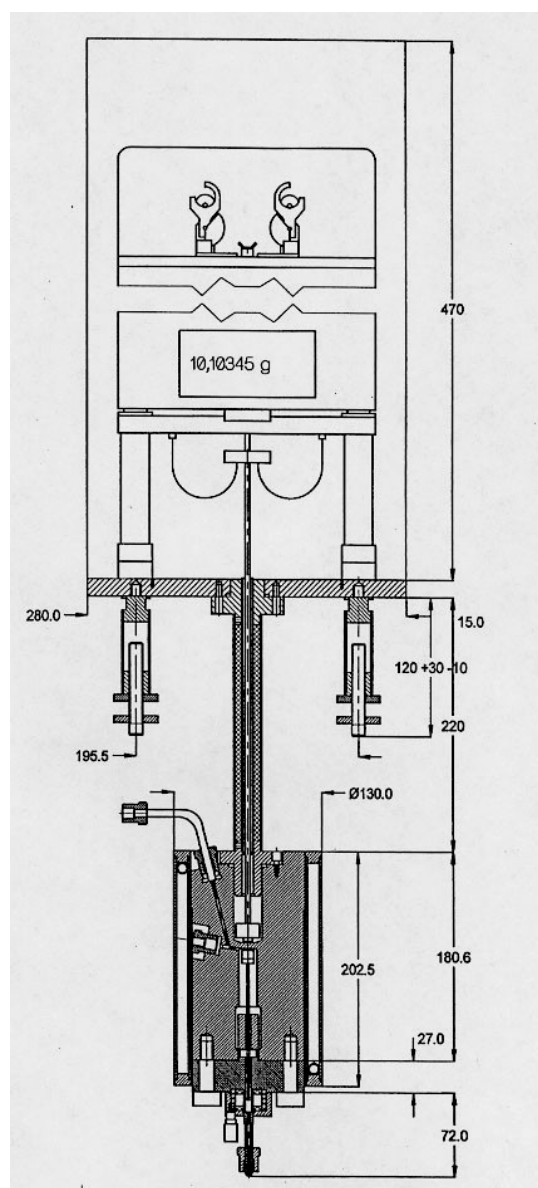


FIGURE 18. The Entire MSD. Scaled figure scanned from Rubotherm manual [56].

The weighing balance rests on a balance frame and this frame sits on the base plate. The connection tube screws into the balance base plate. The weighing balance, weighing balance frame and balance base plate appear in Figure 19.

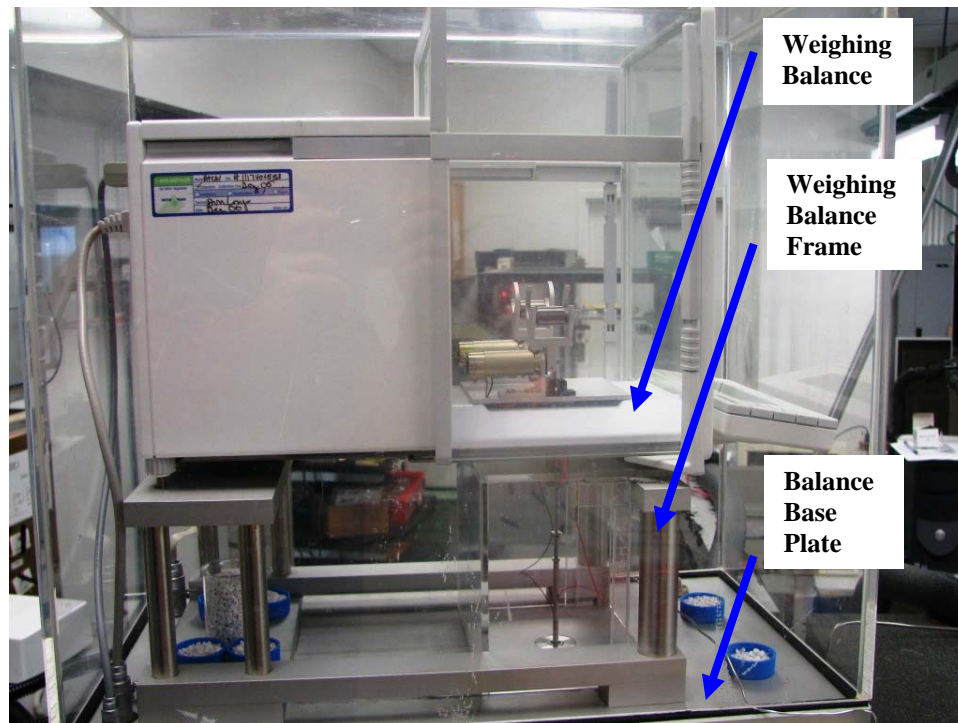


FIGURE 19. Weighing balance, weighing balance frame and balance base plate.

The weighing balance, weighing balance frame and balance base plate are supported by four height-adjustable feet with threading and locking nuts. These feet sit on the 1/2" thick hardened aluminum platform. This aluminum platform rests upon concrete blocks. The aluminum frame is supported on two towers with a 42.5 cm wide space between them formed by stacking six levels of cinder blocks with layers of carpet between every two levels to absorb vibrations. Figure 20 presents the overall picture of the concrete blocks, aluminum platform and weighing balance.

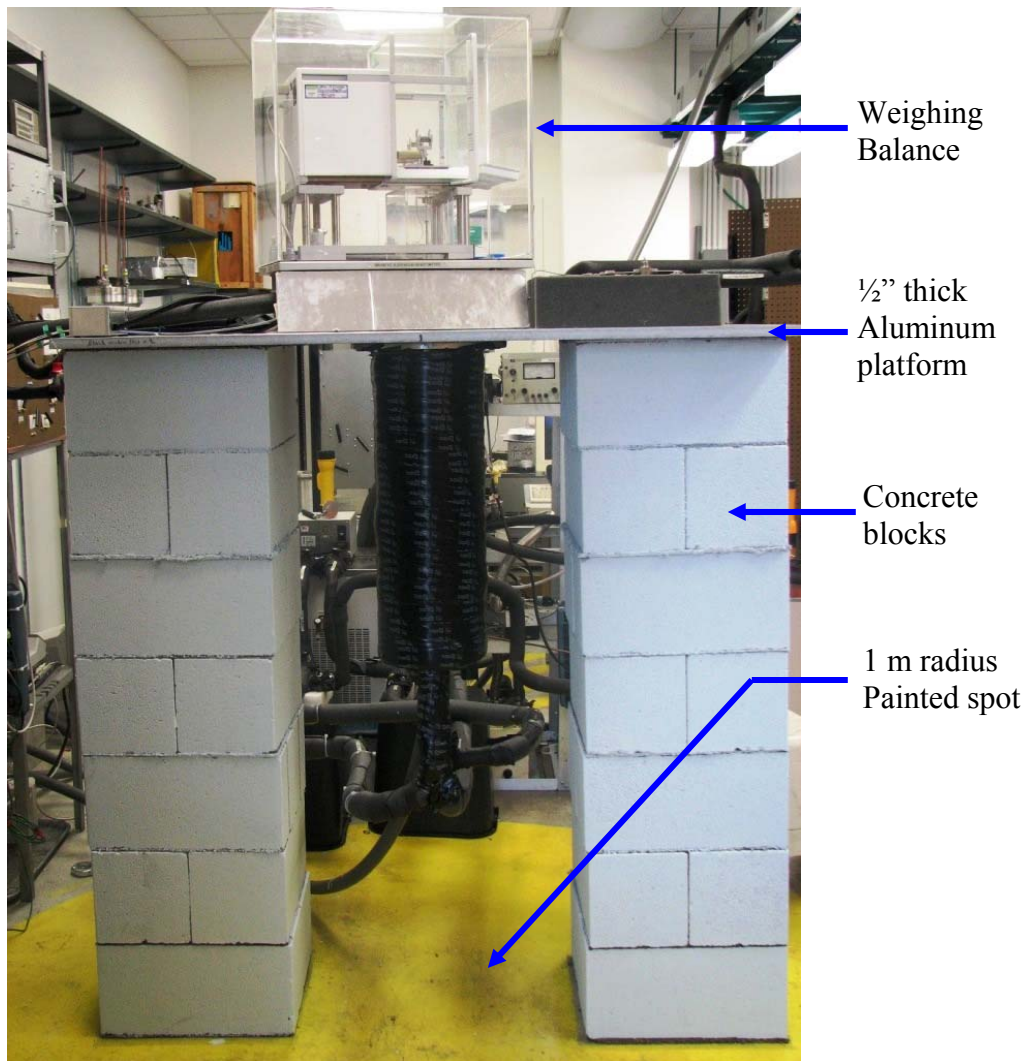


FIGURE 20. Concrete blocks, aluminum platform and weighing balance.

The balance base plate has a circular, bubble level indicator to check the horizontal alignment of the balance. However, we use a more accurate high precision level for horizontal alignment of balance base plate. The weighing balance frame attaches to the balance base plate with knurled latches. These knurled screws can be loosened to move the balance frame and center the EM suspension tube and retightened to prevent it from skewing during density measurements after initial centering.

During installation of high pressure the cell, the weighing balance and the suspension assembly, the EM suspension tube must be inserted from the bottom of the cooler and raised through the cooler until its threaded end is reaches the space in the acrylic glass box. After feeding the EM suspension tube, the high-pressure cell can be screwed into the cooler flange. The EM suspension shaft engages the suspension hook assembly, which is suspended freely from the hook located under the balance pan as mentioned above and shown in below figure 21.

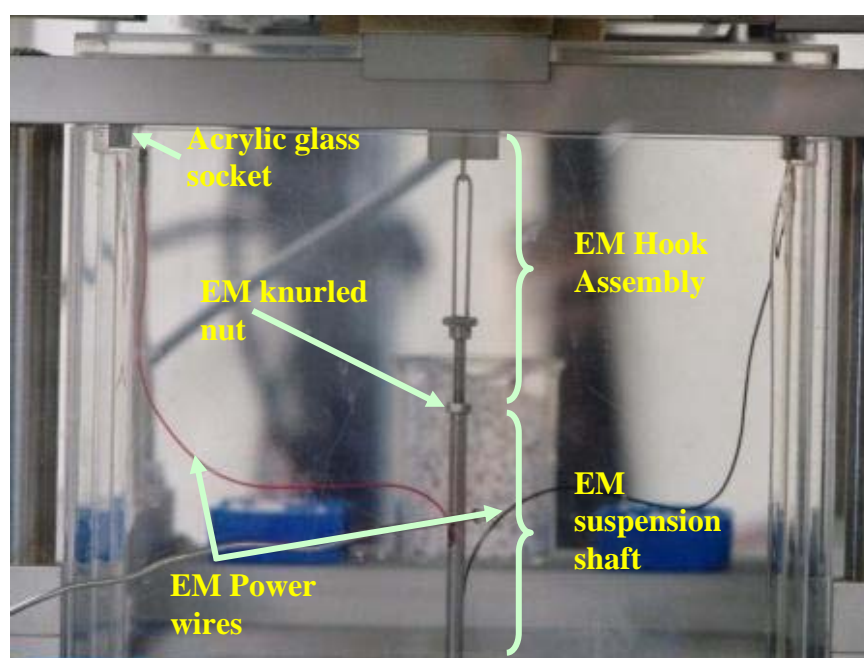


FIGURE 21. Electromagnet shaft and hook assembly.

Vertical alignment of the EM is one of the key adjustments before the density measurements. For stable balance readings, correct EM vertical height must be assured. For this reason, vertical alignment of the EM is checked by monitoring weighing balance readings at the beginning of each isotherm for experimented gas samples. The vertical height is adjusted by mechanically screwing the electromagnet connection hook assembly into the electromagnet suspension tube. A knurled nut is the locking

mechanism, which prevents change in the vertical height of the electromagnet from the electromagnet well bottom during measurements. It is very important to provide the same vertical height during vacuum measurements and pressure measurements. There are two acrylic glass plates with embedded brass electrical connection sockets in the acrylic space housing for electrical connections of the EM wires. By unplugging these wires, the EM can rotate freely for vertical alignment purposes.

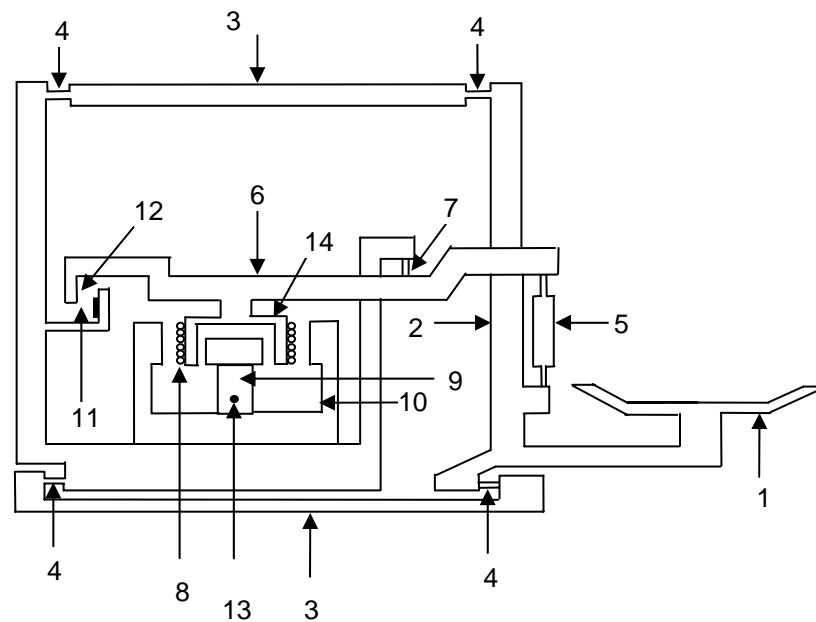
A wide gap exists between the bottom of the weighing balance and the balance base plate. The EM hangs from a hook located at the bottom of the weighing balance. The open space between the weighing balance bottom and the base plate is covered by transparent acrylic glass box in which a few inches of the EM suspension tube and connections for powering the electromagnet coil are exposed. This acrylic glass box is split into two pieces so that the electromagnet suspension tube can be removed from the hook and to access electrical connections.

The brand and model of weighing balance that is used in the MSD is METTLER Toledo AT 261. This balance has two measuring scales. The first range is between 0 and 62 g with 0.01 mg accuracy while the second range is between 0 and 200 g with 0.1 mg accuracy. For our high accuracy density measurements, we use the first range. The working principal of the weighing balance is based upon a magnetic force compensation technique. When weights are on the weighing pan, the coil support that acts as an electromagnet attached to the weighing pan rises. A linear-variable-differential transformer (LVDT) senses the displacement of the weighing pan from its null position. The LVDT sends the detected signal to a controller that manipulates the current in the electromagnet such that an active force,  $F$ , completely balances the weight on the pan,  $W$ , and the position sensor returns to the null position [44]. Because the current flowing is proportional to the compensation force generated and that force equals the weight of the load, the generated current is proportional to the load.

Another important feature of METTLER Balance that ensures stable weighing of the object apart from the position sensor LVDT and control system is a parallel-motion

guide system. This system absorbs the shock of lateral disturbing forces and assures that the true force is transmitted to the weighing section.

Several factors provide accurate readings through the balance. One of them is internal calibration and another is ambient conditions compensation. An ideal characteristic curve of the weighing balance comparing its display reading to the actual load is a straight line over the range between zero and maximum load. However, the characteristic curve may deviate over time because of external factors such as ambient temperature, pressure, humidity, altitude of the balance and horizontal leveling of the balance.



- |  |  |
|--|--|
| 1 Weighing Pan                           | 8 Compensation coil                            |
| 2 Hanger                                 | 9 Permanent magnet of electrodynamic converter |
| 3 Guide of the parallel-motion mechanism | 10 Magnetic circuit                            |
| 4 Flexible bearing                       | 11 Position sensor                             |
| 5 Link                                   | 12 Position indicator                          |
| 6 Lever to transmit weight force         | 13 Sensor for temperature compensation         |
| 7 Suspension of level                    | 14 Coil support                                |

FIGURE 22. Cross section of the weighing balance cell for METTLER balance [44].

Therefore, internal calibration of the balance is extremely important to bring the deviated characteristic curve to its original state. A linearity check of the balance is



performed using two 100 g reference calibration weights located within the balance. While this auto-calibration feature could be invoked by the balance itself when it senses drastic changes in conditions, it was not used during density measurements [22]. During internal calibration, ambient conditions are also accounted and compensated for using the 100 g calibration weights.

Temperature compensation is also necessary to maintain the strength of the permanent magnet located in the main weight measuring section. Temperature fluctuations influence the strength of the permanent magnet for magnetic force compensation. At higher temperatures, the magnetic field becomes weaker and causes higher currents leading to higher and incorrect balance display values. In order to compensate all these, a temperature sensor located in the balance senses the ambient temperature and the temperature of the permanent magnet. Later, these values are transmitted to the microprocessor where magnitude of compensation is calculated and applied. Figure 22 is a schematic cross section of the weighing cell of the METTLER AT balance.

#### **4.5 Temperature Control**

Initially, Patil [22] used an open circuit circulation system. In this mode, the high pressure cell was immersed directly in a circulating bath fluid. Heat transfer via conduction on the cell surface made the cell temperature fluctuate according to changes in the room conditions. Because of unstable temperature readings and liquid overflow of circulating fluid from open-top bath, a closed circuit system was introduced after the move of the apparatus to the new building. The closed circuit system includes two heat exchanger shields, one vacuum chamber, a constant temperature bath and a vacuum pump. Heating/cooling tubes and heating tapes are attached to the heat exchange shields. Temperature is measured by a platinum resistance thermometer (PRT).

##### **4.5.1 Heat Exchangers around the High Pressure Cell**

Figure 23 presents the heat exchanger shields and vacuum chamber. Two shields surround the cell with the outermost one being a vacuum shield. The clearance between

the cell body and the inner shield and between each successive shield varies between 0.75 and 1 inch. Clearance is small as possible for faster heating or cooling of the sample. Liquid is pumped at fixed temperature to the shield heating and cooling tubes from a constant temperature bath.

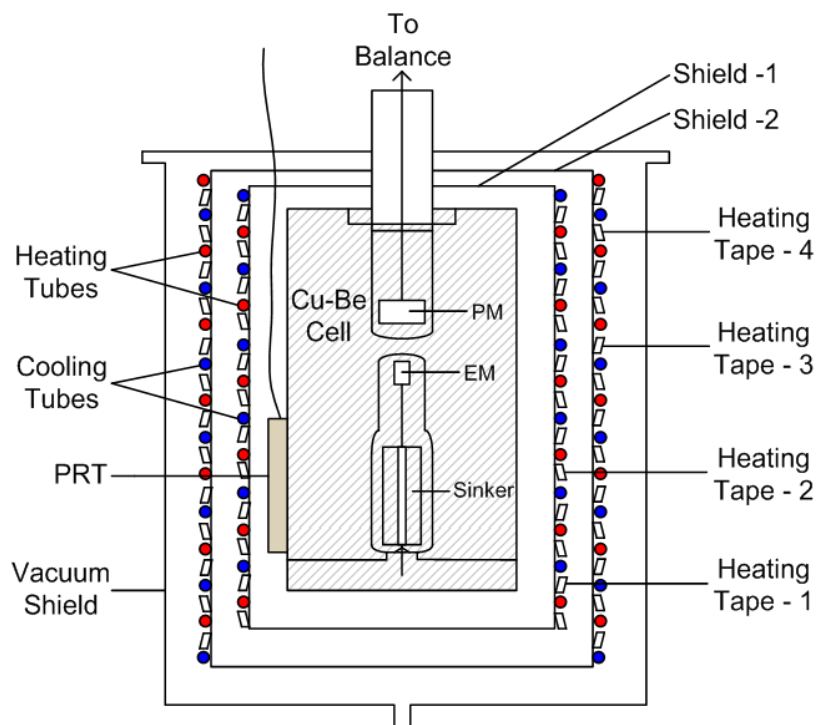


FIGURE 23. Heat exchanger shields and vacuum chamber schematics.

The vacuum pump connects to the vacuum shield, which is made of aluminum and vacuum is pulled during operations to provide heat transfer via radiation only. Preventing heat transfer via conduction and convection provides better temperature control for the high-pressure cell. Actual shield picture is given in figure 24 and high pressure cell picture is given in figure 25 after PRT and heater connections were made.



FIGURE 24. Heating/Cooling shield -2 with heating tape 1 and 2 connections made.



FIGURE 25. High pressure MDS cell with PRT and thermopile connections made.

When changing temperature of the cell, both shields are active. When approaching the temperature set point, we could keep only the inner shield active. When both shields are active, the response of the cell to temperature change is faster but stability may be sacrificed. With only one active shield, the reverse should hold true. During measurements, we keep both the shields active because we have not seen much of a difference in terms of stability.

Around the isothermal shields are 4 different sets of heating tapes (two for each shield) to fine-tune temperature. The wire comes from Clayborn Lab<sup>®</sup>. The heaters have 4.9  $\Omega$ /ft and can carry 52 W/ft. Heating tapes 1 and 2 have opposite polarity, so when current flows, the magnetic field created from each tape cancels. This cancellation is very important for stable sinker levitation. We use AC power supplies for the heating tapes. The heater action is controlled by LabView<sup>®</sup> using TTL (transistor-transistor logic).

A Platinum Resistance Thermometer (PRT) in the body of the high-pressure Cu-Be cell monitors and measures the cell temperature. We use silicon oxide paste between the Cu-Be block and the PRT body for physical contact. All the parts used on the isothermal shields and in the thermostat system are non-magnetic materials, mostly SS-316 or aluminum.

#### **4.5.2 Constant Temperature Bath**

We have a PolyScience<sup>®</sup> model 9512 constant temperature heating/cooling circulating bath. The working fluid is kept at constant temperature in the bath reservoir and then pumped to the isothermal shields. Different types of working fluids are used depending upon the desired working temperature range. Usually, 50% ethylene glycol and 50% water is the working fluid providing operation between 255 K and 350 K. For higher temperature operation, we use special silicon-based oil (Dow-Corning 550 DC-550 phenyl methyl siloxane oil). With DC-550, we can work between 373 and 473 K. Figure 26 is a picture of the constant temperature bath and its connections.



FIGURE 26. PolyScience ® constant temperature bath and its connections to MSD.

For temperatures lower than 255 K, we use liquid nitrogen. A 150 lt. liquid nitrogen dewar connects to same line as the constant temperature bath. We isolate the bath with globe valves and metering valves from liquid nitrogen flow. Liquid nitrogen flows through the isothermal shield tubes and then discharges as gas to a fume hood. Flow of liquid nitrogen is adjusted by a metering valve placed at the exit of the system.

A new cooling system will replace the liquid nitrogen cooling operation. This new system uses liquid nitrogen to cool liquid propane that then flows through the isothermal shield tubes.

#### **4.5.3 Liquid Propane Cooling System**

Liquid nitrogen is not a desirable cooling fluid for the apparatus because it provides unstable cooling caused by the large temperature difference between the nitrogen and the temperature of the apparatus. The main components of the cooling

system are: a heat exchanger, a gear pump, a cooling coil for the isothermal shield, and a liquid nitrogen container. In this system, liquid nitrogen cools liquid propane, which in turn cools the isothermal shield and the cell. Figure 27 presents a schematic diagram of this cooling system.

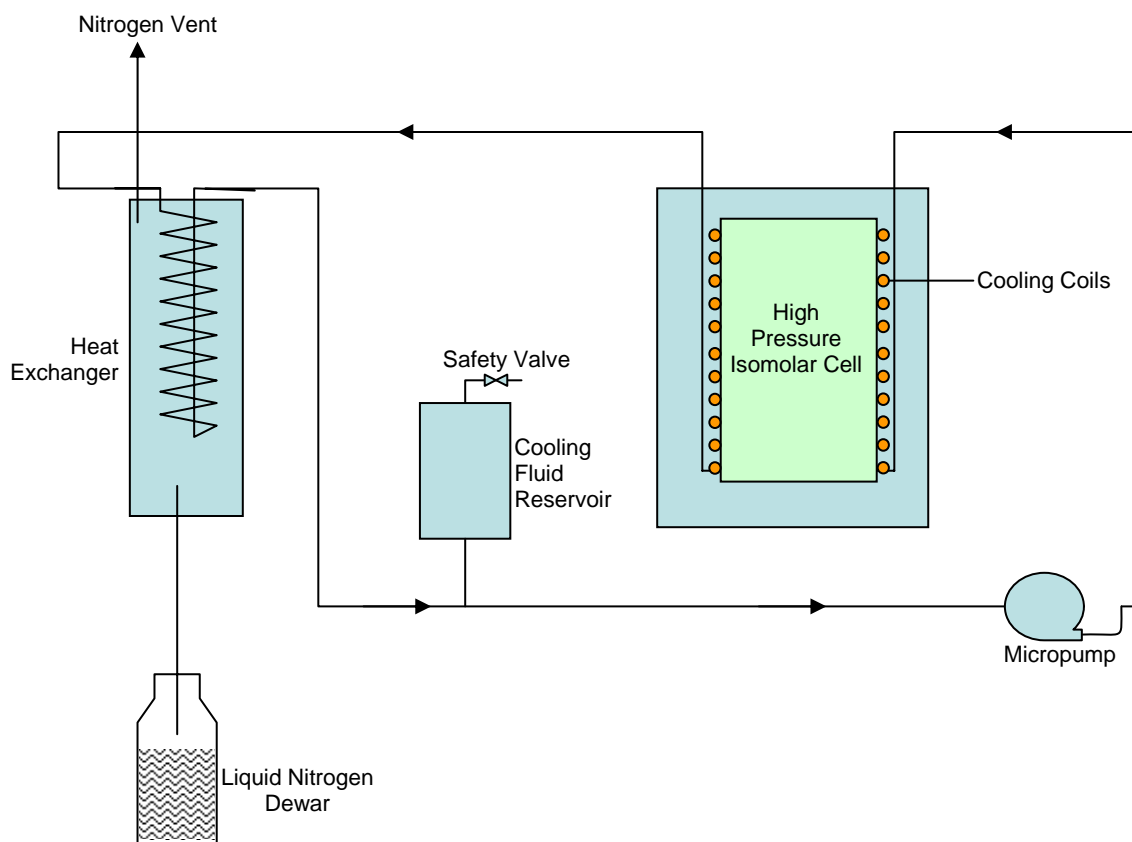


FIGURE 27. Schematic diagram of the propane cooling system.

We use propane as the cooling medium because of its low freezing point (85.5 K) and its low viscosity (less than 1 cp at 130 K). Also, propane has a relatively low vapor pressure (about 0.9 MPa at room temperature). The heat exchanger is a  $\frac{1}{4}$ " O.D. copper tube coil inside a shell made of a  $1\frac{1}{2}$ " OD pipe. The pipe is insulated with a 1" layer of a porous rubber material. The coil is 2 ft above the nitrogen vapor (77 K) feed port to avoid

freezing the propane. The operating temperature range of copper tubing is  $-253^{\circ}$  to  $204^{\circ}\text{C}$ .

Liquid propane flows inside the coil while nitrogen vapor flows through the shell. The coil has a heat exchange area of  $3600\text{ cm}^2$ . A closed, 150 l container stores the liquid nitrogen. The liquid nitrogen exerts a pressure of 0.2 MPa. This pressure is the driving force to force the nitrogen through the heat exchanger.

The liquid propane is pumped with a magnetic gear pump (Micropump<sup>®</sup>, model 180). This pump can handle a system pressure drop up to 0.276 MPa and a volumetric flowrate of  $20\text{ cm}^3/\text{min}$  with a maximum operating pressure of 4MPa. The temperature range specified by the manufacturer is 200 to 410 K. However, it has been observed that this pump can operate at 170 K without problem. The pump body and all internal pieces are stainless steel (SS-316); therefore it is suitable to operate the pump at the anticipated operating temperature range. This pump requires the outlet pressure to be higher than the inlet pressure to operate properly. So, the propane reservoir must be at the outlet of the pump and be at a slightly higher temperature than the rest of the system. This ensures that the outlet pressure of the pump is higher than its inlet pressure at all times. The pump is operated with a 0-24 V DC motor. The volumetric flow rate of the pump can be adjusted by varying the voltage applied to its motor. The cooling power of the system can be controlled by the volumetric flowrate of the gear pump. If liquid nitrogen condenses inside the shell, an external pneumatic valve controlled by computer controls the level. The computer reads the temperature of the shell side below the cooling coils, and, if there is sudden decrease in the temperature, a pneumatic valve opens to allow accumulated liquid nitrogen to evaporate and exit from the exchanger. The pressure in the liquid propane buffer tank is 250 psia. At ambient temperature (298 K) the pressure required to keep propane liquid is 130 psia. He gas is as blanketing medium on the propane in the buffer tank. For safety reasons, a relief valve on top of the liquid propane tank is set at 350 psi.

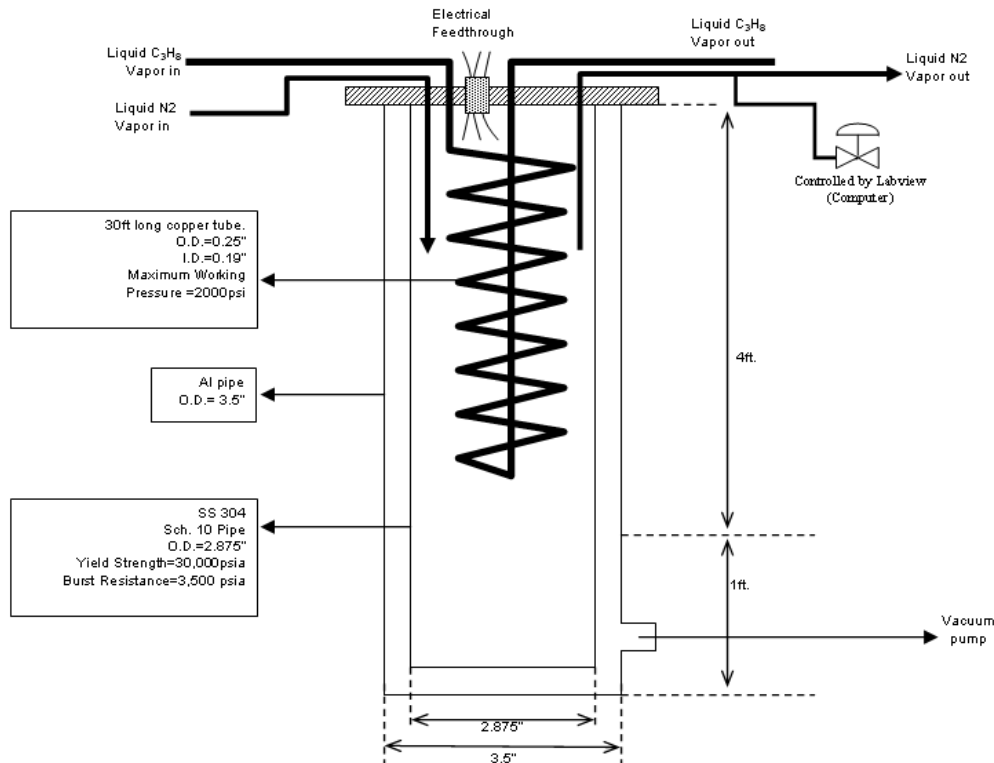


FIGURE 28. Schematic of heat exchanger of propane cooling system.

Figure 28 is a schematic of the propane heat exchanger and Figure 29 is a schematic of the propane tank. Figure 30 contains photos of the nitrogen/liquid propane heat exchanger and liquid propane tank.

#### 4.5.4 Temperature Measurement and Methodology

We use a Minco<sup>®</sup> four-lead, capsule PRT (model: S1059-2, serial number 204) with a range of 84.15 to 533.15 K for temperature measurements. The operating principle of resistance thermometers is to sense the change in resistance with changing temperature. For our 100  $\Omega$  PRT, the temperature sensitivity is 0.3925  $\Omega / ^\circ\text{C}$ . The PRT is calibrated using a triple point cell. In the current setup, we have checked the triple point of water temperature with our PRT. Details of the PRT calibrations appear in Appendix B.



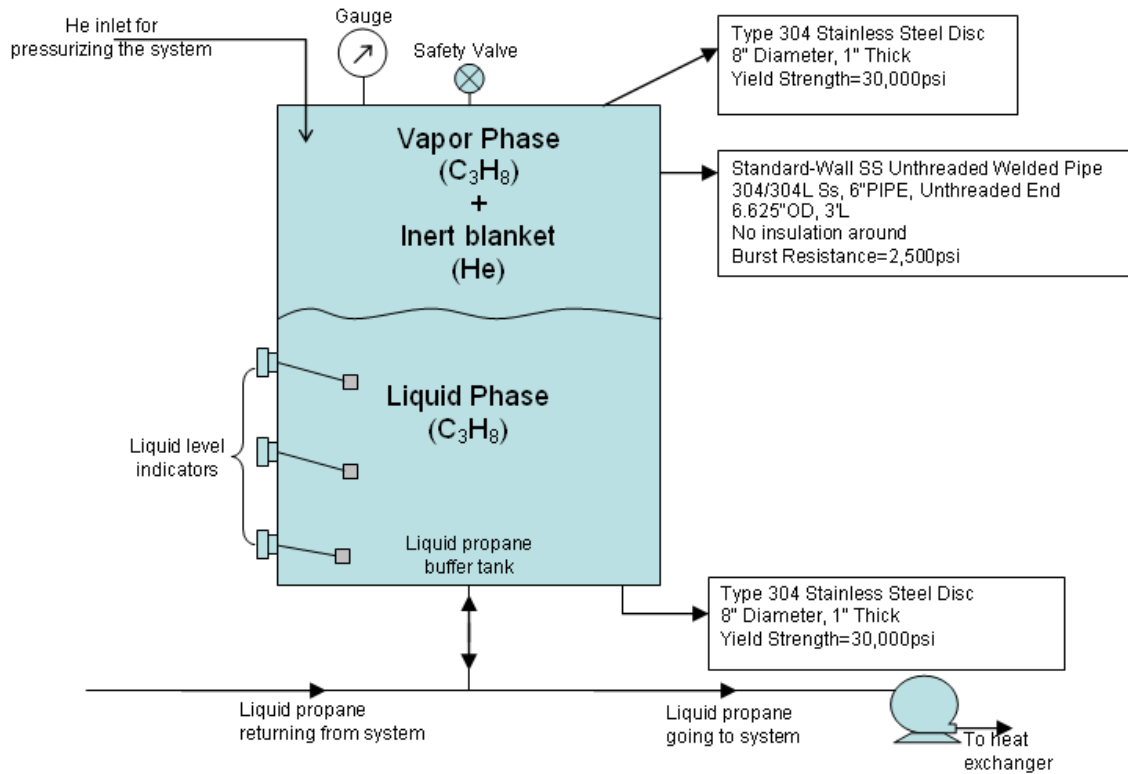


FIGURE 29. Liquid propane tank.



FIGURE 30. Liquid nitrogen/ liquid propane heat exchanger (a), liquid propane tank (b).

The PRT is inserted in a copper capsule and placed in a groove on the cylindrical surface of the MSD cell with a copper screw such that the capsule spans the height of the MSD cell. The top of the capsule is sealed with silicone caulk to prevent condensation on the PRT joints that might affect temperature measurements.

A custom-built constant current supply is used for temperature measurement. Figure 28 presents a schematic diagram of the constant current source. The current supply provides 0.14 mA to the PRT and to a four lead standard resistor (manufactured by Julie Research Laboratories, NY). To achieve high stability, the zener diode and the operational amplifier must be stable. The zener diode maintains a constant voltage of 6.95 V across its terminals. A zener diode is a special diode that can be forward biased or reverse biased. An external voltage of 15 V is applied, which is larger than the rated breakdown voltage of the reverse-biased zener diode. A reverse-biased Zener diode displays a controlled breakdown and lets the current flow to keep the voltage across the zener diode at the zener voltage [44].

An external, four wire JRL secondary-standard resistor is used in the temperature measuring system. The external resistor is compact, oil-filled, nominally equal to the ice point resistance of the PRT, and stable with time. The JRL resistor is calibrated, and its stability is 0.003% per year with 0.02% accuracy. The JRL resistor and PRT are connected in series. The DPDT reed relays have the ability to reverse the current to minimize the effects of thermal EMF using the computer program. The signal required to reverse the current comes from the National instrument PCI DAQ-card that uses TTL signal logic. Figure 31 illustrates the current reversing procedure. An external independent DPDT switch provides additional control to reverse the currents.

In order not to destroy the device and keep power dissipation below permitted levels, resistance  $R_1$  is as small as possible. By keeping  $R_1$  small, the current through the zener diode keeps the diode in reverse breakdown. The constant current produced by the constant current source can be varied by changing  $R_{ext}$ . Because of the large impedance between the input terminals, negligible current flows between the terminals.

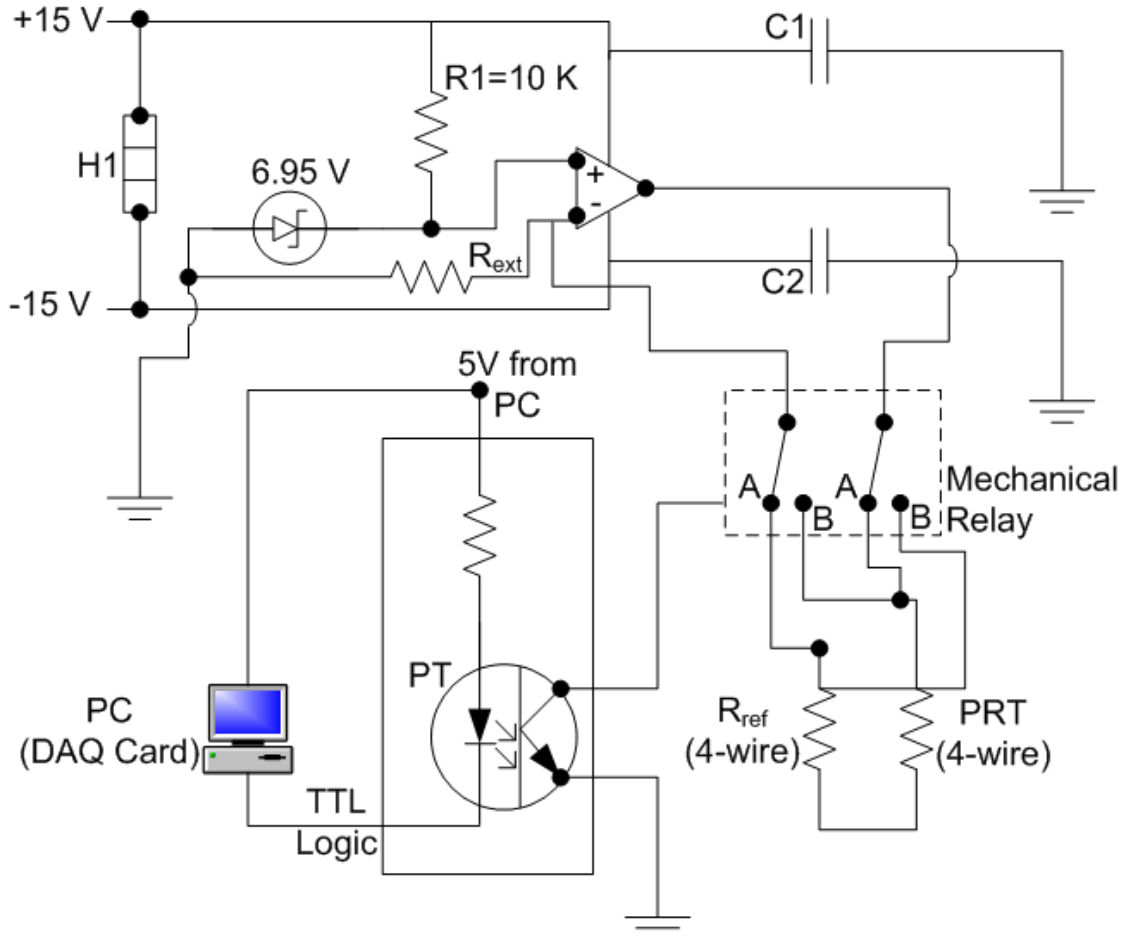


FIGURE 31. Constant current source.

Therefore, both terminals have essentially the same voltage. The output of the constant power supply than is  $I_o = 6.95/R_{ext}$ . We can vary the current from 0.1 to 0.4 mA in 12 stages. The main reason that the constant current source has stable working voltage and stable operation is the frictionless operation of the op-amps and the presence of heater (H1) that maintains the temperature of the zener diode.

Figure 32 is a circuit diagram for accurate measurement using a four-lead PRT and current reversing. A 6½ digit multimeter (DMM) with a scanning card (Keithley

Instruments® model: 2000-20, serial number 0832694) is used for measuring the voltage drop across the four-lead PRT and for to supply a stable 1 mA DC current through it.

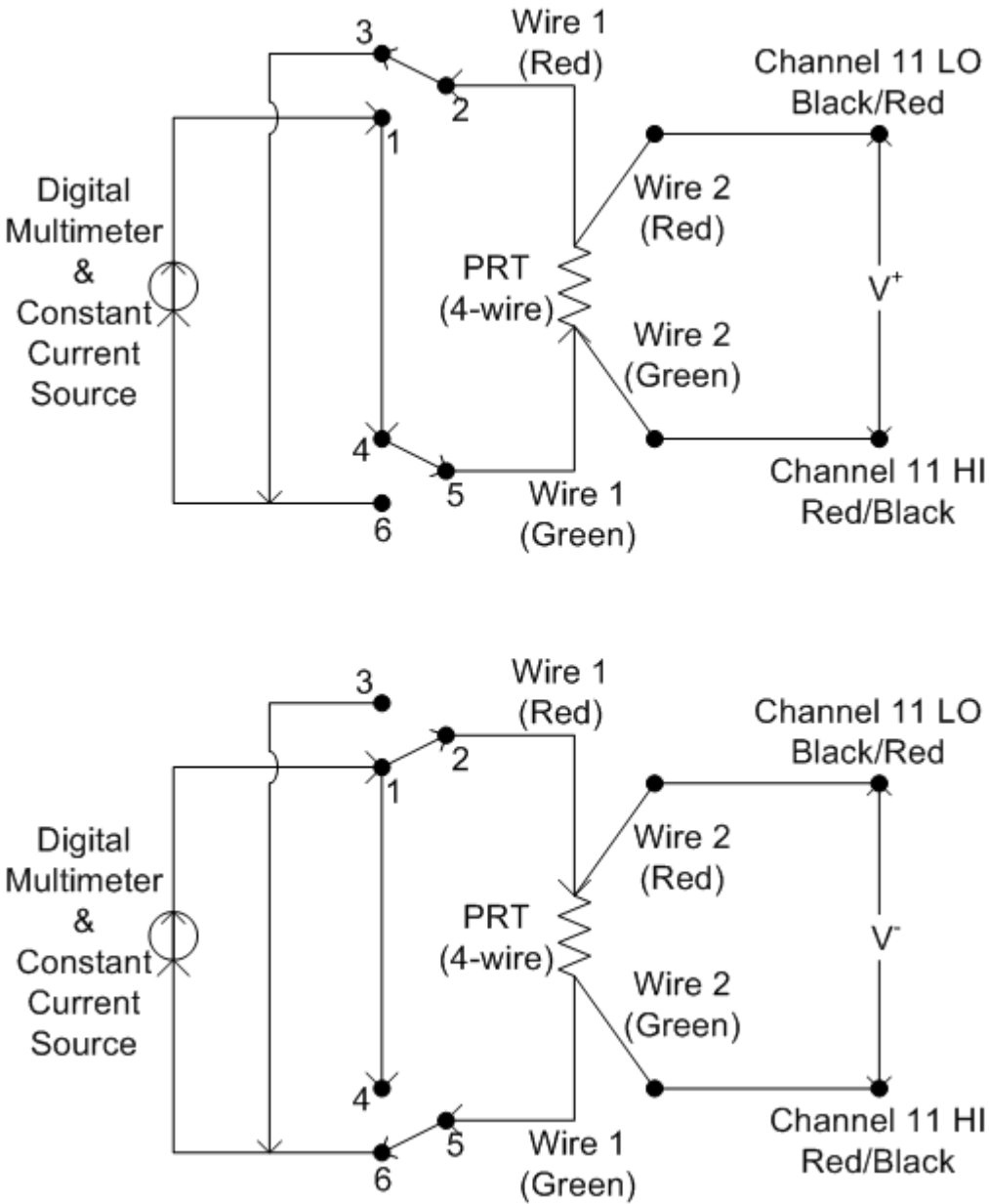


FIGURE 32. Constant current source current reversing procedure.

A constant current,  $I$ , passes through the PRT through one pair of its leads, 1 and 2, while the other pair, 3 and 4, measures the voltage drop,  $V_{PRT}$ . The resistance value is simply by the ratio of the measured voltage and the current value:

$$R_{PRT} = \frac{V_{PRT}}{I} \quad (18)$$

Because a voltage drop exists across the lead resistances  $L_1$  and  $L_2$  the measured voltage across the PRT is different from the actual voltage in a two lead PRT. However, actual voltages across a four-lead PRT are the same because the current through the voltage sensing leads with lead resistances  $L_3$  and  $L_4$  is negligible. Hence, four-lead resistance measurement is preferred for more accurate temperature measurements.

These voltages can be cancelled by measuring the voltage drop twice with currents of opposite polarity through the PRT. With the positive current applied, the measured voltage is:

$$V_{PRT}^+ = V_{EMF} + IR_{PRT} \quad (19)$$

With the direction of current through the PRT reversed, the measured voltage is:

$$V_{PRT}^- = V_{EMF} - IR_{PRT} \quad (20)$$

The average of the measured voltages with positive and negative currents then eliminates the thermoelectric EMF such that:

$$V_{PRT} = \frac{V_{PRT}^+ - V_{PRT}^-}{2} = IR_{PRT} \quad (21)$$

Equation (21) is the same as equation (18) for calculating resistance. The measured resistance of the PRT given by equation (19) or (21) is converted to temperature according to the International Temperature Scale of 1990 (ITS-90) described in [57] and the calibration constants for the PRT determined by Minco [58]. Possible noise that may occur during temperature measurements can be reduced by shielding and grounding the cables and digital filtering by the computer. Yet, it may be further reduced by using an analog to digital converter (ADC) with better resolution, for instance instead of using 6-bits; one could use an ADC with 24-bits.

A thermopile monitors the temperature gradient across the high pressure cell. A thermopile is a combination of five copper/constantan thermocouples ('T' type) in series. In our current setup, we measure the temperature difference as  $\Delta T = T_{\text{top}} - T_{\text{bottom}}$ . In principle, a voltage (the Seebeck effect) is generated between the measuring junction and the reference junction. This voltage difference is proportional to the temperature difference and is measured at assigned a channel in a Keithley digital multimeter. The temperature difference is required to minimize the temperature gradient across the cell by controlling the heater at the. For such an application, quality control of the thermopile output by signal conditioning or thermal electromotive force compensation is not necessary [59].

#### **4.5.5 Temperature Data Acquisition and Control**

All temperature measurement components and ancillary devices are controlled by Labview<sup>®</sup> programs installed on a PC. The computer uses and sends TTL logic signals through a PCI-DAQ card to control the on/off action of solid state relays (SSR) that control the heater. Measured voltage signals across the PRT are received by the DMM and digitalized. The digitalized PRT signal is converted to resistance and later converted to a corresponding temperature value based upon ITS-90. Figure 33 is an overview of the data acquisition and control system. Transistors used in the constant current source, the SSR and their operations are discussed in [44].

#### **4.5.6 DAQ Card Configuration and NI Connector Block Connections**

The National Instrument (NI) DAQ card (model # 6527) is installed in PC. Its pins are shorted with NI connector block placed next to the computer. DAQ card has 100 pins and the connector block has only 50 pins available. Therefore pins 51, 52, ... 67, 68, ... 71, 72, ... 75, 76, ... 79, 80, ... 99, 100 in the DAQ card are externally short-circuited with pins 01, 02, ... 17, 18, ... 21, 22, ... 25, 26, ... 29, 30, ... 49, 50 in the connector block by using a ribbon cable. Power supply and ground pins are 99 and 100 in DAQ card and 49 and 50 in connector block respectively.

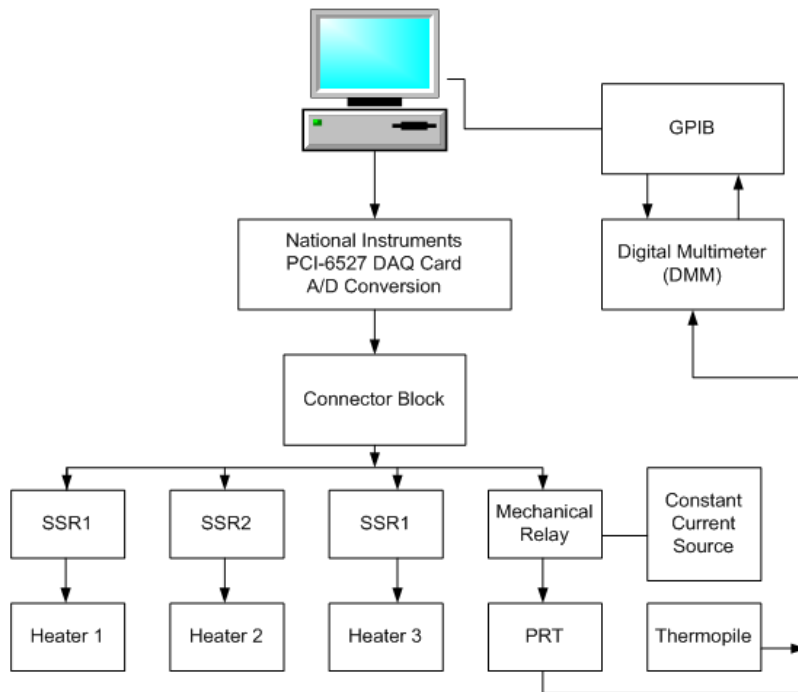


FIGURE 33. Overview of the data acquisition and control system.

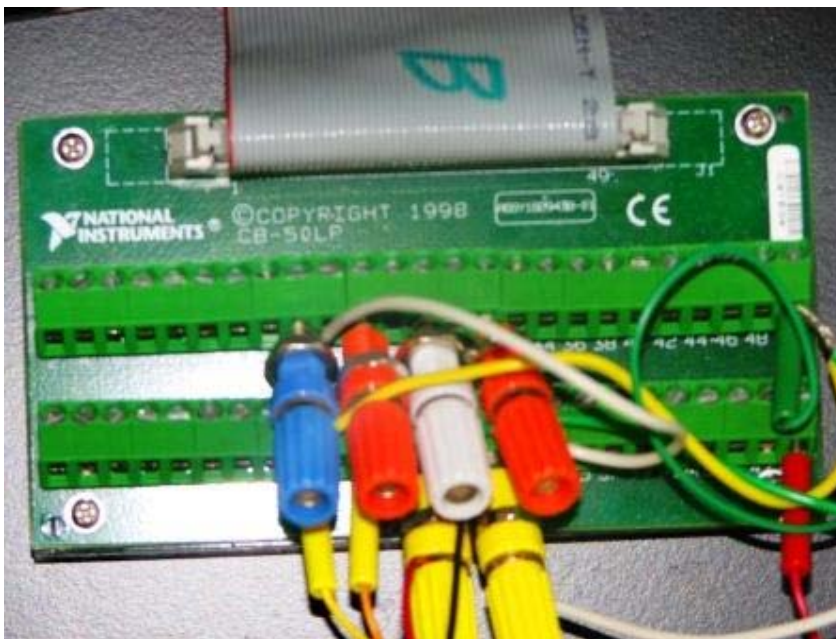


FIGURE 34. DAQ card connector block.

This DAQ card can handle only digital input and digital output. Figure 34 is a picture of the connector block that utilizes the DAQ card pins.

Pins 17 and 18 in the connector block drive SSR1 for heater 1. Similarly, pins 21 and 22 drive SSR2 for heater 2. Lastly, pins 29 and 30 drive SSR3 for heater 3. Heaters 1 and 2 are on the smaller isothermal shield and heater 3 is on the high-pressure measuring cell top. In the current setup, connections for heaters 4 and heater 5 are on the outer isothermal shield, and the computer program must be modified. Pins 25 and 26 are connected to the constant power supply box for current reversal in PRT resistance measurement.

Use of multiple ground points results in generation of ground loops that can result in current flow through the circuit common and cable shields. This may cause loss of signal and noise. In order to avoid such problem, digital grounds and grounds of the SSR are connected to the DAQ ground reference pin.

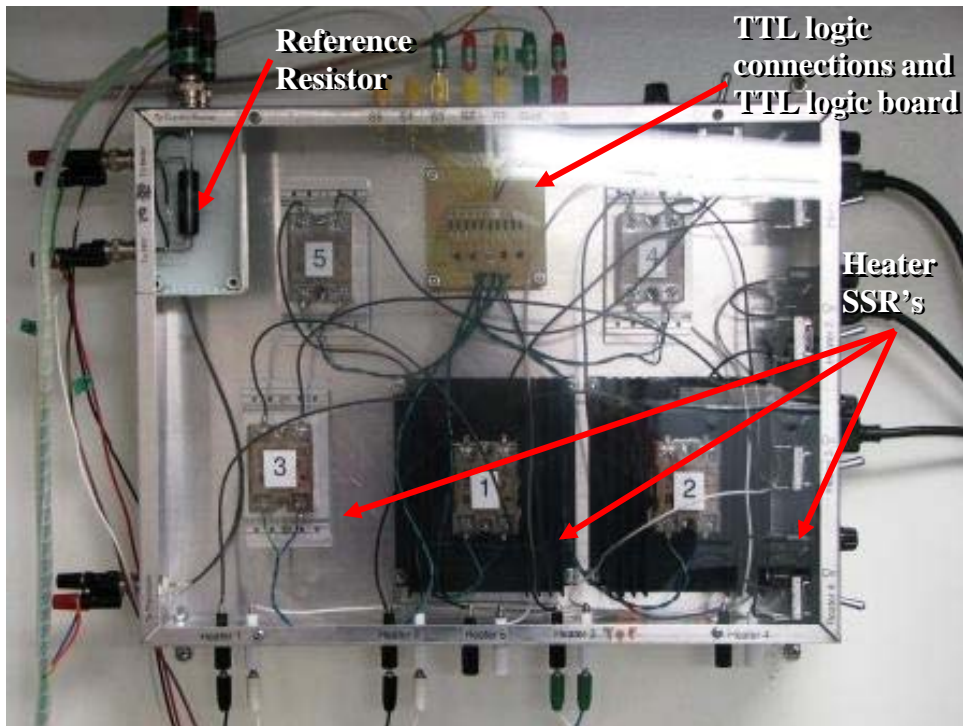


FIGURE 35. Picture of temperature control system box.



Finally, figure 35 is a picture of the temperature control box including the reference resistor, heater SSR and thermopile connections. The basic circuitry and connection diagram of temperature control system box is figure 36.

#### 4.6 Pressure Transducers

For pressure measurements we use oil-free, absolute pressure measuring and resonating crystal pressure transducers (Paroscientific). NIST traceable calibrations are applied to the pressure transducers. Depending upon the pressure range of the measurements, two different pressure transducers are used for pressure measurements. For pressures up to 206.9 MPa (30,000 psi), we use pressure transducer PT30K (model 430K-101, serial number 80872). For low pressures (pressures up to 41.4 MPa, 6,000 psi) we use pressure transducer PT6K (model 46K-101, serial number 84267) because it has better accuracy than PT30K at low pressures.

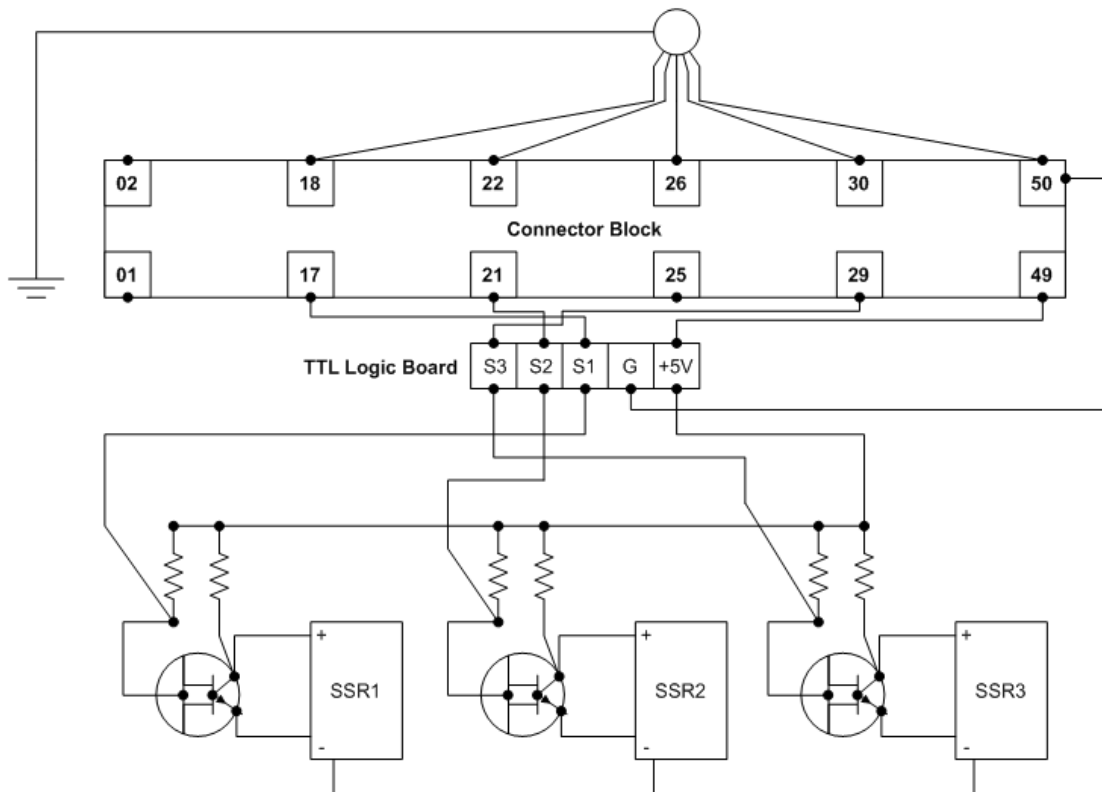


FIGURE 36. Circuitry and connection diagram of temperature control system box.

Instead of expressing the percentage of full scale, the accuracy of pressure measurement is better from a transducer whose accuracy is expressed as a percentage of the pressure reading [22]. The manufacturer's specified accuracy is  $\pm 0.01\%$  (full scale) for PT6K and  $\pm 0.02\%$  (full scale) for PT30K. Therefore, we prefer to use PT6K for pressures lower than 40 MPa and PT30K for pressures between 40 MPa up to 200 MPa.

A polarized quartz crystal is the resonating material in the transducers. As pressure is applied, the quartz crystal self-aligning molecules generate voltage that is directly proportional to the frequency of oscillation. This voltage also varies with pressure-induced stress and with temperature. PT6K and PT30K have internal temperature signals that thermally compensate the pressure calculated from the frequency of oscillation. Therefore, pressure can be measured accurately over a wide range of temperatures. The operating temperatures are: for PT6K between 273.15 and 398.15 K and for PT30K between 273.15 and 323.15 K. Both transducers can be used 20% above the recommended higher pressure limit.

Both transducers are kept above ambient temperature. PT30K is at 52 °C and PT6K is at 30 °C during the sample measurements. Each transducer is in a cylindrical hole slightly larger than the outer diameter of the transducer bored into a solid aluminum cylinder with 4 inch diameter and 9 inch length [22]. The aluminum block thermostating system includes a three-lead PRT, an auto-tune PID temperature controller, a solid state relay (SSR) switch, a cartridge heater (all supplied by Omega Engineering) and a variable AC power supply shown in figure 37.

The PRT used in the thermostat is a three lead, ceramic encapsulated, 100  $\Omega$  PRT (Omega model: RTD-2-1PT100KN2528-108-T). The PRT has a temperature coefficient of resistance of 0.00385  $\Omega/\Omega/^\circ\text{C}$  and is accurate within  $\pm 0.3$  °C at 0 °C and  $\pm 0.8$  °C at 100 °C. The PID temperature controller (Omega model: CNi3244) keeps the temperature at the desired value. The controller can control temperature with an accuracy of  $\pm 0.5$  °C. The aluminum block is insulated with glass-wool and a polystyrene/styrofoam box and isolated from ambient conditions. Details of the transducer calibrations appear in Appendix C.

#### 4.7 Magnetic Suspension Densimeter Operations

The manual for a single sinker MSD comes from Rubotherm [56]. A detailed description of the MSD appears in this operating manual. The manual also contains the operating procedure and information on control boxes and the weight changing device. The MSD employs a differential application of Archimedes' principal.

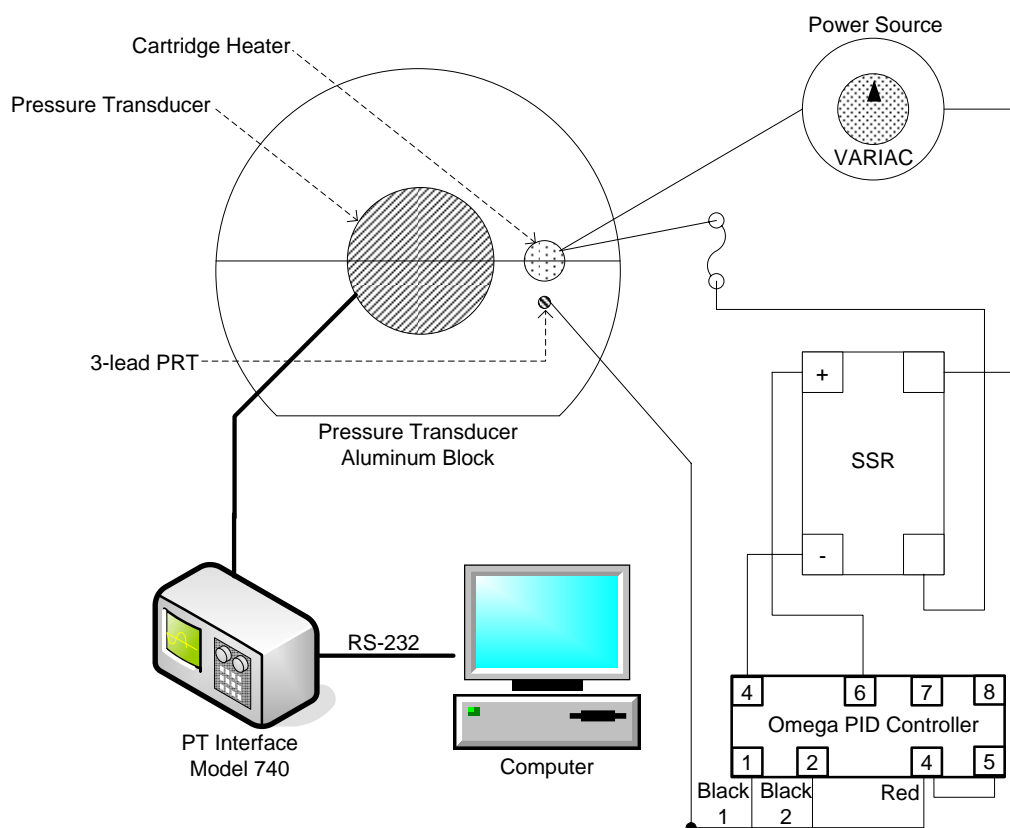


FIGURE 37. Schematic of pressure transducer thermo-stating system.

The weight of the titanium sinker is monitored under vacuum and under pressure, and, as described in equation 6, density is determined by dividing the difference of both readings. The sinker resides in a high-pressure copper-beryllium (Cu-Be) measuring cell. The maximum operating pressure for the cell is 200 MPa; however, the manufacturer

tested the cell up to 300 MPa with water. The cell has a state-of-the-art magnetic levitation system supported by control boxes. This coupling system allows contact-less transmission of force from the pressurized measuring cell to the balance at ambient conditions. Figure 38 provides a drawing of the MSD cell.

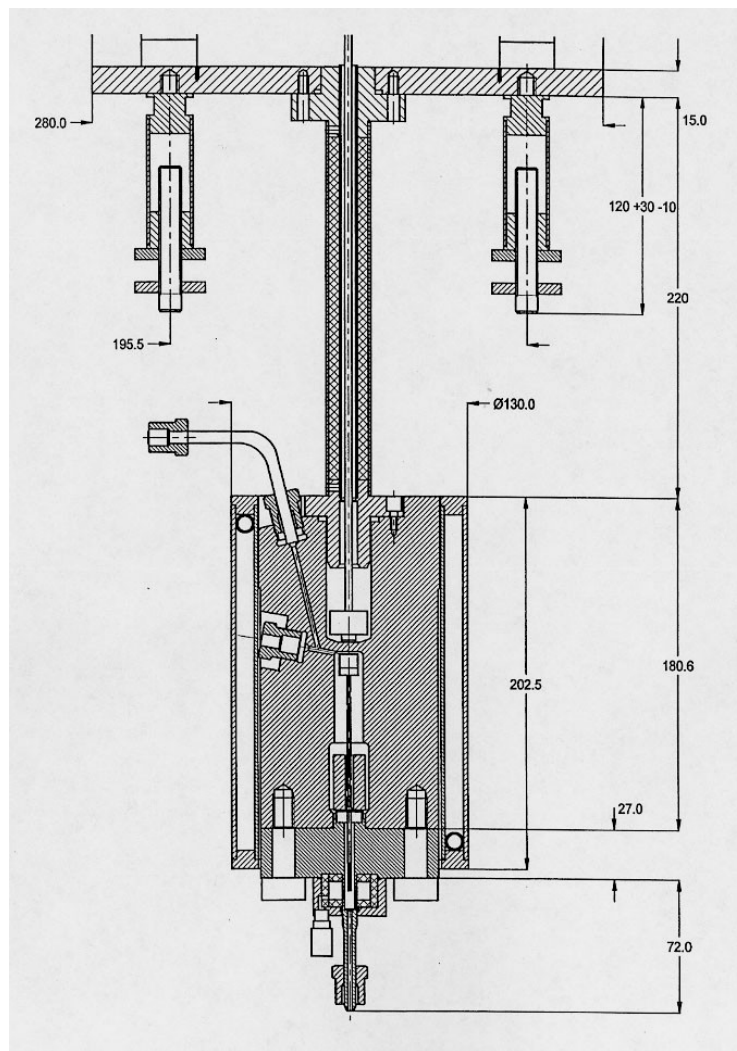


FIGURE 38. Cross-section of MSD high pressure measuring cell (units in mm).

Magnetic coupling occurs in the heart of the MSD. The EM has soft iron core and the PM is samarium cobalt ( $\text{SmCo}_5$ ). The Electromagnet is attached to the balance from a

hook located under the balance weighing pan. A thin wall separates the pressure environment and ambient conditions; in other words, between EM and PM, there is a thin separating wall. When desired, either manually or automatically, the EM is energized and a magnetic coupling develops between PM and EM. Two positions exist under magnetic coupling: ZP (zero point) and MP (measuring point). In ZP position, the PM is raised only a few mm such that it does not couple with the sinker; and the EM and all the magnetic levitation ancillary equipment is tared to zero. In the MP position the PM is raised such that the sinker is coupled. The sinker is raised and its weight is sensed by the digital balance. Depending upon gas density, the distance between the permanent magnet and the top of the inner part of the pressure-cell is about 1 to 3 mm in the measuring position and about 6 mm in the taring position [15, 24]. ZP and MP weighing positions appear in Figure 39.

Three effects cannot be cancelled in single sinker magnetic suspension densimeters. The interaction between the high-pressure cell housing and the sinker affects the force transmitted through the magnetic coupling and is a major problem for the apparatus. Although Cu-Be is nonmagnetic, impurities exist in the material that cause an offset. This means that the sinker mass is not be the same if measured directly at the balance and measured through the coupling. Because the position of the PM changes in the cell housing and approaches the cell wall in MP position, this effect persists. According to Kuramoto et. al. this handicap has an effect upon density on the order of  $10^{-6}$  [24]. Wagner et al. have suggested a multiplying factor of  $1 \pm 20 \times 10^{-6}$  to the numerator in equation 6 [15].

Secondly, the magnetic susceptibility of the fluid being measured in the cell creates an extra magnetic field and interaction between the molecules and PM. Both paramagnetic and diamagnetic fluids cause this fluid effect (described in detail in section 3.4.2). Also in the same section, an empirical correlation is proposed for the correction of the fluid specific effect, which is slightly different from the empirical correlation proposed by Klimeck et. al. [39].

Lastly, gas adsorption on the sinker surface has a negative effect on actual

pressure and a positive effect on buoyancy. However, this is significant only at low densities and in the vicinity of pure component critical points [32]. The first and third drawbacks do not exist in two sinker densimeters. However, the fluid specific effect exists in two-sinker MSD. On the other hand, despite the drawbacks of single sinker MSD, they can be corrected using simple empirical correlations. Nevertheless, a two-sinker MSD has pressure limitations and single sinker devices can reach high pressures.

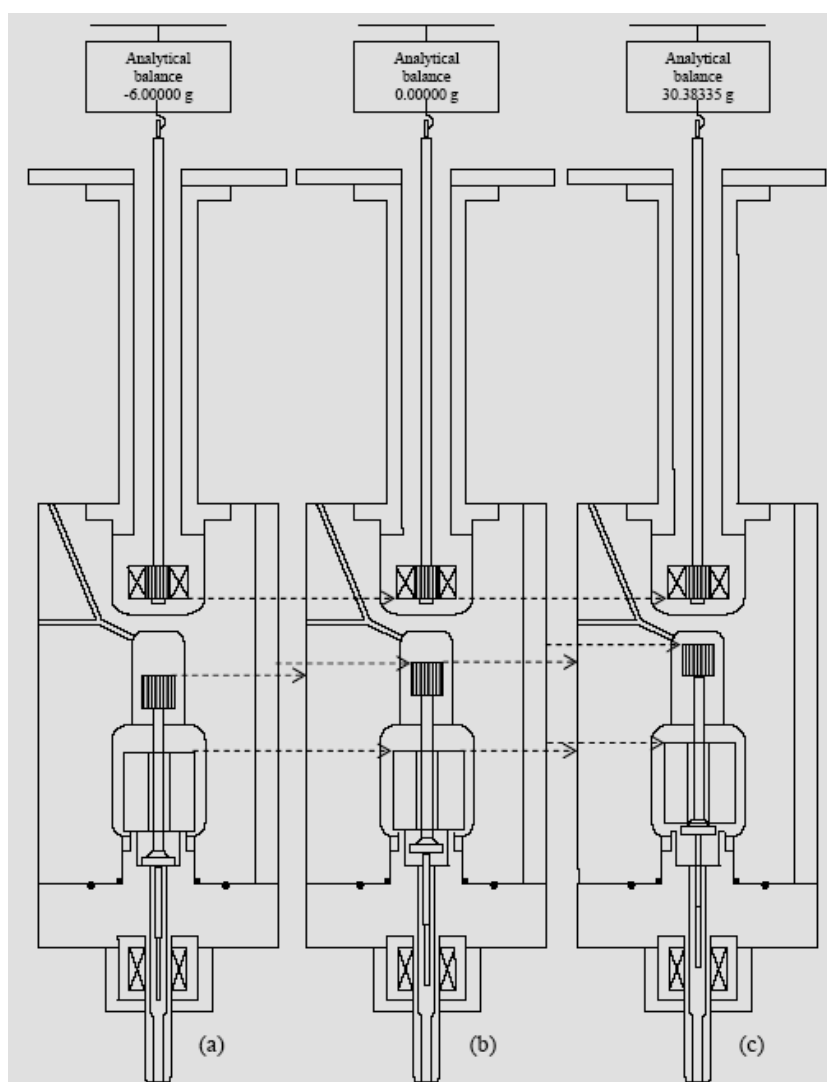


FIGURE 39. Operation of MSD (a) Magnetic levitation off; (b) magnetic levitation is set to ZP position; (c) magnetic levitation is set to MP position.

The PM absolute position is detected by the position sensor and then is levitated and kept in fixed position by a fast loop PID controller. The position sensor box appears in figure 40. Controlled upward and downward movement of the PM results from a superimposed set-point controller and an additional control system kept commercially confidential [32, 39].

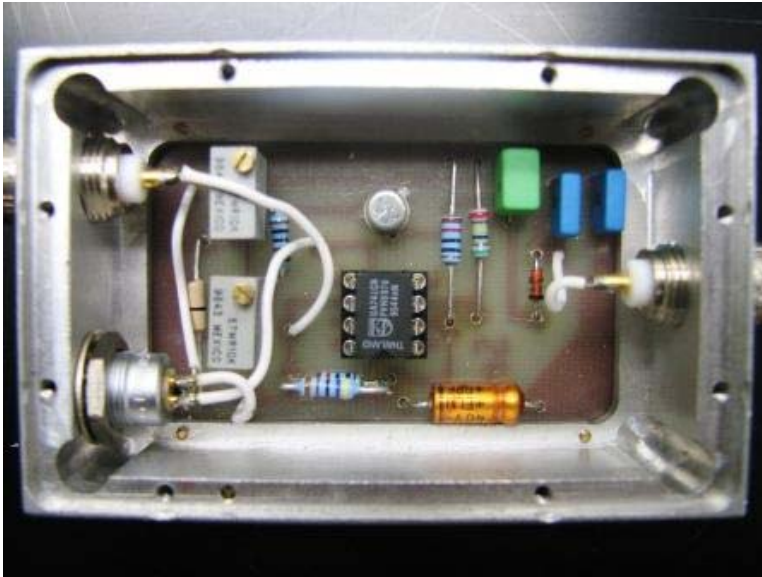


FIGURE 40. Position sensor box.

Because the PM coupling with EM is a function of cell temperature, proportional gain in the set point control system must be modified by variable resistors. Two different resistors can be replaced in the set point control system main board. An external variable resistor box is installed outside of the main control box and depending on the temperature range, resistors are changed manually to provide stable levitation of the PM and the sinker. By experience, resistor values appearing in table 2 provide stable coupling.

TABLE 2

Variable resistor values determined for different temperature ranges.

	Temperature Range [K]	Resistor #1 [k $\Omega$ ]	Resistor #2 [k $\Omega$ ]
Range 1	250-280	20	20
Range 2	280-350	30	30
Range 3	350-450	33	47

Details on magnetic levitation of the sinker and control action appear in [22, 44].

#### 4.7.1 Weight Changing Device

Because the weighing balance deviates slightly from its ideal operation curve, we must compensate for non-linearity of the weighing balance by introducing an external weight compensation system. Figure 38 contains a typical operating curve for the weighing balance.

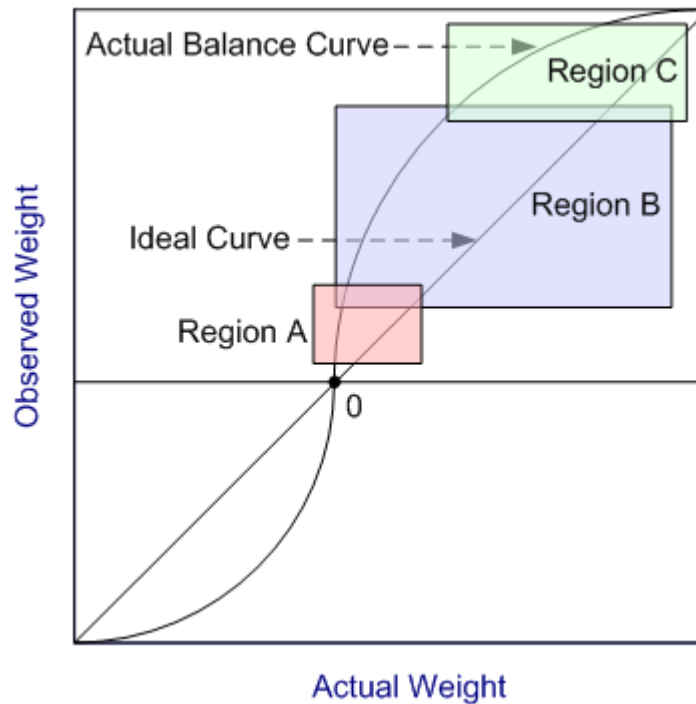


FIGURE 41. Illustration of weighing balance actual curve vs. ideal weighing curve.



The solution introduced by the weight changing device is to measure the weight of the sinker in MP position as close as possible to a balance display reading of zero. Weight changing consists of two different weights: one titanium (Ti) and the other tantalum (Ta).

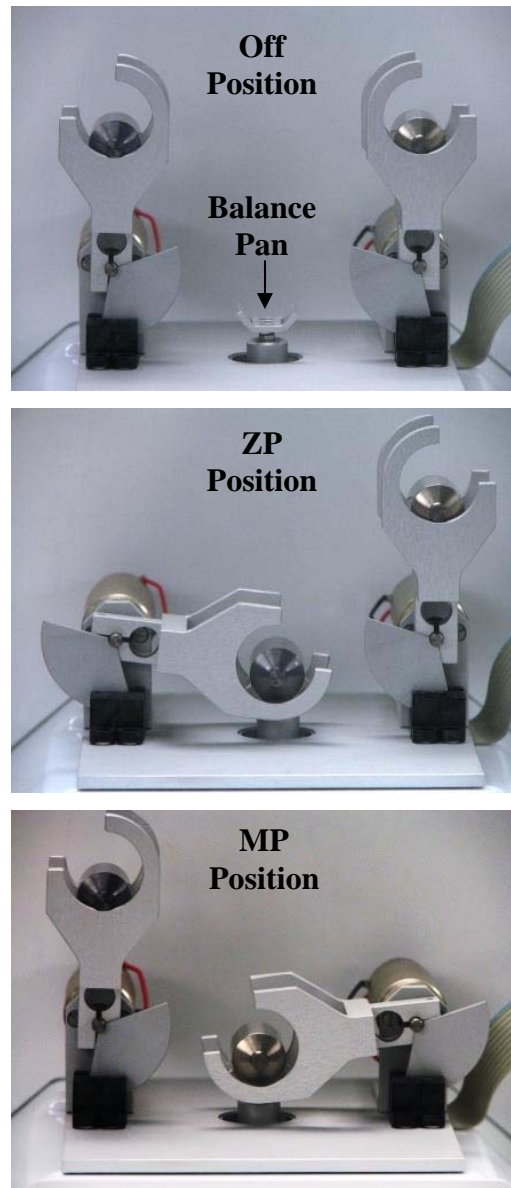


FIGURE 42. Weight changing device (Ta weight on the left, Ti weight on the right).

The Ti weight is approximately 10 g and the Ta weight is about 40 g. The 16.7 g/cm<sup>3</sup> density of tantalum is approximately four times the 4.5 g/cm<sup>3</sup> density of titanium. Either of these weights is lowered onto the balance mini pan as shown in figure 42 depending upon the measuring position. Ti sinker weighs approximately 30 g. This allows the balance reading of the sum of the titanium weight and the titanium sinker in the MP position as well as the balance reading of the tantalum weight in the ZP position to be close to zero. The balance calibration and operating curve appear in Appendix D.

#### **4.7.2 MSD Alignment**

For stable sinker weighing, several precautions and adjustments must be made. Alignment of the EM tube is the most important adjustment. The two types of alignment are: vertical and horizontal.

##### **4.7.2.1 Vertical Alignment**

Depending upon the vertical height of the EM from the EM well bottom, magnetic coupling can be lost. If the EM is too far away from the EM well bottom, the levitation system loses coupling a few seconds after the PM engages the EM. In order to prevent this problem, careful vertical height adjustment must be performed before the start of each isotherm. Once stable levitation is achieved without loss of magnetic levitation, the vertical position of the EM should be kept the same during the entire isotherm.

The EM vertical height adjusting procedure is not complicated, however extra attention must be given because the hook assembly and the electromagnet itself have very delicate natures. After disconnecting all the wires and cables attached to the EM the EM is rotated counter-clock wise till it stops turning and reaches the bottom of the EM well by using the knurled section of the EM tube.

Then, the EM tube is turned clockwise ½ turn. The EM is kept at this position throughout the measurements for almost all points. If stable coupling cannot be achieved, several different heights of the EM can be tried until stable coupling and levitation is achieved.

#### **4.7.2.2 Horizontal Alignment**

Although a round bubble level indicator is attached to the surface of the weighing balance base plate, a more precise level is used to perform horizontal alignment of the MSD. Horizontal alignment includes two adjustments; first centering the EM tube that passes through the cooler, second leveling the weighing balance base plate. Centering the EM tube is done by hand and the EM tube is checked and centered visually.

We use a high accuracy level indicator accurate to 1 mm in 100 m. There are two different positions that we place the level to check the horizontal alignment. First, we place it in front of the acrylic glass window in x direction to check level in x axis. Later, we take the level and place it in the y direction at the back of the acrylic glass window and check the level on the y axis. This is an iterative procedure and each time one of the four adjustment nuts located on the balance base plate legs is adjusted. It may take 10 to 30 minutes to finish the whole alignment process. After finding the correct position, the adjustment nuts are locked. Because the balance base plate is sensitive to motion, touching the aluminum base plate should be avoided after the horizontal alignment.

#### **4.7.3 Sinker Volume Calibration**

The sinker volume has been determined using the hydrostatic computer technique described by Bowman et. al. [60, 61]. This method differs from the traditional hydrostatic technique in that the known density is that of a solid object rather than a reference fluid, such as water. The standard and unknown objects are suspended in a fluid, but the fluid serves only transfer density knowledge of the standard to the unknown. The density of the fluid itself need not be known. It only needs to be constant for the time necessary to complete the measurement.

Several factors affect total uncertainty of the density measurement. One factor that adds to total uncertainty of the density measurements other than temperature measurements, pressure measurements and composition of the mixture being measured is uncertainty in sinker volume. Our latest sinker calibration comes from the National Institute of Standards and Technology in Boulder. They use the hydrostatic weighing

method with single-crystal silicon as the reference material. The reference material density determination is NIST traceable and the relative uncertainty in volume achieved by this method for a steel sphere is as low as  $10^{-11} \text{ cm}^3$ . Although our sinker geometry is cylindrical, a sphere is used because excellent sphericities are available and it is less susceptible of damage and distortion.

Mostly for sinker volume calibration, water is preferred [24]. However, NIST uses fluoroether because its density increases the buoyancy force acting on the submerged sinker and makes volume calibration more accurate [62]. Additionally, fluoroether has 78 % less surface tension than water, which reduces the force acting on the suspension wire that holds the sinker during calibration. Moreover, less surface tension prevents contamination of the liquid on the surface. Consequently, the buoyancy forces acting on the reference crystal and titanium sinker are measured with less spread than with water. As a result of calibration, our sinker is  $6.74104 \pm 0.00013 \text{ cm}^3$  ( $k=2$ ) meaning the total uncertainty in sinker volume is about 19 ppm.

#### **4.8 LabView Data Acquisition Programs**

There are five different data acquisition and control programs that we developed for the operation of our MSD. These programs are developed in LabView environment. Labview is a graphical development environment with predefined built-in modules that can be used for most data acquisition systems, instrument control, measurement analysis, and data presentation for engineering applications. LabView enables easy operation for the users through its excellent remote panel control feature. With this standard feature, the user can quickly manipulate system variables and take required actions through many communication devices such as handheld devices, pda's, cell phones and web browsers. Remote control of the running programs is possible by obtaining the programs through an internet server. This feature enables the user to communicate and run instruments and manipulate systems parameters remotely.

The programs developed in this work control temperature, monitor pressure transducers and automatic and manual MSD operations. Programs monitor 6KPT and 30KPT have the same infrastructure.

The program that we use for temperature control was initially developed by Zhou [21]. The program collects data every 12 seconds. Of the 12 seconds, it takes 8 seconds for data acquisition and 4 seconds for heater operations. However, the 8 seconds of data acquisition time can be reduced by manipulating the digital multimeter parameters: power line cycles (NPLC). The default NLPC number is 10 in the MSA main 1.vi temperature measurement program. By changing this value from 10 to 5, the total time required for data acquisition for each temperature point cycle is reduced from 8 to 4 seconds. The temperature program displays the temperature gradient across the high pressure measuring cell, real time temperature, running average temperature and standard deviation of the temperature throughout the measurement time. Forty readings are taken for average and standard deviation calculations. The typical screen shot for the temperature program appears in Appendix E. As explained previously, the temperature program measures the voltage across the PRT and reference resistor in forward and reverse directions of current. The calculated resistance is converted to temperature using ITS-90. Details of the program is explained by Ejaz in his doctorate dissertation [44].

For pressure transducers, communication with the PT interface is provided by LabView programs. The programs we use for this purpose is Pressure Transducer\_6k.vi and Pressure Transducer\_30k.vi. We can monitor the PT temperature and physical pressure in real time with these programs. Also, we can collect temperature frequency and pressure frequency for resonating quartz crystals. These frequency values can be used to check the calibration values of the PT's. The typical screen shot for the pressure program appears in Appendix E as well.

For MSD operations, we use the MSAautobalance\_final\_1.vi program. This program helps us to communicate with the digital weighing balance, external weight changing device and magnetic coupling control box. The balance is configured with the serial port settings: bits per second - 9600, data bit - 7, parity - even, stop bits - 1, flow control - none, hand shake – hardware, end of line – CR. For the weight changing device the command sent through the LPT port in ZP position to lower the Ta weight is 100101. For the MP position, to raise Ta weight and to lower Ti weight, the command is

10100110. Before each measurement, forerun cycles are enforced by the program to achieve stable levitation during measurements. Following the forerun cycles, the MSD goes to ZP position and tares the balance. In this part of the program, sub vi 'readZP1.vi' is active. This sub vi enables direct monitoring of the balance readings on the screen. After ZP position, the MSD goes to MP position and in this part of the program 'readMP1.vi' is active. Following MP, the MSD goes to 'end ZP' position and at the end of the 'end ZP' position the first measuring cycle is complete. The reason we measure ZP in the beginning and at the end of each measuring cycle is to monitor the drift in balance weighings. The number of cycles, forerun ZP and MP time, number of zero points and measurement points in each cycle, ZP and MP stability time, etc. can be controlled from the front panel. Moreover, several time delay points have been introduced in the program to achieve stable levitation in both ZP and MP positions. The number of data collected in ZP and MP positions can be changed from the front panel. Because of the balance drift, a correction factor must be applied to the MP data:

$$MP_{corrected} = MP_{uncorrected} - (ZP)_{average}^{initial} - n * d \quad (22)$$

$$d = \left[ (ZP)_{average}^{final} - (ZP)_{average}^{initial} \right] / (N - 1) \quad (23)$$

where  $n = 0, 1, 2, N-1$  and  $N =$  total number of readings.

## **5. EXPERIMENTAL RESULTS: PURE COMPONENT AND SYNTHETIC NATURAL GAS DENSITY MEASUREMENTS**

### **5.1 Introduction**

We have measured pure components and synthetic natural gas mixtures in this work. We have measured densities for nitrogen, carbon dioxide and methane at high pressures and at various isotherms for apparatus calibration purposes. We have measured 2 synthetic natural gas mixtures in this work in continuation of Ejaz's work as presented in his dissertation [44].

### **5.2 Pure Component Gas Density Measurements**

We have measured pure nitrogen, methane and carbon dioxide for two reasons: first, to check the calibration of the MSD, second, to perform a detailed analysis of force transmission error and to obtain the apparatus fluid specific contribution for our raw density measurements. Results are compared to previously published experimental data and to NIST-12.

These pure components were measured several times between 2005 and 2007 before and after measuring synthetic natural gas densities. We pushed the limits of the MSD apparatus by measuring carbon dioxide gas density at 350 K and at 200 MPa (29,000 psi) during the measurements performed in 2007.

For magnetic levitation based densimeters, measurements at such pressures have not appeared previously. High-pressure, pure component gas density data at 200 MPa are rare. We measured pure nitrogen in March, December of 2005, April-May of 2006 and February-May of 2007. We measured pure methane in December-January of 2006. Additionally, we measured pure carbon dioxide in January of 2006 and April-May of 2007. Table 3 shows the purity of the components, the impurities and the sources of the cylinders. Impurities of the pure component samples were not analyzed in our lab. This information was provided by the sample gas cylinder manufacturers.

TABLE 3

Pure component compositions, impurities and manufacturers.

Component	Formula	Purity [%]	Impurities	Supplier
Nitrogen	N <sub>2</sub>	99.9995	CO < 1 ppm CO <sub>2</sub> < 1 ppm H <sub>2</sub> O < 1 ppm O <sub>2</sub> < 1 ppm	Scott Specialty Gas
Carbon Dioxide	CO <sub>2</sub>	99.99	N/A	Matheson TriGas
Methane	CH <sub>4</sub>	99.99	N/A	Matheson TriGas

For measurements below 41 MPa, the 6,000 psi pressure transducer is used. Above 41 MPa, the 30,000 psi pressure transducer is used. The PRT, pressure transducers and MSD balance readings are collected every 10 to 15 minutes. We took the average and standard deviation of the collected data for each cycle. On the average for each pressure and temperature point, we collected 10 data cycles, approximately 180 minutes.

We calibrated the pressure transducers frequently against a Ruska Deadweight gage. Paroscientific pressure transducers can compensate for temperature changes. We kept the temperature of the aluminum blocks holding the transducers above ambient temperature for better performance. The standard deviation of the aluminum block temperature is generally below 5 mK.

The experimental densities were compared with the values calculated by NIST-12 software, which among other things uses reference a EOS by Span et al. [63] for nitrogen, Setzmann and Wagner [64] for methane and Span and Wagner [65] for carbon dioxide. The percentage relative deviation between experimental and theoretical values is:

$$\Delta\rho/\rho = \left\{ \left( \rho_{\text{exp}} - \rho_{\text{theo}} \right) / \rho_{\text{theo}} \right\} * 100 \quad (40)$$

Table 4 shows the measured density for each pure component at different isotherms for nitrogen measured between March and December of 2005.



TABLE 4

Pure nitrogen experimental density and % deviation from NIST-12 database, 2005.

<b>Nitrogen</b>							
<b>March - December 2005</b>							
<b>Temperature</b>		<b>Pressure</b>		<b>Balance</b>	<b>Density</b>		<b>Error</b>
<b>Average</b>	<b>St. Dev</b>	<b>Average</b>	<b>St. Dev</b>	<b>St. Dev</b>	<b>Exp.</b>	<b>NIST-12</b>	
<b>K</b>	<b>mK</b>	<b>MPa</b>	<b>MPa</b>	<b>mg</b>	<b>kg/m<sup>3</sup></b>	<b>kg/m<sup>3</sup></b>	<b>%</b>
289.990	2.334	6.90	0.017	0.011	80.705	80.707	-0.003
289.983	2.287	13.78	0.047	0.023	158.161	158.204	-0.027
290.009	4.589	20.68	0.127	0.036	227.763	227.840	-0.034
305.190	7.440	6.90	0.009	0.010	76.201	76.155	0.061
305.178	2.048	13.79	0.006	0.005	148.945	148.831	0.077
305.187	2.738	20.69	0.020	0.007	214.575	214.400	0.082
305.198	5.446	27.60	0.055	0.024	271.625	271.408	0.080
305.164	2.926	34.47	0.030	0.016	320.203	319.934	0.084
340.047	11.73	6.90	0.03	0.00	67.503	67.458	0.066
339.969	5.868	13.79	0.02	0.01	131.344	131.251	0.070
339.970	8.824	20.68	0.04	0.01	189.420	189.303	0.062
339.959	9.299	27.58	0.07	0.01	241.054	240.906	0.061
339.991	5.807	34.47	0.08	0.01	286.249	286.045	0.072

The total uncertainty analysis for our density measurements appears in Appendix F. Patil has discussed that the bias error for an MSD is inversely related to molecular weight and suggested an empirical equation for correcting the bias error by using the molecular weight [22]. On the other hand, Ejaz reports some theoretical work on correcting errors caused by FTE [44] and his study is extended in the “Magnetic Suspension Densimeters and Force Transmission Error Phenomena” section. Ejaz did not apply a correction term to his data to correct FTE but presented the raw data. In this work, we apply correction terms to compensate for FTE. Results for pure nitrogen experiments that are completed in 2006 are given in table 5.

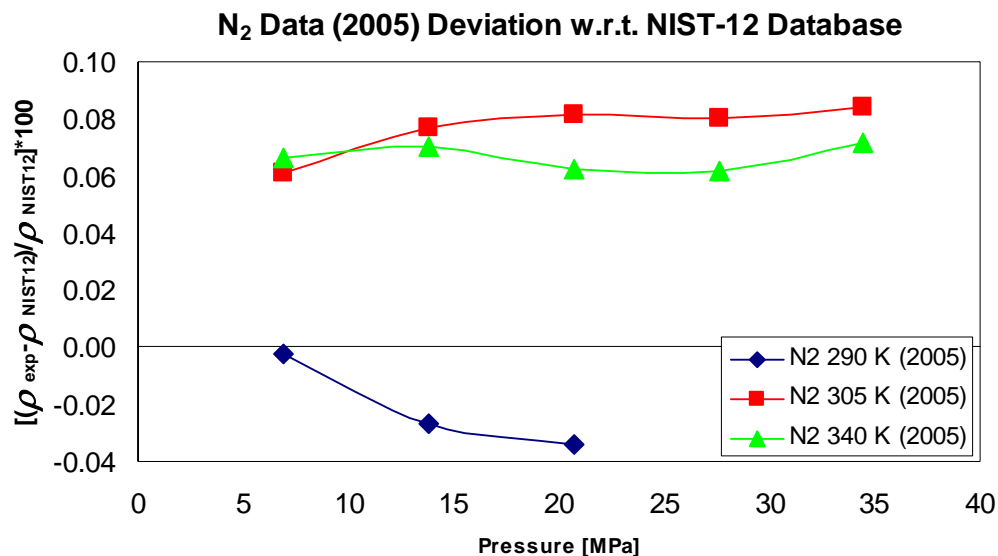


FIGURE 43. Nitrogen density deviations from NIST-12 Database, 2005.

TABLE 5

Pure nitrogen experimental density and % deviation from NIST-12 database, 2006.

Nitrogen ~ April - May 2006							
Temperature		Pressure		Balance	Density		Error
Average K	St. Dev mK	Average MPa	St. Dev MPa	St. Dev mg	Exp. kg/m <sup>3</sup>	NIST-12 kg/m <sup>3</sup>	%
250.365	3.299	15.027	0.044	0.018	208.051	208.000	0.024
250.336	7.627	19.986	0.011	0.041	267.588	267.450	0.052
250.343	6.463	30.000	0.021	0.021	362.355	362.180	0.048
250.366	3.385	50.009	0.051	0.030	482.032	481.810	0.046
250.325	2.723	68.948	0.149	0.042	553.013	552.780	0.042
250.360	3.450	100.008	0.130	0.192	631.065	630.910	0.025
250.366	3.394	124.919	0.182	0.147	676.222	676.290	-0.010
250.368	7.310	149.785	0.244	0.945	712.564	712.930	-0.051
250.398	5.626	164.924	0.333	0.952	731.654	732.270	-0.084
290.066	4.582	6.903	0.026	0.046	80.642	80.719	-0.095
290.065	1.943	20.676	0.026	0.023	227.765	227.770	-0.002
290.084	5.805	34.487	0.035	0.021	337.730	337.629	0.030

TABLE 5 (con't)

<b>Nitrogen</b>							
<b>April - May 2006</b>							
<b>Temperature</b>	<b>St.</b>	<b>Pressure</b>	<b>St.</b>	<b>Balance</b>	<b>Density</b>	<b>NIST-12</b>	<b>Error</b>
<b>Average</b>	<b>Dev</b>	<b>Average</b>	<b>Dev</b>	<b>St. Dev</b>	<b>Exp.</b>	<b>kg/m<sup>3</sup></b>	<b>%</b>
<b>K</b>	<b>mK</b>	<b>MPa</b>	<b>MPa</b>	<b>mg</b>	<b>kg/m<sup>3</sup></b>	<b>kg/m<sup>3</sup></b>	<b>%</b>
293.231	2.104	14.989	0.039	0.030	168.808	168.760	0.028
293.175	2.675	20.016	0.045	0.018	218.782	218.670	0.051
293.214	2.825	29.993	0.020	0.009	302.472	302.310	0.053
293.255	2.052	49.992	0.033	0.009	420.206	420.038	0.040
293.217	1.936	68.889	0.066	0.011	494.660	494.407	0.051
293.252	2.583	99.992	0.119	0.038	578.540	578.405	0.023
293.336	1.885	124.906	0.084	0.030	627.278	627.271	0.001
293.244	4.581	149.876	0.200	0.065	666.755	666.968	-0.032
293.210	4.640	164.776	0.086	0.074	687.146	687.475	-0.048
340.155	3.791	15.006	0.095	0.020	141.937	141.895	0.030
340.091	15.962	20.002	0.018	0.019	183.881	183.829	0.028
340.118	4.429	30.023	0.071	0.021	257.648	257.488	0.062
340.196	5.875	50.006	0.074	0.041	368.567	368.199	0.100
340.233	16.285	68.972	0.153	0.061	443.169	442.830	0.077
340.132	6.606	99.943	0.099	0.122	529.661	529.516	0.027
340.143	16.552	125.000	0.239	0.165	580.955	581.231	-0.047
340.122	9.575	149.978	0.183	0.350	622.114	623.020	-0.145
340.141	2.762	164.915	0.246	0.345	643.886	644.667	-0.121

Deviations of pure nitrogen data from NIST-12 database lie between 0.06% and 0.08% for isotherms 305 and 340 K. For the 290 K isotherm, deviations are between 0.00% and -0.03% for the measurements completed in 2005. These deviations appear in figure 43.

Deviation of pure nitrogen from NIST-12 database lie between -0.1% and +0.1% for 250, 290, 293 and 340 K isotherms and shown in figure 44. We have collected more points in 2006 than 2005 measurements. Results for pure nitrogen experiments that are completed in 2007 are given in table 6.

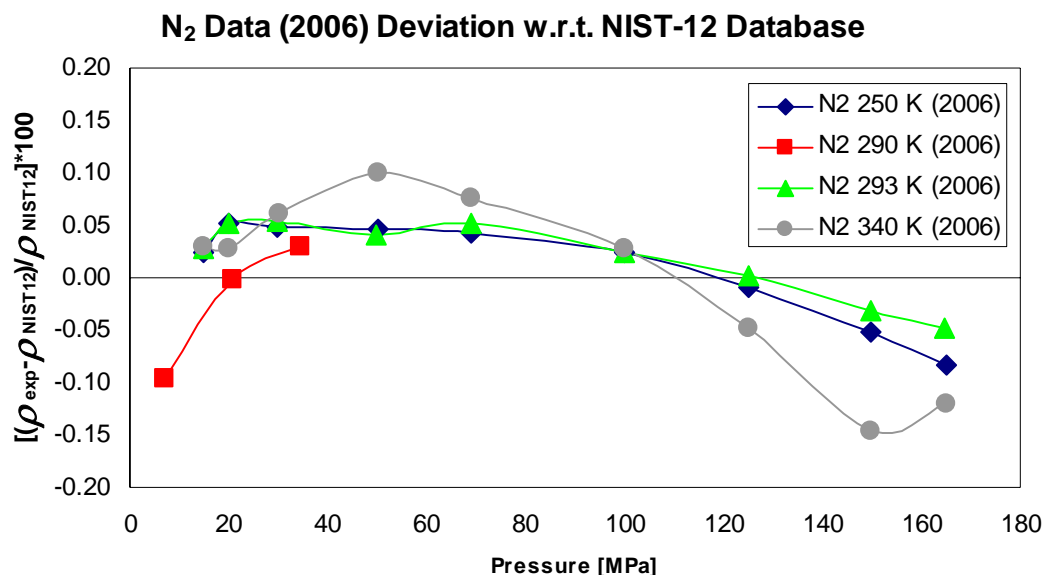


FIGURE 44. Nitrogen density deviations from NIST-12 Database, 2006.

TABLE 6

Pure nitrogen experimental density and % deviation from NIST-12 database, 2007.

Nitrogen							
January - March 2007							
Temperature		Pressure		Balance	Density		
Average	St. Dev	Average	St. Dev	St. Dev	Exp.	NIST-12	Error
K	mK	MPa	MPa	mg	kg/m <sup>3</sup>	kg/m <sup>3</sup>	%
264.815	4.200	0.970	0.0025	0.007	12.333	12.409	-0.615
264.814	3.781	1.939	0.0035	0.005	24.848	24.918	-0.282
264.806	2.713	3.930	0.0036	0.004	50.833	50.896	-0.124
264.826	2.884	5.995	0.0057	0.006	77.964	78.031	-0.086
264.804	2.905	7.981	0.0134	0.008	104.060	104.100	-0.038
264.833	4.324	9.832	0.0135	0.007	128.088	128.110	-0.017
264.800	3.460	15.002	0.0071	0.014	192.422	192.380	0.022
264.808	4.805	20.003	0.0879	0.007	248.458	248.370	0.035
264.819	3.378	24.996	0.0275	0.007	297.313	297.180	0.045
264.829	3.447	29.978	0.0276	0.015	339.328	339.160	0.050
264.779	2.816	35.074	0.0356	0.007	376.375	376.220	0.041

TABLE 6 (con't)

<b>Nitrogen ~ January - March 2007</b>							
<b>Temperature</b>		<b>Pressure</b>		<b>Balance</b>	<b>Density</b>		
<b>Average</b>	<b>St. Dev</b>	<b>Average</b>	<b>St. Dev</b>	<b>St. Dev</b>	<b>Exp.</b>	<b>NIST-12</b>	<b>Error</b>
<b>K</b>	<b>mK</b>	<b>MPa</b>	<b>MPa</b>	<b>mg</b>	<b>kg/m<sup>3</sup></b>	<b>kg/m<sup>3</sup></b>	<b>%</b>
264.815	8.145	49.982	0.0495	0.017	459.349	459.130	0.048
264.822	3.726	74.794	0.1827	0.017	550.025	549.740	0.052
264.823	3.178	100.437	0.2733	0.009	613.600	613.210	0.064
264.794	3.080	124.999	0.1354	0.051	659.503	659.200	0.046
264.799	4.203	149.512	0.1536	0.040	696.693	696.360	0.048
293.146	6.871	0.969	0.0019	0.0064	11.111	11.161	-0.448
293.147	5.523	1.937	0.0037	0.0160	22.309	22.347	-0.172
293.148	8.819	3.928	0.0076	0.0047	45.362	45.408	-0.101
293.148	9.140	5.994	0.0135	0.0055	69.258	69.287	-0.042
293.146	6.452	7.978	0.0270	0.0118	92.006	92.021	-0.016
293.153	5.970	9.829	0.0236	0.0062	112.939	112.930	0.008
293.149	4.589	14.883	0.0055	0.0115	167.752	167.710	0.025
293.150	6.787	19.990	0.0093	0.0246	218.530	218.450	0.037
293.150	3.866	24.965	0.0155	0.0076	262.845	262.730	0.044
293.143	7.431	29.985	0.0123	0.0183	302.479	302.340	0.046
293.150	3.461	35.006	0.0310	0.0186	337.482	337.310	0.051
293.145	3.335	39.943	0.0276	0.0159	367.969	367.790	0.049
293.149	7.166	50.167	0.0294	0.0075	421.204	420.990	0.051
293.148	4.712	75.007	0.1640	0.0115	514.198	513.930	0.052
293.170	3.295	99.996	0.0390	0.0073	578.824	578.510	0.054
293.160	4.600	125.617	0.1660	0.0315	629.090	628.700	0.062
293.153	5.035	151.050	0.5070	0.0095	669.201	668.750	0.067
298.136	8.563	10.010	0.0976	0.02986	112.667	112.660	0.006
298.166	7.752	30.021	0.0852	0.02933	297.082	296.940	0.048
298.146	13.736	49.826	0.1111	0.02029	413.395	413.170	0.054
298.166	4.879	74.989	0.0402	0.00488	508.158	507.870	0.057
298.144	12.970	100.116	0.1424	0.02922	573.548	573.200	0.061
298.154	9.155	124.742	0.1751	0.03633	622.316	621.900	0.067
298.162	8.536	151.095	0.6563	0.03374	664.306	663.820	0.073

TABLE 6 (con't)

<b>Nitrogen</b>							
<b>January - March 2007</b>							
<b>Temperature</b>		<b>Pressure</b>		<b>Balance</b>	<b>Density</b>		
<b>Average</b>	<b>St. Dev</b>	<b>Average</b>	<b>St. Dev</b>	<b>St. Dev</b>	<b>Exp.</b>	<b>NIST-12</b>	<b>Error</b>
<b>K</b>	<b>mK</b>	<b>MPa</b>	<b>MPa</b>	<b>mg</b>	<b>kg/m<sup>3</sup></b>	<b>kg/m<sup>3</sup></b>	<b>%</b>
350.009	9.340	0.979	0.002	0.0071	9.361	9.412	-0.539
350.004	8.593	2.977	0.005	0.0069	28.460	28.518	-0.204
349.990	9.279	4.921	0.007	0.0139	46.861	46.927	-0.141
349.995	9.692	5.975	0.005	0.0280	56.756	56.808	-0.091
349.991	7.829	7.484	0.007	0.0152	70.761	70.817	-0.079
350.004	9.045	9.973	0.031	0.0071	93.499	93.497	0.002
349.992	5.454	13.789	0.010	0.0078	127.075	127.070	0.004
350.005	4.247	17.234	0.023	0.0193	155.961	155.930	0.020
349.996	7.360	20.680	0.017	0.0145	183.361	183.310	0.028
349.987	9.692	24.133	0.014	0.0126	209.295	209.210	0.041
349.986	9.620	27.583	0.039	0.0108	233.605	233.540	0.028
350.000	10.662	29.851	0.033	0.0251	248.800	248.710	0.036
349.999	5.391	34.691	0.031	0.0082	279.138	279.020	0.042
350.047	8.085	49.947	0.310	0.0080	358.923	358.680	0.068
349.994	5.447	74.982	0.083	0.0445	453.178	452.950	0.050
350.009	8.110	99.978	0.089	0.0162	520.578	520.320	0.050
350.003	4.617	124.454	0.394	0.0325	571.613	571.320	0.051
349.998	7.731	150.329	0.458	0.0346	615.308	615.000	0.050

In 2007, we have collected both high pressure and low-pressure data with the MSD for pure components. We have pushed the limits of the MSD by going to pressures up to 200 MPa, which is the maximum operating pressure for the MSD. For pressures above 10 MPa for all four isotherms (264.8, 293.15, 298.15 and 350 K), we have observed deviations from NIST-12 for nitrogen between -0.02% and +0.06% as shown in figure 45. We also have measured gas densities for pressures as low as 1 MPa.

We observe nitrogen density deviations from NIST-12 at low-pressure for all isotherms between -0.6% and -0.03% as shown in figure 46. Poor performance of the MSD is expected because it is not designed for low pressure operation.

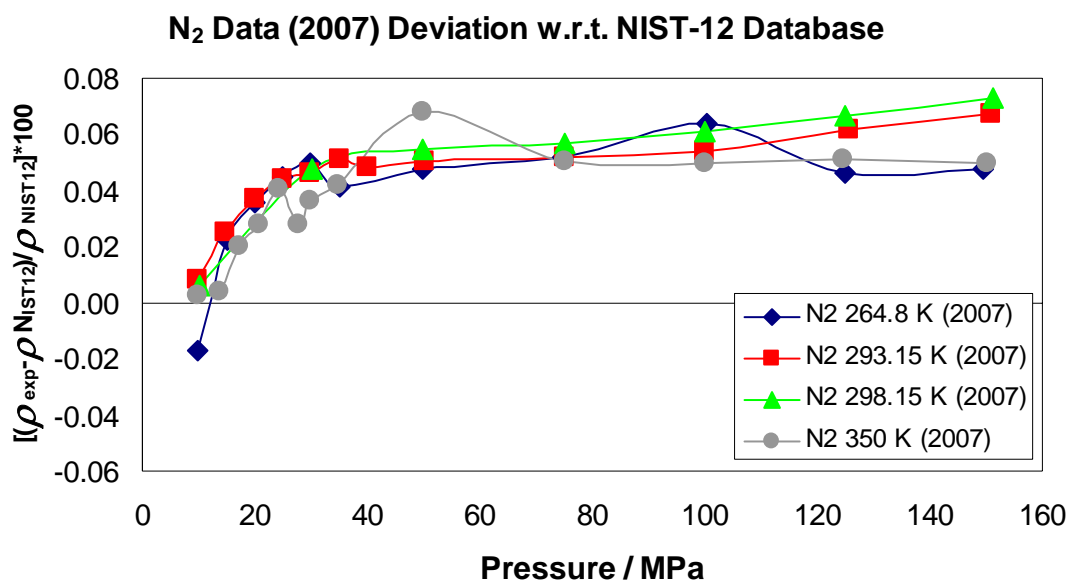


FIGURE 45. Nitrogen density deviations from NIST-12 Database, high pressure, 2007.

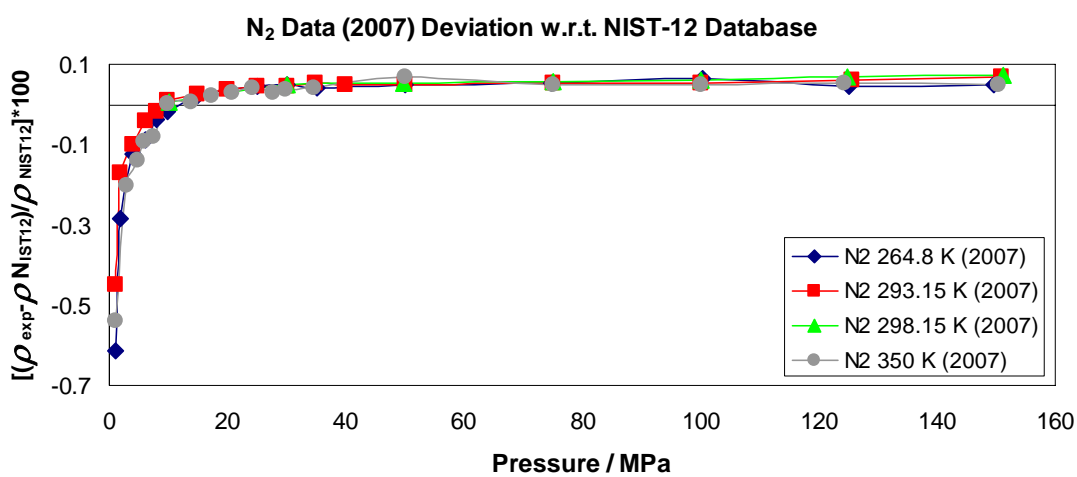


FIGURE 46. Nitrogen density deviations from NIST-12 Database, all points, 2007.

TABLE 7

Pure carbon dioxide experimental density and % deviation from NIST-12 database, 2006.

Raw Data - Carbon dioxide							
January 2006							
Temperature		Pressure		Balance	Density		Error
Average	St. Dev	Average	St. Dev	St. Dev	Exp.	NIST-12	
K	mK	MPa	MPa	mg	kg/m <sup>3</sup>	kg/m <sup>3</sup>	
309.224	7.552	6.896	0.029	0.033	207.099	206.809	0.141
309.294	3.120	20.721	0.163	0.078	866.718	865.846	0.101
309.259	7.760	34.515	0.326	0.086	946.990	946.311	0.072
338.348	2.657	6.904	0.008	0.014	146.088	145.979	0.074
338.377	5.926	20.720	0.244	0.179	703.344	702.799	0.078
338.365	5.528	34.494	0.170	0.060	841.115	840.527	0.070

We also have measured pure carbon dioxide densities in 2006 and 2007. We have observed deviations between 0.08% and 0.14% for 2006 measurements as shown in table 7 and figure 47. However, we have few measurements in 2006.

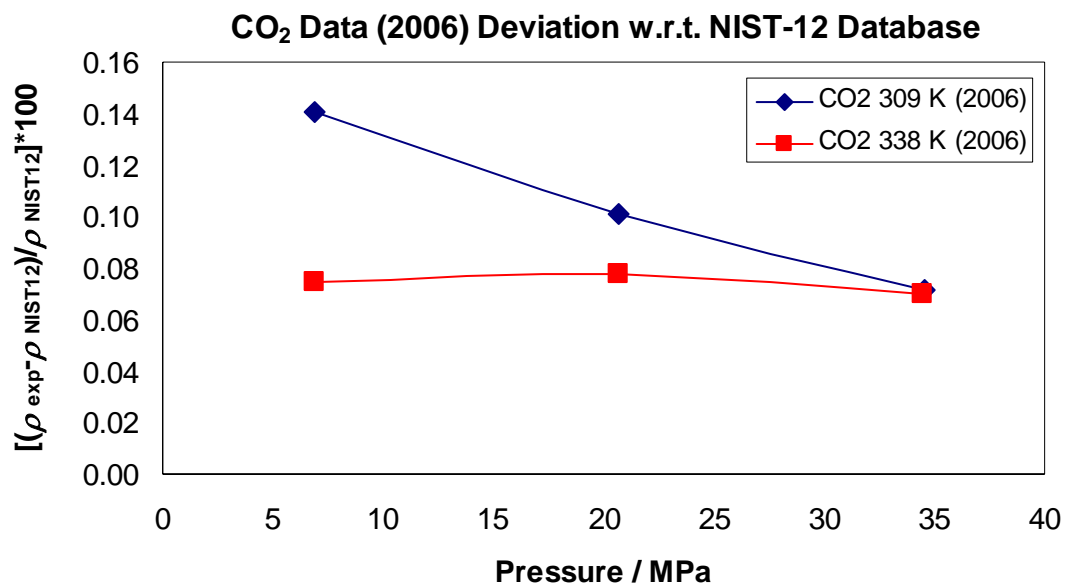


FIGURE 47. Carbon dioxide density deviations from NIST-12 Database, 2006.



In 2007, we again have investigated pure carbon dioxide. This time, we pushed the limits of the MSD by going up to 200 MPa in the measuring cell. We have measured gas densities for three different isotherms 310, 330 and 350 K. Percentage deviations from NIST-12 appear in table 8 and figure 48. We observed deviations between -0.10% and 0.10%.

TABLE 8

Pure carbondioxide experimental density and % deviation from NIST-12 database, 2007.

<b>Carbon dioxide</b>							
<b>April-May 2007</b>							
<b>Temperature</b>	<b>St.</b>	<b>Pressure</b>	<b>St.</b>	<b>Balance</b>	<b>Density</b>		<b>Error</b>
<b>Average</b>	<b>Dev</b>	<b>Average</b>	<b>Dev</b>	<b>St. Dev</b>	<b>Exp.</b>	<b>NIST-12</b>	
<b>K</b>	<b>mK</b>	<b>MPa</b>	<b>MPa</b>	<b>mg</b>	<b>kg/m<sup>3</sup></b>	<b>kg/m<sup>3</sup></b>	<b>%</b>
309.989	5.053	10.042	0.038	0.047	687.5661378	687.881	-0.046
309.993	6.481	15.409	0.139	0.041	808.2143568	808.080	0.037
310.008	5.698	20.057	0.287	0.022	856.8974606	856.717	0.041
309.983	4.875	24.872	0.072	0.034	892.7486677	892.502	0.048
309.982	4.194	30.041	0.096	0.015	922.7138558	922.319	0.043
309.993	4.808	50.060	0.114	0.011	1000.728673	1000.552	0.018
310.005	4.708	75.040	0.264	0.025	1063.08784	1063.046	0.004
310.001	6.814	79.469	0.284	0.013	1072.074353	1072.062	0.001
310.002	6.176	92.373	0.131	0.009	1095.975466	1095.939	0.003
310.008	4.543	124.811	0.436	0.020	1145.132653	1144.939	0.017
310.007	5.884	139.925	0.497	0.034	1164.355348	1164.071	0.024
309.990	6.881	149.813	0.225	0.016	1176.043647	1175.678	0.031
309.991	3.934	154.978	0.316	0.012	1181.867783	1181.467	0.034
309.996	5.400	159.934	0.290	0.013	1187.291064	1186.864	0.036
309.996	3.400	164.827	0.318	0.013	1192.533935	1192.064	0.039
310.005	3.600	169.891	0.130	0.008	1197.793614	1197.295	0.042
309.980	5.000	174.935	0.240	0.012	1202.963554	1202.432	0.044
310.001	2.800	179.219	0.430	0.010	1207.198067	1206.630	0.047
310.013	3.419	203.792	0.396	0.016	1207.198067	1206.630	0.047

TABLE 8 (con't)

<b>Carbon dioxide</b>							
<b>April-May 2007</b>							
<b>Temperature</b>		<b>Pressure</b>		<b>Balance</b>	<b>Density</b>		<b>Error</b>
<b>Average</b>	<b>St. Dev</b>	<b>Average</b>	<b>St. Dev</b>	<b>St. Dev</b>	<b>Exp.</b>	<b>NIST-12</b>	
<b>K</b>	<b>mK</b>	<b>MPa</b>	<b>MPa</b>	<b>mg</b>	<b>kg/m<sup>3</sup></b>	<b>kg/m<sup>3</sup></b>	<b>%</b>
330.032	4.809	10.011	0.017	0.062	310.675	310.808	-0.043
330.015	4.034	14.736	0.262	0.350	626.264	626.294	-0.005
330.024	3.846	19.773	0.325	0.123	739.881	739.774	0.014
330.033	4.466	24.928	0.134	0.030	801.184	800.954	0.029
330.006	8.917	29.930	0.125	0.044	842.579	842.141	0.052
330.016	3.693	50.142	0.131	0.021	943.435	943.106	0.035
329.985	4.483	75.031	0.224	0.022	1016.459	1016.237	0.022
330.015	6.085	100.092	0.115	0.016	1068.122	1067.890	0.022
330.001	4.731	124.826	0.370	0.015	1108.208	1107.890	0.029
330.011	5.820	149.910	0.289	0.047	1141.925	1141.482	0.039
330.018	4.805	159.641	1.192	0.016	1153.612	1153.144	0.041
330.038	5.684	169.715	0.308	0.088	1165.064	1164.540	0.045
330.030	4.333	180.426	0.209	0.007	1176.680	1176.062	0.053
330.023	4.442	197.158	0.165	0.010	1193.569	1192.893	0.057
350.000	4.239	9.216	0.023	0.035	201.250	201.673	-0.210
350.006	5.725	20.068	0.175	0.014	614.242	615.692	-0.235
350.006	8.012	30.074	0.068	0.038	758.541	759.659	-0.147
350.004	7.265	40.426	0.110	0.021	835.463	836.238	-0.093
350.024	3.748	50.215	0.203	0.055	885.929	885.629	0.034
350.010	8.067	74.987	0.304	0.014	970.469	969.922	0.056
350.003	8.350	99.737	1.022	0.022	1027.834	1027.203	0.061
350.012	5.908	119.508	0.315	0.015	1063.895	1063.119	0.073
350.020	6.389	149.482	0.157	0.016	1108.571	1107.626	0.085
350.034	7.804	159.981	0.572	0.023	1122.180	1121.176	0.090
349.995	7.438	170.058	0.335	0.034	1134.534	1133.493	0.092
350.002	5.242	175.085	0.411	0.009	1140.473	1139.343	0.099
349.991	5.361	183.839	0.188	0.013	1150.325	1149.201	0.098
350.005	4.093	199.519	0.423	0.011	1167.462	1165.773	0.145

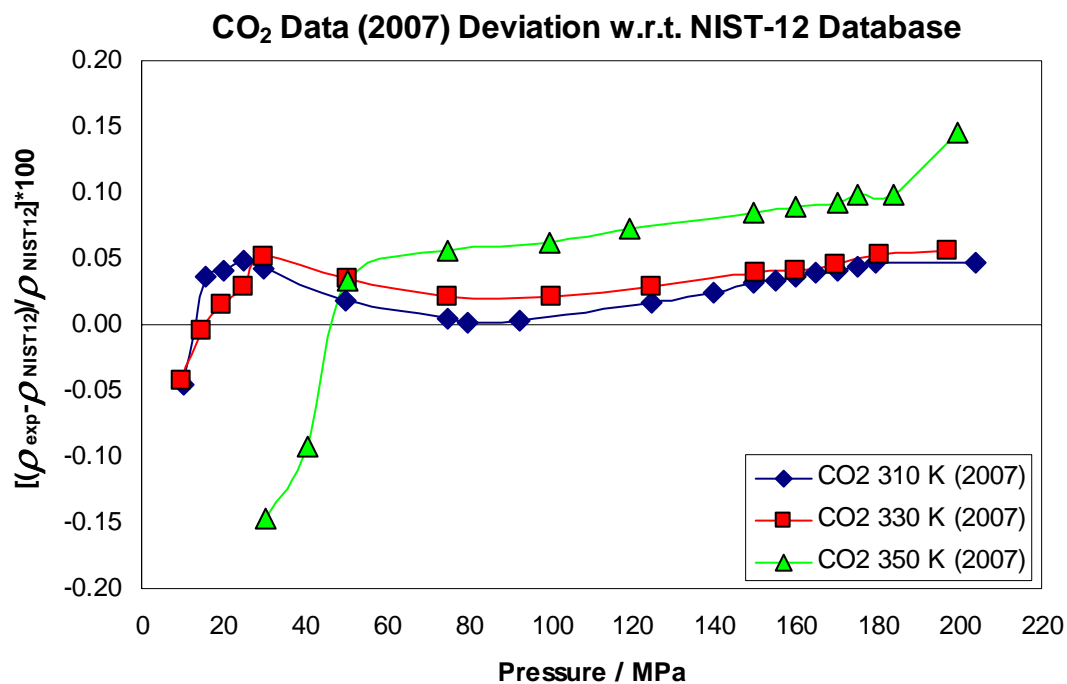


FIGURE 48. Carbondioxide density deviations from NIST-12 Database, all points, 2007.

TABLE 9

Pure methane experimental density and % deviation from NIST-12 database, 2005.

Methane							
April-May 2005							
Temperature		Pressure		Balance	Density		Error
Average	St. Dev	Average	St. Dev	St. Dev	Exp.	NIST-12	
K	mK	MPa	MPa	mg	kg/m <sup>3</sup>	kg/m <sup>3</sup>	%
305.250	6.797	6.914	0.013	0.015	48.627	48.566	0.126
305.294	11.143	20.686	0.027	0.027	155.094	154.916	0.115
305.274	5.982	34.435	0.054	0.014	223.511	223.256	0.114
338.255	5.159	6.903	0.025	0.010	42.067	42.040	0.066
338.046	4.708	20.670	0.047	0.018	130.219	130.062	0.121
338.051	5.737	34.477	0.119	0.032	195.688	195.466	0.113

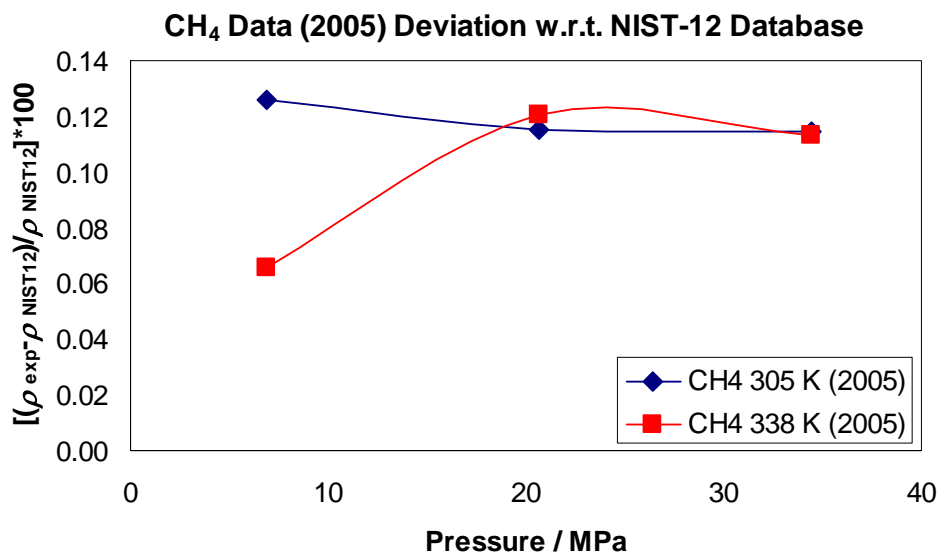


FIGURE 49. Methane density deviations from NIST-12, all points, 2005.

Because methane is the major component of natural gas mixtures, we have measured methane densities for a few pressure points at two different temperatures for calibration purposes. We observed deviations between 0.06% and 0.12% for pure methane as given in table 9 and figure 49.

### 5.2.1 Comparison of Pure Component Data with Literature

We have compared our data with the available literature data for nitrogen, carbon dioxide and methane. Mainly, we look at the deviations from NIST-12. We have observed a close match between our data and previously published work on pure components. We have chosen literature data on components with purity of 99.99 mole % or better. As discussed in Appendix F, the total experimental uncertainty caused by temperature and pressure measurements for pure components are on the order of  $\pm 0.03$  % in our laboratory. For nitrogen, methane and carbon dioxide, measurements from a two sinker densimeter has smaller deviations with respect to NIST-12 predictions.

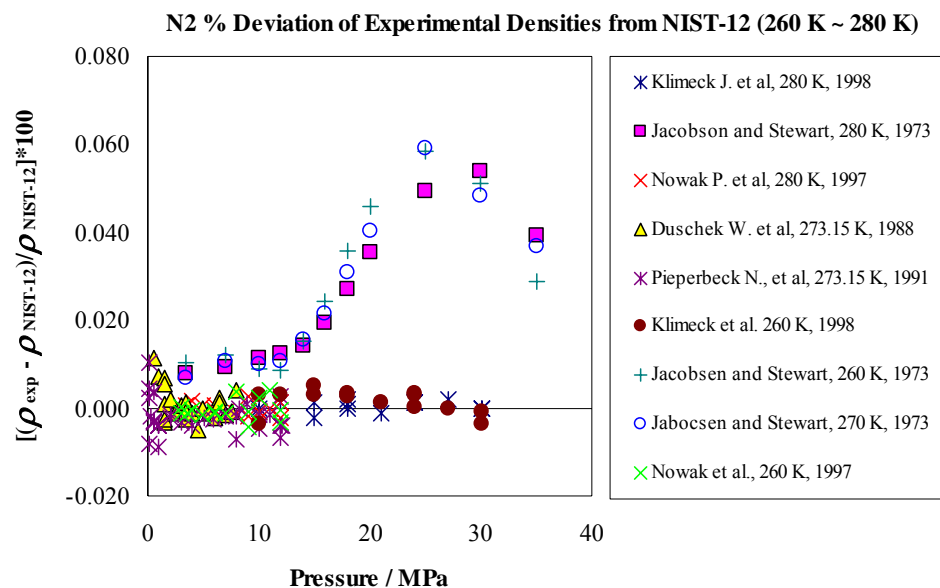


FIGURE 50. Literature nitrogen deviations from NIST-12 database for temperatures between 260 K and 280 K [39, 66-69].

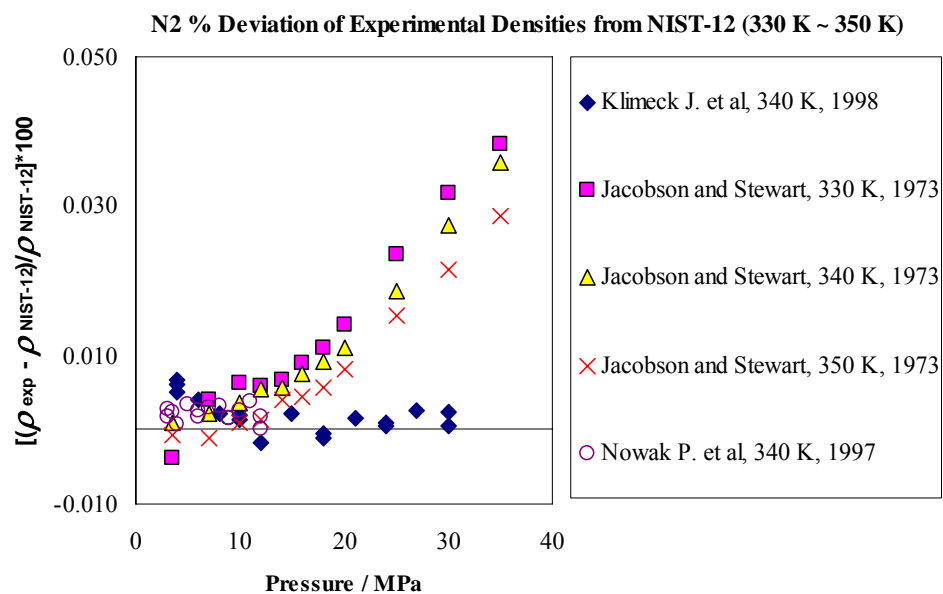


FIGURE 51. Literature nitrogen deviations from NIST-12 database for temperatures between 330 K and 350 K [39, 66-69].

From plots, it is evident that the two-sinker method has superior performance especially at low densities. Literature data percentage deviation from NIST-12 database for nitrogen is given in figures 50 and 51.

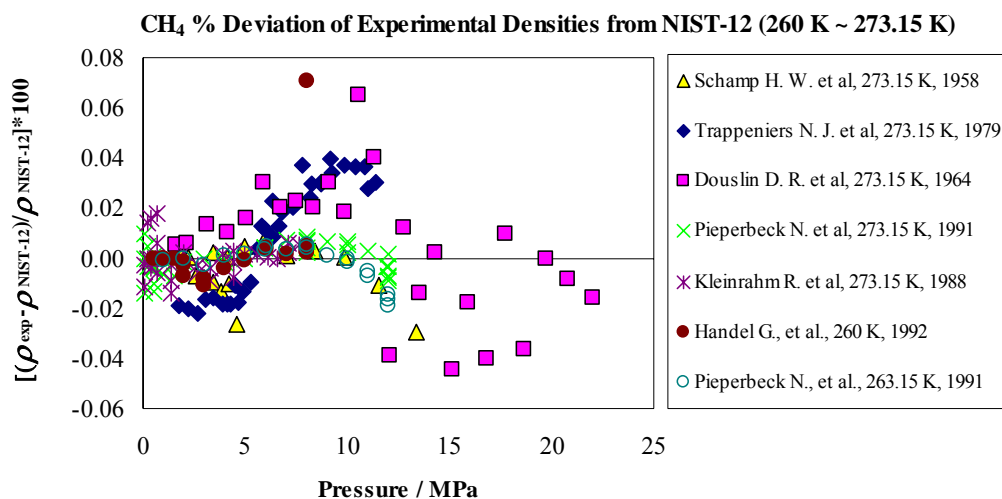


FIGURE 52. Literature methane deviations from NIST-12 database for temperatures between 260 K and 273.15 K [68, 70-73].

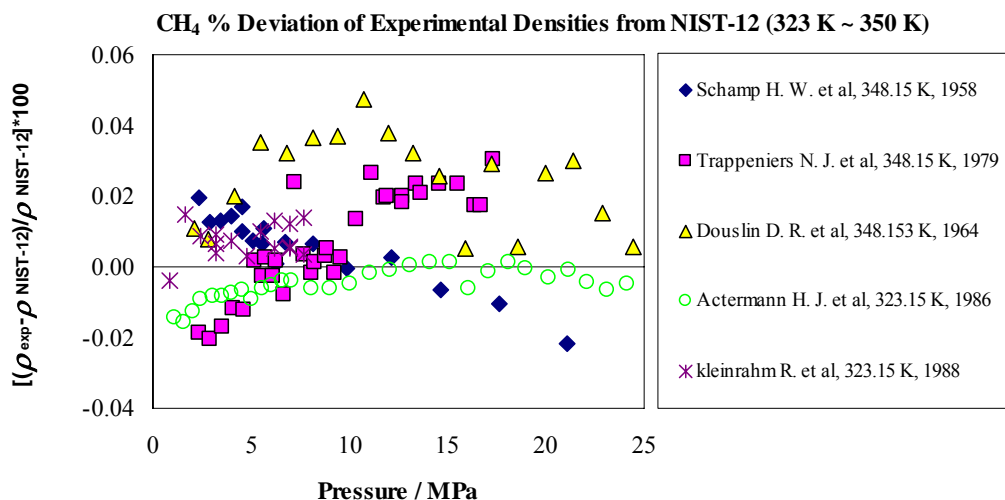


FIGURE 53. Literature methane deviations from NIST-12 database for temperatures between 323 K and 350 K [70-74].

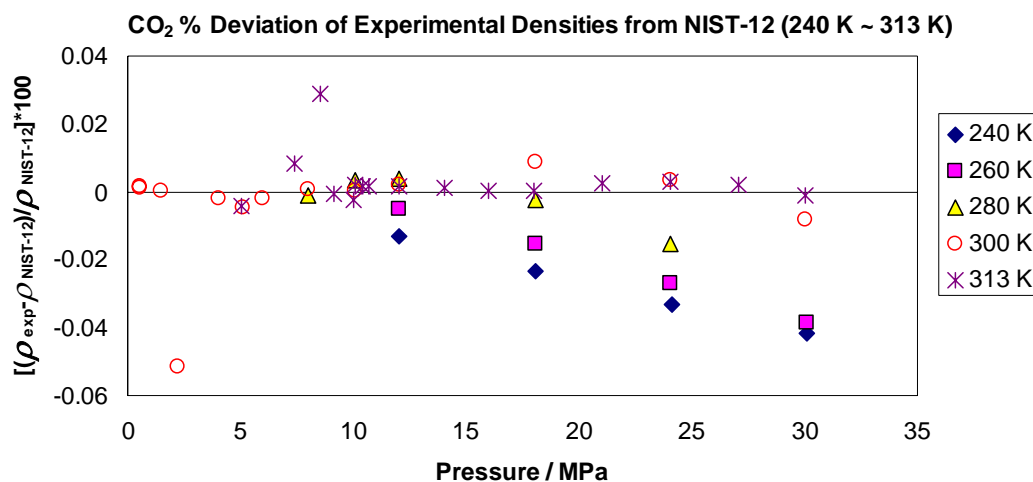


FIGURE 54. Literature carbon dioxide deviations from NIST-12 database for temperatures between 240 K and 313 K [76].

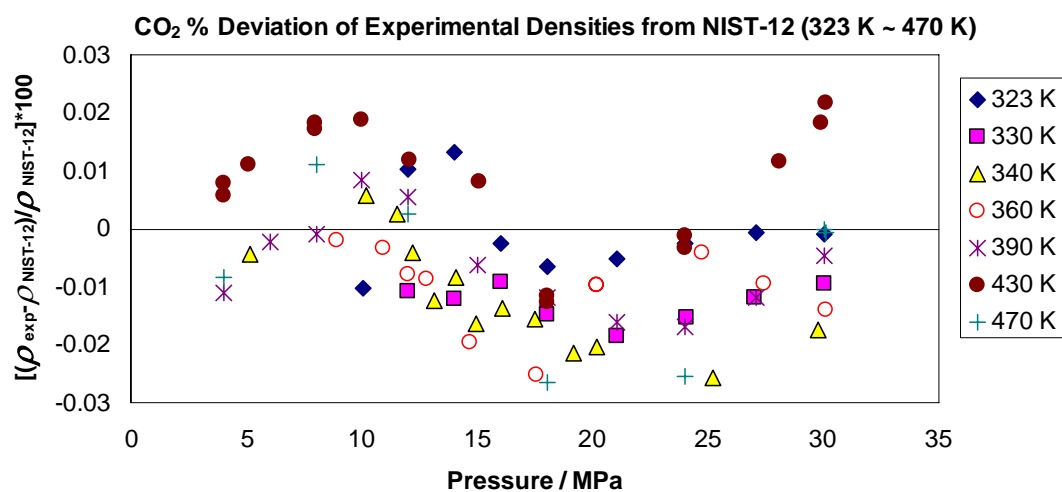


FIGURE 55. Literature carbon dioxide deviations from NIST-12 database for temperatures between 323 K and 470 K [76].

The literature data on methane include measurements done by Händel et al. [73] using a two-sinker MSA, Pieperbeck et al. [68] using a two-sinker MSA, Kleinrahm et al. [25] using a two-sinker MSA, Achtermann et al. [75] using the refractive index method, Trappeniers et al. [71] using a piezometer, Douslin et al. [72] using a pycnometer and Schamp et al. [70] using the piezometer method. The deviations of the methane data are shown in figures 52 and 53. Figure 54 and 55 shows the deviations of experimental carbon dioxide density from NIST-12. Presented data is measured by Klimeck et. al. with a two-sinker densimeter [76].

### **5.3 Synthetic Natural Gas Density Measurements**

The main objective of this work is to simulate natural gas like mixtures under normal and extreme conditions and to obtain high accuracy P- $\rho$ -T data for them. These high accuracy P- $\rho$ -T data will be useful in developing a new equation of state that will be used for natural gas custody transfer. In this work, we also will simulate reservoir conditions by going up to 150 MPa and 450 K. Such experiments for synthetic natural gas mixtures have not been performed previously with state-of-the art MSD apparatus.

Ejaz presented uncorrected data for synthetic natural gas (SNG) mixtures 3 and 5 in his dissertation [44]. Here, we applied appropriate FTE correction terms for SNG 3 and SNG 5 and presented Ejaz's final data. Additionally, as a continuation of Ejaz's work, we studied two more synthetic natural gas mixtures, SNG 4 and SNG 6. We also presented phase envelopes for all SNG mixtures, which are unpublished work of Martinez [77]. Based upon the experimental phase envelope data, we avoided two phases in the density measuring cell. We generally charged our sample in the MSD measuring cell minimum 150 psi above cricondenbar and 10 K above cricondentherm. We also placed trace heaters on the tubes and manifolds to avoid possible condensation in the tubes. Like pure components, we did not check the compositions of the samples before and after the measurements; calculations were performed based on the gas suppliers' certificate.



### 5.3.1 SNG 3 and SNG 5 Measurements

When Ejaz presented the data for SNG 3 and SNG 5, the corrections for FTE were not ready. Therefore the data were uncorrected raw data. As discussed in section 3 of this work, we did numerical analyses on pure components to deduce a correction term. SNG 3 and SNG 5 mixture compositions are given in table 10 and table 11.

TABLE 10

SNG 3 mixture compositions.

<b>Component</b>	<b>Mol %</b>	<b>Component</b>	<b>Mol %</b>
methane	0.89982	isopentane	0.00300
ethane	0.03009	n-pentane	0.00300
propane	0.01506	nitrogen	0.01697
isobutane	0.00752	carbon dioxide	0.01701
n-butane	0.00753		

The densities of SNG 3 were measured at three different temperatures, 250 K, 350 K and 450 K in the pressure range of 10 to 165 MPa (1,450 psia ~ 23,925 psia). The data were compared to both AGA8-DC92 and GERG-2004. For GERG-2004 calculations REFPROP program is used. SNG3 and SNG 5 have compositions that can be classified as falling under the ‘normal range’ as defined by the AGA8-DC92 report where the C<sub>6+</sub> fraction is lower than 0.2%. Corrected experimental data for SNG 3 is given in table 12.

TABLE 11

SNG 5 mixture compositions.

<b>Component</b>	<b>Mol</b>	<b>Component</b>	<b>Mol %</b>
Methane	0.89975	Isopentane	0.00450
Ethane	0.02855	n-Pentane	0.00450
Propane	0.01427	Nitrogen	0.01713
Isobutane	0.00709	Carbon dioxide	0.01699
n-Butane	0.00722		

TABLE 12

SNG 3 experimental P- $\rho$ -T data (after correction term).

**Synthetic Natural Gas Mixture 3 (SNG-3)**  
May - June 2006

Temperature		Pressure		Balance		Density			Relative Deviation	
Average [K]	St. Dev [mK]	Average [Mpa]	St. Dev [Mpa]	St. Dev [mg]	Exp. [kg/m <sup>3</sup> ]	AGA8-DC92 [kg/m <sup>3</sup> ]	GERG-2004 [kg/m <sup>3</sup> ]	AGA8-DC92 [%]	GERG-2004 [%]	
249.986	4.179	14.995	0.028	0.0458	231.630	233.666	231.820	-0.849	-0.060	
250.033	8.938	29.999	0.096	0.0202	316.601	317.639	315.320	-0.305	0.429	
250.055	6.429	49.993	0.237	0.0937	361.567	362.148	360.190	-0.138	0.405	
249.991	7.555	68.972	0.051	0.0617	387.854	388.049	386.520	-0.028	0.367	
249.997	4.640	100.218	0.187	0.0747	417.868	417.549	416.600	0.099	0.327	
249.969	2.328	149.856	0.120	0.0474	450.614	449.693	449.510	0.227	0.268	
349.983	10.776	9.998	0.019	0.026	70.393	70.457	70.423	-0.068	-0.020	
350.020	3.805	29.988	0.064	0.027	200.174	200.080	199.810	0.069	0.204	
350.030	4.747	49.989	0.102	0.054	270.063	269.967	269.320	0.058	0.298	
349.992	5.373	68.941	0.207	0.025	309.606	309.553	308.760	0.040	0.296	
350.028	4.590	99.948	0.097	0.022	351.900	351.843	350.980	0.039	0.285	
350.012	5.212	149.913	0.185	0.044	395.705	395.580	394.760	0.054	0.262	
449.986	8.631	9.994	0.009	0.019	50.376	50.411	50.392	-0.048	-0.010	
450.000	7.570	29.976	0.060	0.019	142.430	142.361	142.290	0.070	0.120	
449.998	7.604	49.981	0.093	0.018	208.047	207.870	207.710	0.106	0.183	
450.000	5.945	68.945	0.159	0.021	251.087	251.014	250.660	0.050	0.192	
449.989	5.648	99.967	0.168	0.020	299.594	299.580	299.070	0.026	0.196	
450.000	9.251	149.899	0.306	0.027	350.282	350.155	349.720	0.057	0.182	

Deviations from AGA8-DC92 EOS and GERG-2004 EOS for SNG 3 are presented in figures 56 and 57 respectively. Corrected experimental data for SNG 5 is given in table 13.

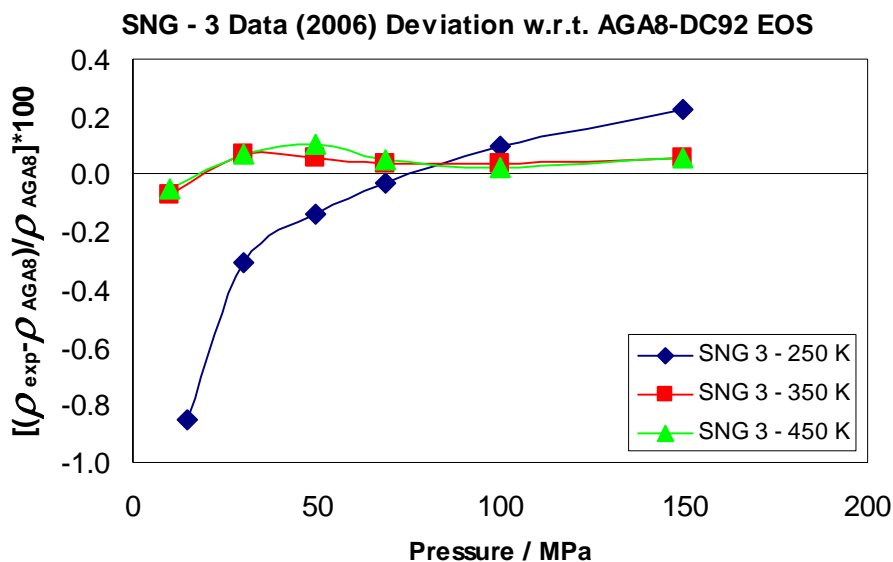


FIGURE 56. Density deviations for SNG 3 from AGA8-DC92 EOS.

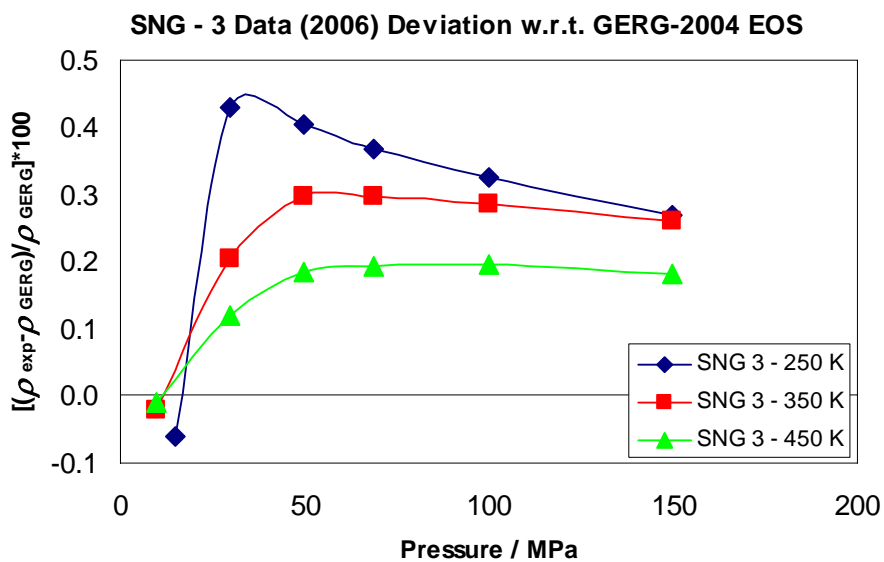


FIGURE 57. Density deviations for SNG 3 from GERG-2004 EOS.

Table 13

SNG 5 experimental P- $\rho$ -T data (after correction term).

Synthetic Natural Gas Mixture 5 (SNG-5) June - July 2006												
Temperature		Pressure		Balance		Density			Relative Deviation			
Average	St. Dev	Average	St. Dev	St. Dev	St. Dev	Exp.	AGA8-DC92	GERG-2004	AGA8-DC92	GERG-2004		
[K]	[mK]	[Mpa]	[Mpa]	[mg]	[mg]	[kg/m3]	[kg/m3]	[kg/m3]	[%]	[%]		
249.954	2.754	14.972	0.048	0.006	0.006	232.960	235.762	233.470	-1.166	-0.196		
249.955	2.515	29.966	0.064	0.030	0.030	317.817	319.286	316.280	-0.437	0.509		
250.024	2.623	49.999	0.270	0.024	0.024	363.087	363.597	360.910	-0.117	0.626		
250.025	5.275	68.966	0.244	0.017	0.017	389.317	389.329	387.060	0.020	0.606		
249.946	1.915	99.877	0.279	0.025	0.025	419.314	418.553	416.840	0.205	0.617		
250.011	4.646	149.957	0.288	0.048	0.048	452.536	450.973	449.950	0.369	0.598		
349.950	5.063	9.988	0.010	0.016	0.016	70.756	70.828	70.793	-0.080	-0.030		
349.980	5.449	29.997	0.033	0.086	0.086	201.894	201.293	200.890	0.321	0.522		
350.011	7.905	49.989	0.095	0.089	0.089	272.432	271.174	270.210	0.486	0.845		
349.977	3.739	68.881	0.166	0.060	0.060	311.161	310.641	309.430	0.190	0.582		
349.977	4.593	99.889	0.088	0.025	0.025	353.912	352.966	351.570	0.291	0.689		
350.015	5.319	149.888	0.131	0.031	0.031	398.143	397.520	395.260	0.179	0.752		
449.992	6.774	10.004	0.011	0.027	0.027	50.699	50.727	50.710	-0.034	-0.001		
449.989	7.921	29.976	0.041	0.031	0.031	143.232	143.103	142.990	0.111	0.190		
449.998	13.754	49.978	0.053	0.019	0.019	209.097	208.803	208.500	0.162	0.307		
450.029	5.318	68.937	0.079	0.021	0.021	252.213	251.994	251.410	0.108	0.341		
449.994	7.602	99.959	0.280	0.021	0.021	300.767	300.617	299.760	0.071	0.357		
449.995	13.224	149.926	0.193	0.021	0.021	351.512	351.310	350.340	0.079	0.356		

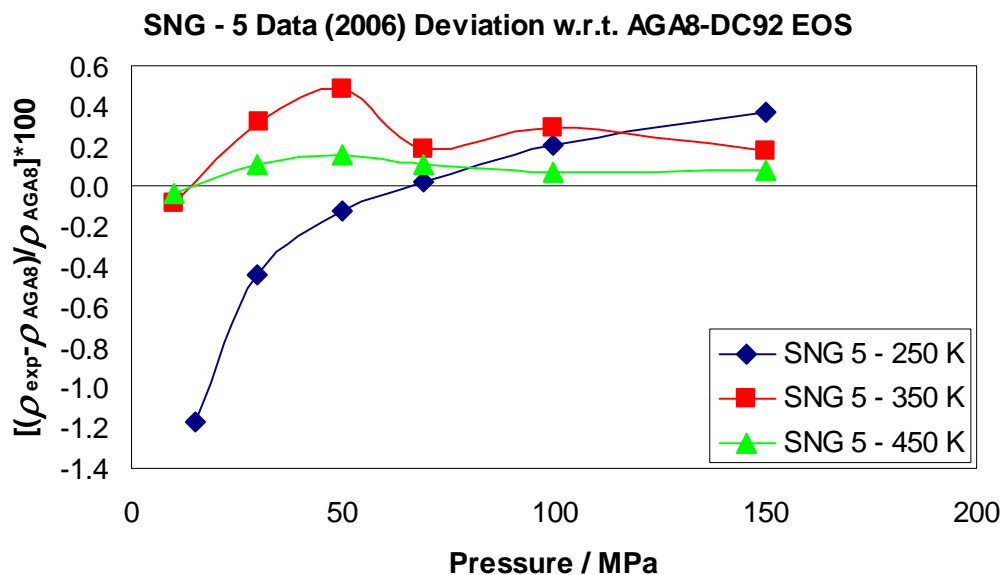


FIGURE 58. Density deviations for SNG 5 from AGA8-DC92 EOS.

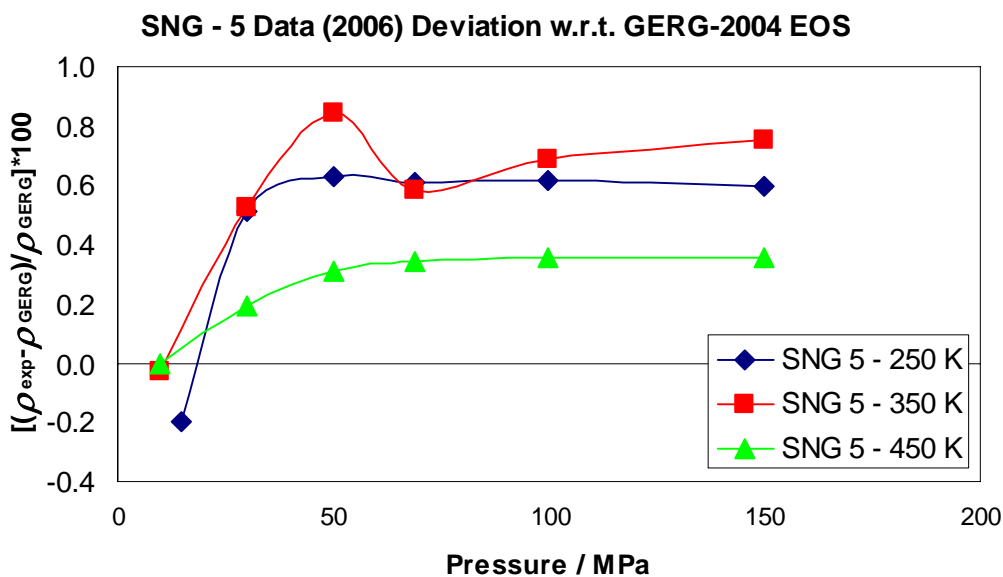


FIGURE 59. Density deviations for SNG 5 from GERG-2004 EOS.

Deviations from AGA8-DC92 EOS and GERG-2004 EOS for SNG 5 are presented in figures 58 and 59 respectively. Since 1992, AGA8-DC92 has been the industry standard EOS for custody transfer purposes in the natural gas pipeline transportation industry. It was declared an international standard as has been reported by Span [63]. AGA8-DC92 has four different temperature and pressure ranges. Table 14 contains the expected accuracies for AGA8-DC92 predictions. Data lying within region 1 should be better than 0.1%, region 2 better than 0.3 %, region 3 better than 0.5 % and region 4 better than 1%. On the other hand, AGA8-DC92 has two different mixture characteristics depending upon the content of the natural gas mixture mol percentages. These characteristics are given in table 15.

TABLE 14  
American Gas Association (1992) data regions.

Data Region	Min. T [K]	Max. T [K]	Min. P [MPa]	Max. P [MPa]
1	265	335	0	12.00
2	211	394	12.00	17.00
3	144	477	17.00	70.00
4	144	477	70.00	140.00

On the other hand, GERG-2004 can reproduce experimental liquid saturated densities to within  $\pm 0.2\%$  while the widely used Peng-Robinson EOS can deviate by more than 10% for liquefied natural gas like mixtures. Moreover, gas densities for gas mixtures including ethane (up to 20%), propane (up to 14%), butane (up to 6%) and methane (balance) were also calculated using GERG-2004. Up to 30 MPa and between temperatures of 310 K to 360 K, GERG-2004 predictions are within  $\pm 0.1\%$  to  $\pm 0.2\%$  compared to the experimental data.

In addition, GERG-2004 accurately describes natural gas mixtures containing a high fraction of hydrogen. The equation is accurate within  $\pm 0.1\%$  between 270 K to 350 K and up to 30 MPa for mixtures containing 10% hydrogen or for methane-hydrogen binary mixtures containing up to 75% hydrogen. The total number of experimental points and their corresponding AGA8-DC92 regions for SNG 3 and SNG 5 mixtures are given in table 16.

TABLE 15

Ranges of gas mixture characteristics for AGA8-DC92 EOS.

Components	Compositions [% mol]	
	Normal Range	Expanded Range
N <sub>2</sub>	0 – 50	0 – 100
CO <sub>2</sub>	0 – 30	0 – 100
CH <sub>4</sub>	45 – 100	0 – 100
C <sub>2</sub> H <sub>6</sub>	0 – 10	0 – 100
C <sub>3</sub> H <sub>8</sub>	0 – 4	0 – 12
C <sub>4</sub>	0 – 1	0 – 6
C <sub>5</sub>	0 – 0.3	0 – 4
C <sub>6+</sub>	0 – 0.2	0 – dew point

TABLE 16

Total number of experimental points and their corresponding AGA8-DC92 EOS regions for SNG 3 and SNG 5 mixtures.

Isotherm	AGA8-DC92 [Region 2]		AGA8-DC92 [Region 3]		AGA8-DC92 [Region 4]	
	SNG 3	SNG 5	SNG 3	SNG 5	SNG 3	SNG 5
	250 K	1	1	2	2	3
350 K	1	1	2	2	3	3
450 K	-	-	3	3	3	3

Detailed results and further conclusions on SNG 3 and SNG 5 experimental results are discussed in following section.

### 5.3.2 SNG 4 and SNG 6 Measurements

As a continuation upon the work of Ejaz, we have studied two more synthetic natural gas mixtures, SNG 4 and SNG 6. Mixture compositions and mol percentages of the components are given in tables 17 and 18. When all 4 SNG components and compositions are compared, we realize systematic alternation of propane, butane fractions. Yet, in SNG 6 we have removed the CO<sub>2</sub> and N<sub>2</sub> fractions. Such systematic studies on alternating fractions are extremely important for developing an accurate database for a new equation of state.

TABLE 17

SNG 4 mixture compositions.

<b>Component</b>	<b>Mol %</b>	<b>Component</b>	<b>Mol %</b>
Methane	0.8999	Isopentane	0.0015
Ethane	0.0315	n-Pentane	0.0015
Propane	0.01583	Nitrogen	0.01699
Isobutane	0.00781	Carbon dioxide	0.01707
n-Butane	0.0079		

TABLE 18

SNG 6 mixture compositions.

<b>Component</b>	<b>Mol %</b>	<b>Component</b>	<b>Mol %</b>
Methane	0.90001	n-Butane	0.01151
Ethane	0.04565	Isopentane	0.00450
Propane	0.02243	n-Pentane	0.00450
Isobutane	0.01140		



TABLE 19

SNG 4 experimental P- $\rho$ -T data (after correction term).

**Synthetic Natural Gas Mixture 4 (SNG-4)**  
December, 2006

Temperature		Pressure		Balance		Density			Relative Deviation	
Average [K]	St. Dev [mK]	Average [Mpa]	St. Dev [Mpa]	St. Dev [mg]	Exp. [kg/m3]	AGA8-DC92 [kg/m3]	GERG-2004 [kg/m3]	AGA8-DC92 [%]	GERG-2004 [%]	GERG-2004 [%]
250.020	4.343	20.023	0.078	0.029	270.977	272.368	270.780	-0.492		0.092
250.028	2.875	29.950	0.053	0.051	314.673	315.705	314.050	-0.308		0.217
250.026	3.405	49.915	0.381	0.059	360.131	360.494	359.250	-0.082		0.264
250.003	8.244	75.019	0.976	0.050	393.215	393.242	392.580	0.012		0.181
250.032	4.899	100.046	0.233	0.017	416.754	416.000	415.810	0.200		0.246
250.038	2.623	125.013	0.181	0.023	434.273	433.751	433.940	0.139		0.096
250.068	4.840	149.917	0.603	0.014	449.834	448.401	448.930	0.339		0.220
350.002	2.9153	9.941	0.016	0.015	69.496	69.548	69.519	-0.052		-0.011
349.999	8.1073	29.912	0.054	0.055	198.587	198.493	198.370	0.070		0.132
349.997	2.6835	49.954	0.046	0.018	268.642	268.592	268.270	0.041		0.161
349.983	2.2806	74.917	0.475	0.044	318.064	317.993	317.630	0.044		0.159
350.009	2.5595	99.972	0.845	0.026	350.653	350.590	350.250	0.040		0.137
349.996	2.7661	125.109	0.139	0.027	375.197	375.026	374.730	0.068		0.147
349.990	4.6723	149.891	0.435	0.058	394.544	394.301	394.100	0.084		0.135
350.029	2.5475	155.022	0.726	0.030	398.114	397.858	397.660	0.087		0.136
450.038	10.751	9.966	0.017	0.025	49.785	49.975	49.957	-0.360		-0.324
450.045	0.076	29.976	0.076	0.029	141.524	141.547	141.520	0.004		0.023
450.043	12.984	49.975	0.138	0.021	206.987	206.811	206.790	0.105		0.116
450.059	6.4558	68.914	0.180	0.018	249.890	249.821	249.700	0.048		0.096
450.054	13.08	86.155	0.211	0.045	279.287	279.220	279.050	0.044		0.105
450.027	16.88	114.952	0.194	0.043	316.172	316.101	315.970	0.043		0.084
450.013	7.0139	137.492	0.231	0.045	338.514	338.394	338.340	0.056		0.072

Experimental P- $\rho$ -T data for SNG 4 are given in table 19. Deviations from AGA8-DC92 EOS and GERG-2004 EOS for SNG 4 are presented in figures 60 and 61 respectively. Experimental results for SNG6 are given in table 6.

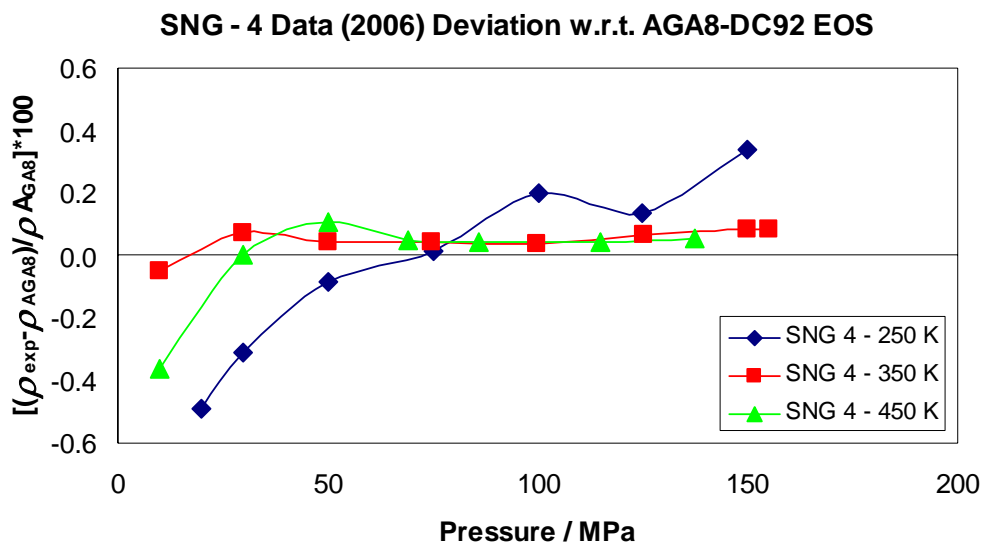


FIGURE 60. Density deviations for SNG 4 from AGA8-DC92 EOS.

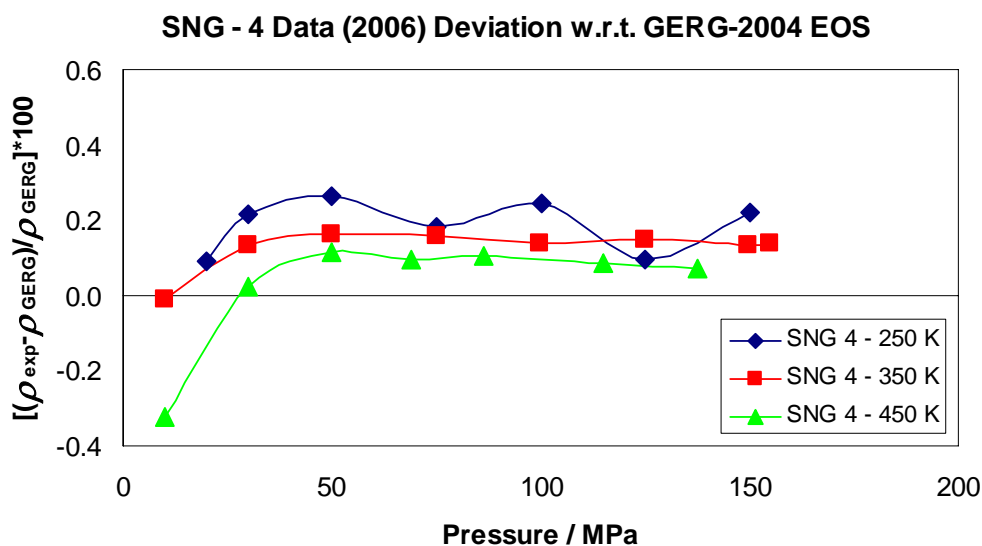


FIGURE 61. Density deviations for SNG 4 from GERG-2004 EOS.

TABLE 20

SNG 6 experimental P- $\rho$ -T data (after correction term).

## Synthetic Natural Gas Mixture 6 (SNG-6)

August - November 2006

Temperature		Pressure		Balance		Density			Relative Deviation	
Average [K]	St. Dev [mK]	Average [Mpa]	St. Dev [Mpa]	St. Dev [mg]	Exp. [kg/m <sup>3</sup> ]	AGA8-DC92 [kg/m <sup>3</sup> ]	GERG-2004 [kg/m <sup>3</sup> ]	AGA8-DC92 [%]	GERG-2004 [%]	
249.983	10.606	20.028	0.750	0.067	282.449	283.222	281.940	-0.254	0.200	
249.987	2.310	30.030	0.036	0.012	321.509	321.769	320.220	-0.062	0.422	
249.997	3.999	49.946	0.348	0.027	362.863	362.232	361.150	0.193	0.493	
249.977	8.045	74.931	0.321	0.016	393.862	392.451	392.030	0.379	0.487	
249.999	4.141	100.291	0.806	0.059	416.017	414.059	414.170	0.492	0.465	
249.918	5.584	124.967	0.268	0.080	432.480	430.647	431.190	0.445	0.318	
249.988	2.144	149.990	0.477	0.075	446.730	445.398	445.490	0.318	0.297	
350.026	12.202	9.998	0.011	0.019	72.452	72.636	72.599	-0.229	-0.179	
350.019	4.058	29.984	0.144	0.019	205.214	205.483	205.150	-0.108	0.055	
350.013	4.479	49.890	0.583	0.043	272.889	273.020	272.280	-0.024	0.247	
349.993	3.363	74.991	0.103	0.027	320.430	320.498	319.600	0.002	0.283	
350.000	3.544	99.925	0.214	0.023	351.424	351.462	350.530	0.012	0.278	
350.018	4.883	124.942	0.101	0.019	374.602	374.711	373.790	-0.006	0.241	
349.944	5.138	149.787	0.086	0.033	393.415	393.253	392.410	0.064	0.279	
450.043	15.311	9.999	0.012	0.026	51.259	51.431	51.415	-0.311	-0.280	
450.050	13.453	30.001	0.091	0.029	145.276	145.401	145.360	-0.061	-0.033	
450.057	9.292	49.945	0.054	0.024	210.802	210.596	210.430	0.122	0.201	
450.062	12.822	68.926	0.078	0.070	253.261	252.947	252.560	0.149	0.302	
450.027	13.661	99.965	0.315	0.037	300.500	300.130	299.590	0.148	0.328	
450.084	9.417	124.928	0.399	0.023	327.750	327.302	326.760	0.162	0.328	
450.051	11.064	149.926	0.356	0.022	349.557	349.023	348.580	0.178	0.305	

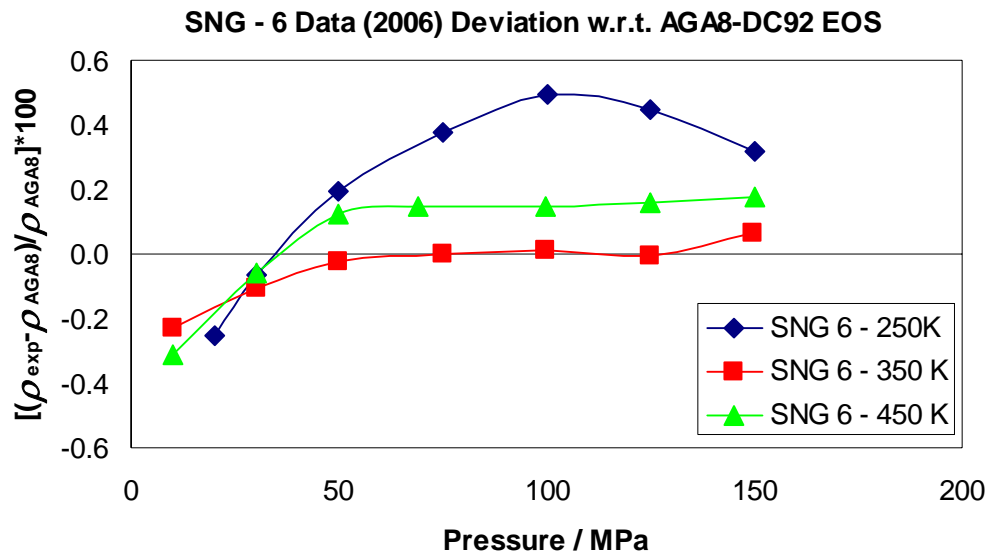


FIGURE 62. Density deviations for SNG 6 from AGA8-DC92 EOS.

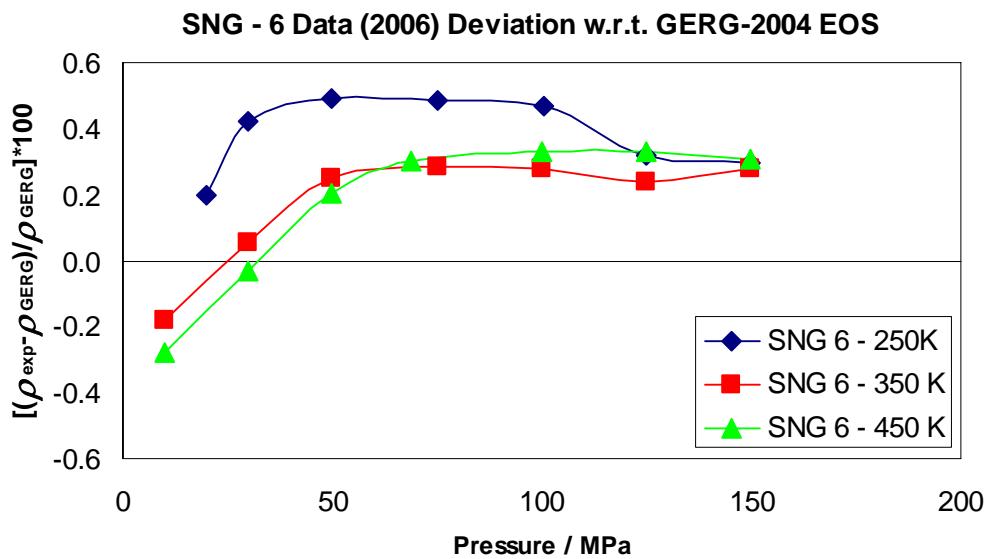


FIGURE 63. Deviations for SNG 6 from GERG-2004 EOS.

Deviations from AGA8-DC92 EOS and GERG-2004 EOS for SNG 6 are presented in figures 62 and 63 respectively. Total number of experimental points and their corresponding AGA8-DC92 EOS regions for SNG 4 and SNG 6 mixtures are given in table 21.

TABLE 21

Total number of experimental points and their corresponding AGA8-DC92 EOS regions for SNG 4 and SNG 6 mixtures.

Isotherm	AGA8-DC92 [Region 2]		AGA8-DC92 [Region 3]		AGA8-DC92 [Region 4]	
	SNG 4	SNG 6	SNG 4	SNG 6	SNG 4	SNG 6
	250 K	1	-	2	3	4
350 K	1	1	2	2	5	4
450 K	-	-	3	4	3	4

#### 5.4 Synthetic Natural Gas Phase Envelope Measurements

In 2005, Aparicio-Martinez used an isochoric apparatus located in the Thermodynamics Research Laboratory in Texas A&M University to measure phase envelopes for SNG mixtures. Details of the isochoric apparatus are given by Zhou [21].

Experimental results and predictions from Peng-Robinson (PR) are presented in figure 64. Experimental phase envelope points for SNG mixtures are given in table 22. As seen in figure 64, for SNG 5 and SNG 6, there is a dramatic difference in cricondentherm and cricondenbar between experimental results and EOS predictions. For SNG 3, PR EOS slightly over-predicts some phase loop points. Conversely, for SNG 4, PR EOS slightly under-predicts some loop points. However, for both SNG 3 and SNG 4 mixtures, the experimental cricondentherm and cricondenbar are not dramatically different from PR EOS predictions.

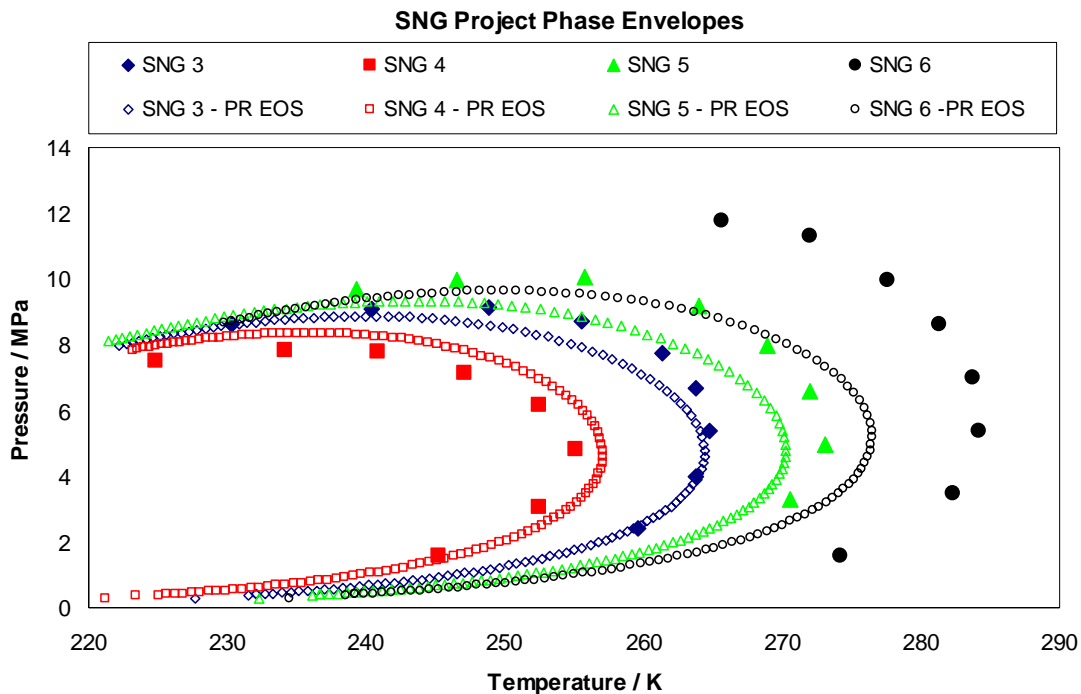


FIGURE 64. Experimental phase envelope points and PR EOS predictions for SNG mixtures.

TABLE 22

SNG mixtures experimental phase envelope data.

Phase Envelope Data Points							
SNG-3		SNG-4		SNG-5		SNG-6	
T / K	P / MPa	T / K	P / MPa	T / K	P / MPa	T / K	P / MPa
230.270	8.621	224.810	7.512	239.310	9.681	265.600	11.762
240.360	9.105	234.140	7.841	246.530	9.964	272.000	11.315
248.890	9.134	240.850	7.778	255.800	10.039	277.610	9.947
255.540	8.710	247.150	7.161	264.020	9.156	281.370	8.607
261.350	7.736	252.470	6.159	268.880	7.959	283.760	6.990
263.730	6.682	255.150	4.832	272.040	6.568	284.140	5.384
264.790	5.374	252.440	3.053	273.150	4.958	282.330	3.488
263.830	3.975	245.280	1.572	270.600	3.303	274.230	1.593
259.620	2.393						

### **5.5 Comments on SNG Mixture Experiments**

Measurements for SNG mixtures fall in the AGA8-DC92 regions 2, 3 and 4. For SNG 3 and SNG 5, 18 points are measured. Of the 18 points, only one point at 250 K and 10 MPa (region 2) falls out of the defined uncertainty. The rest of the AGA8-DC92 predictions and comparisons to experimental data obey the defined uncertainties. Compared to AGA8-DC92, GERG-2004 does a better job in predicting low pressure points.

We have measured 21 points for SNG 4. At low pressure (10 MPa) GERG-2004 performs better than AGA8-DC92. Additionally, at 250 K and 150 MPa GERG-2004 shows less deviation than AGA8-DC92. For rest of the points, AGA8-DC92 appears to be superior to GERG-2004.

We measured 22 points for SNG 6. GERG-2004 is shows better performance at 350 K - 10 MPa, 450 K - 10 MPa, 250 K - 20 MPa, 250 K - 100, 125, 150 MPa. For the rest of the points, AGA8-DC92 appears superior to GERG-2004.

### **5.6 Natural Gas Mixtures Including Heavy Components**

As a part of this work, we also determined thermodynamics properties for some mixtures including heavy components such as hexane, heptane, octane, nonane and some cyclic aromatics as well. We measured samples that are typical in the Gulf of Mexico. We measured densities of mixtures between 270 K and 340 K up to 35 MPa. Because of a confidentiality agreement, these data do not appear in the dissertation.

## 6. CONCLUSIONS AND RECOMMENDATIONS

### 6.1 Conclusions

Following conclusions can be drawn from this work.

1. An experimental setup for gas density measurements based upon a magnetic suspension technique covering the temperature range of 193 K to 523 K with the pressure range of 0 to 200 MPa has been used. The apparatus was originally manufactured by Rubotherm Präzisionsmesstechnik. All the data acquisition systems for temperature, pressure and weight measurements have been built and required programming for such systems has been programmed in LabVIEW®. For low temperature operations, we constructed a new liquid propane cooling system because stable operation is hard to achieve at low temperatures using the traditional liquid nitrogen method.
2. Pressure transducers are calibrated against Ruska Deadweight Gauges and PRT calibration is checked with a triple point of water cell.
3. Calibration of the apparatus is checked by measuring densities for pure nitrogen before and after measuring the Gulf of Mexico samples. Performance of the overall system is improved and fine-tuned during pure components measurements.
4. Pure methane, carbon dioxide and nitrogen were measured at pressures up to 200 MPa at temperatures between 250 K and 350 K. Pure component data are compared with NIST-12. In most cases, we achieved  $\pm 0.05$  to 0.1 % deviation from NIST-12 in gas density measurements for pure components. This shows the reliability of our data.
5. Operations at 200 MPa are the highest pressure operations that have been achieved with an MSD apparatus. Fortunately, we were able to maintain stable operations at the limits of the MSD.
6. Based upon pure component measurements, we determined the temperature and pressure dependency of the FTE correction term. We derived the required



correction term, which must be applied to raw density measurements obtained from our single sinker MSD.

7. We measured densities of four synthetic natural gas mixtures, SNG 3, SNG 4, SNG 5 and SNG 6, at three different isotherms (250 K, 350 K and 450 K) between 10 MPa and 150 MPa. We targeted reservoir conditions by going up to extreme temperatures and pressures and constructed an accurate P- $\rho$ -T database that can be used to validate a new equation of state.
8. All four mixtures fall in the normal range of compositions determined by American Gas Association [16]. Our measurements were in the 2<sup>nd</sup>, 3<sup>rd</sup> and 4<sup>th</sup> uncertainty regions for AGA8-DC92 as shown in figure 5. Most of the results were within the expected uncertainties except for low temperature and low pressure points.
9. We also tested the performance of the GERG-2004 developed by a group of European and American Researchers and presented by Kunz [78]. This EOS is expected to be a new reference EOS for custody transfer of natural gas. We have observed that for many points, AGA8-DC92 performs better than GERG-2004. We have used the REFPROP program for GERG-2004 calculations, which is obtained from NIST in Boulder. We conclude that more natural gas mixtures must be measured and tested against GERG-2004 before validating it as a new reference equation because its performance is questionable.
10. We performed a total uncertainty analysis for our density measurements. We included uncertainties from temperature and pressure measurements as well as uncertainty from compositions. The total uncertainty of our gas density measurements is estimated to be 0.11% mostly caused by uncertainty from the mixture composition.

## 6.2 Recommendations

Following recommendations can be given after completion of this work.

1. Because the final objective of this work is to construct a high accuracy P- $\rho$ -T database, more data for several different natural gas samples must be collected. Because of the uncertainty associated with AGA8-DC92, more high accuracy data are necessary to calculate equation parameters, perform modifications and even to suggest replacement of the equation with a new EOS. For this reason measurements for both normal and expanded range natural gas mixtures must be done in all temperature and pressure ranges including low pressures.
2. More pure component densities should be measured for a complete investigation of the FTE. With this work, we showed that the fluid specific apparatus constant appears to be a function of pressure and temperature. However, we validated the functional equation based upon nitrogen and carbon dioxide measurements. Extensive density measurements for air, oxygen, methane and other gases should be done.
3. Additionally, the FTE investigation should be checked with additional sinkers. As McLinden has discussed [53], for single sinker densimeters measurements of pure components with two different sinkers having different volume but same mass is crucial for determining FTE for a single sinker MSD. For this purpose, a second sinker made of copper must be made. Following volume and mass calibration of the new sinker, all the pure component data produced previously in the content of this work should be repeated for final FTE determination.
4. We have noticed that dropping from high pressures to low pressures with large pressure increments affects the time required for temperature and pressure to reach to equilibrium. It is recommended that the MSD operator decrease pressure with small pressure increments so that equilibrium is reached quickly in the system. These intervals could be 5 MPa intervals for pressures above 20 MPa and 2 or 3 MPa for pressures lower than 20 MPa. By doing so, more

experimental points can be collected within same amount of time required when large pressure increments are applied.

5. More low pressure data should be collected below 10 MPa and compared to two sinker densimeter results to calibrate the single sinker MSD at low pressures. Because our single sinker densimeter is not designed for low pressure operations, low pressure calibration against a two sinker densimeter is necessary for wide range of data collection. This may also give us some idea about the FTE at low pressures.
6. When isochoric densities are needed, collection by MSD and isochoric apparatus operating in tandem is discussed in [28]. Isotherms should be selected such that an intersection with an isochoric line occurs because isochoric densities are obtained at the intersections.
7. As mentioned in Appendix F, most of the uncertainty for our density measurements comes from the uncertainty in the compositions. Compositions of the gas samples should be analyzed using a proper instrumental method before and after the measurements. Also, a mixture apparatus available in the laboratory could be used to produce gas mixtures.
8. Full automation of the MSD can be achieved by installing solenoid valves at the required sections of the manifold. These solenoid valves can be operated by transistor logic remotely.
9. A high pressure DPI should be constructed and put to use instead of the ruptured Ruska DPI. The new DPI can be used along with a Ruska deadweight gauge.

## REFERENCES

- [1] J.M. Smith, H.C.V. Ness and M. Abbott, Introduction to Chemical Engineering Thermodynamics, seventh ed., McGraw Hill, New York, 2004.
- [2] Exxon Mobil, Tomorrow's Energy: A Perspective on Energy Trends, Greenhouse Gas Emissions and Future Energy Options, Irving, TX, 2006. Available from: [http://www.exxonmobil.com/.../tomorrows\\_energy.pdf](http://www.exxonmobil.com/.../tomorrows_energy.pdf)
- [3] Energy Information Administration, Office of Energy Markets and End Use, US Department of Energy Publication, Vol. No. DOE/EIA-0384, 2005.
- [4] Worldwide Look at Reserves and Production, Oil & Gas Journal 103 (2005) 24-25.
- [5] BP Statistical Review of World Energy, London, 2005. Available from: [http://www.bp.com/.../STAGING/local\\_assets/downloads/pdf/statistical\\_review\\_of\\_world\\_energy\\_full\\_report\\_2005.pdf](http://www.bp.com/.../STAGING/local_assets/downloads/pdf/statistical_review_of_world_energy_full_report_2005.pdf)
- [6] International Energy Outlook Report, DOE/EIA-0484 (2006).
- [7] R.D. Baud, R.H. Peterson, G.E. Richardson, L.S. French, J. Regg, T. Montgomery, T.S. Williams, C. Doyle and M. Dorner., in: Department of the Interior Publication, Vol. OCS Report MMS 2002-021, US Department of the Interior, Anchorage, 2002.
- [8] A.B. Derman and G. Jacobson, Oil & Gas Journal 98 (19) (2000) 24.
- [9] A.B. Derman and D. Johnston, Oil & Gas Journal 98 (37) (2000) 50.
- [10] G. Moritis, Oil & Gas Journal 101 (44) (2003) 54.
- [11] S.R. Sauer and J. Wiseman, Offshore Technology Conference, Houston, 2006.
- [12] G. Clouser, Oil and Gas investor, Deepwater Investment Supplement 22 (8) (2002) 16.
- [13] M. Atilhan, S. Ejaz, S. Aparicio-Martinez and K.R. Hall, Sixteenth Symposium on Thermophysical Properties, Boulder, 2006.
- [14] X. Wang and J.G. Bomba, Proceedings of the 13th International Conference on Offshore Mechanics and Arctic Engineering, Houston, 2006.
- [15] W. Wagner and R. Kleinrahm, Metrologia 41 (2004) S24-S39.

- [16] American Gas Association, Compressibility Factors of Natural Gas and Other Related Hydrocarbon Gases, Washington DC, 1992.
- [17] AGA8-DC92 EOS uncertainty ranges based on pressure and temperature, <http://www.4uengineer.com/topic/FlowMeter/AGA8.gif>, 2007.
- [18] J.T.R. Watson and B. Millington, Project No DRG001, Report No 110/97, National Engineering Laboratory, (1998).
- [19] Personal Communication to K.R. Hall, Texas A&M University, College Station 2002-2007.
- [20] M. Atilhan, Master Thesis, Texas A&M University, College Station, 2004.
- [21] J. Zhou, Ph.D. Dissertation, Texas A&M University, College Station, 2005.
- [22] P.V. Patil, Ph.D. Dissertation Texas A&M University, College Station, 2005.
- [23] R. Klimeck, O. Kunz and W. Wagner, Gas - und Wasserfach. Gas – Erdgas, 144 (7) (2003) 430-435.
- [24] N. Kuramoto, K. Fujii and A. Waseda, Metrologia 41 (2004) S84-S94.
- [25] R. Kleinrahm and W. Wagner, Progress Reports of the VDI Journals, 3 (1984) 92.
- [26] V. Majer, A.A.H. Pauda, in: A.R.H. Goodwin, K.N.Marsh and W.A. Wakeham. (Eds.), Measurement of the Thermodynamic Properties of Single Phases, Vol. VI, Elsevier, Amsterdam, 2003.
- [27] J.L. Daridon, A. Lagrabette and B. Lagourette, J. Chem. Thermodyn. 30 (1998) 607-623.
- [28] J.J. Zhou, P. Patil, S. Ejaz, M. Atilhan, J.C. Holste and K.R. Hall, J. Chem. Thermodyn. 38 (2006) 1489-1494.
- [29] V. Majer and A.A.H. Padua. in: Goodwin, A.R.H. Goodwin, K.N. Marsh and W.A. Wakeham, ed. (Eds.), Measurement of the Thermodynamic Properties of Single Phases, Experimental Thermodynamics, Amsterdam, 2003.
- [30] A.A.H. Padua, J.M.N.A. Fareleira, J.C.G. Calado and W.A. Wakeham, Rev. Sci. Instrum. 69 (1998) 2392-2399.
- [31] E.S. Burnett, Journal of Applied Mechanics, 3 (1936) A-136.

- [32] W. Wagner, K. Brachthäuser, R. Kleinrahm and H.W. Losch, *Int. J. Thermophys.* 16 (1995) 399.
- [33] R. Tillner-Roth and H.D. Baehr, *J. Chem. Thermodyn.* 24 (1992) 413-424.
- [34] P.T. Eubank, L.L. Joffrion, M.R. Patel and W. Warowny, *J. Chem. Thermodyn.* 20 (1988) 1009-1034.
- [35] W.R. Lau, C.A. Hwang, H.B. Brugge, G.A. Iglesias-Silva, H.A. Duarte-Garza, W.J. Rogers, K.R. Hall, J.C. Holste, B.E. Gammon and K.N. Marsh, *J. Chem. Eng. Data* 42 (1997) 738-744.
- [36] R. Kleinrahm and W. Wagner, *J. Chem. Thermodyn.* 18 (1986) 739-760.
- [37] H.W. Lösch, *Development and Design of New Magnetic Suspension Balances for Non-Contact Measurements of Vertical Forces*, Dusseldorf, 1987.
- [38] W. Wagner, R. Kleinrahm, H.W. Lösch and J.T.R. Watson, in: A.R.H. Goodwin, K.N. Marsh and W.A. Wakeham. (Eds.), *Measurement of the Thermodynamic Properties of Single Phases*, Vol. VI, Elsevier, Amsterdam, 2003.
- [39] J. Klimeck, R. Kleinrahm and W. Wagner, *J. Chem. Thermodyn.* 30 (1998) 1571-1588.
- [40] R. Kleinrahm, W. Wagner and M.O. McLinden, *Int. J. Thermophys.* (in press). 2007.
- [41] J.W. Beams and A.M. Clarke, *Rev. Sci. Instrum.* 33 (1962) 750-753.
- [42] K. Brachthäuser, R. Kleinrahm, H.W. Losch and W. Wagner, *Entwicklung eines neuen Dichtemessverfahrens und Aufbau einer Hochtemperatur-Hochdruck-Dichtemessanlage*, Dusseldorf, 1993.
- [43] Two sinker magnetic suspension densimeter apparatus scheme, [http://www.ruhr-uni-bochum.de/thermo/Forschung/Seiten/Dmas/zsk\\_dma-eng.htm](http://www.ruhr-uni-bochum.de/thermo/Forschung/Seiten/Dmas/zsk_dma-eng.htm) 2007.
- [44] S. Ejaz, Ph.D. Dissertation, Texas A&M University, College Station, 2007.
- [45] W. Blanke, G. Klingenberg and R. Weiss, *Int. J. Thermophys.* 16 (1995) 1143-1153.
- [46] W. Blanke, G. Klingenberg and R. Weiss, *J. Chem. Eng. Data*, 41 (1996) 576-580.

- [47] J.R.T. Watson and B. Millington, East Kilbride National Engineering Lab, The Density of Rich Natural Gas Mixtures. A joint Industrial Project, Project No DRG001, Report No 110/97, East Kilbride, Glasgow, 1998.
- [48] K. Iwagai, T. Masuda, H. Sato and K. Watanabe, Proceedings of 20th Japan Symposium on Thermophysical Properties, Japan Society of Thermophysical Properties, Tokyo, Japan, 1999.
- [49] N. Kuramoto and K. Fujii, Proceedings of 22nd Japan Symposium on Thermophysical Properties, Japan Society of Thermophysical Properties, Sendai, Japan, 2001.
- [50] M. Kinoshita and K. Fujii, Proceedings of 22th Japan Symposium on Thermophysical Properties, Japan Society of Thermophysical Properties, Tokyo, Japan, 2001.
- [51] M.A. Villamañán and C.R. Chamorro, Thermodynamics Conference on Thermodynamics and Statistical Mechanics with Industrial Applications, School of Chemistry, University of Bristol, Bristol, 2001.
- [52] B. Saleh and M. Wendland, 15th Symposium on Thermophysical Properties, Boulder, CO, 2003.
- [53] Personal communication to M.O. McLinden and W. Wagner, NIST, Boulder, 2006.
- [54] M.O. McLinden and C. Losch-Will, *J. Chem. Thermodyn.* 39 (2007) 507-530.
- [55] Ruska Instrument Corporation, Deadweight Gauge Operating Manual, Houston, 1977.
- [56] Rubotherm GmbH, Operating Instructions – Densimeter with Magnetic Suspension Balance, Bochum, Germany, 1999.
- [57] H. Preston-Thomas, *Metrologia* 27, (1990), 3.
- [58] Minco, Report of Calibration for Platinum Resistance Thermometer Model S1059-2, Serial Number 204, Report number 3385, Friedley, MN, 2000.
- [59] R.N. Bateson, Introduction to Control System Technology, sixth ed., Prentice-Hall, Upper Saddle River, NJ, 1999.

- [60] H.A. Bowman, R.M. Schoonover and C.L. Carroll, *J. Res. NBS* 78A (1973)13-40.
- [61] H.A. Bowman, R.M. Schoonover and C.L. Carroll, *Metrologia* 10 (1974) 117-121.
- [62] Personal Communication to M.O. McLinden, Boulder, 2007.
- [63] R. Span, E.W. Lemmon, R.T. Jacobsen, W. Wagner and A. Yokozeki, *J. Phys. Chem. Ref. Data* 29 (2000) 1361-1433.
- [64] U. Setzmann and W. Wagner, *J. Phys. Chem. Ref. Data* 20 (1991) 1061-1155.
- [65] R. Span and W. Wagner, *J. Phys. Chem. Ref. Data* 25 (1996) 1509-1596.
- [66] R.T. Jacobsen, R.B. Stewart and M. Jahangiri, *J. Phys. Chem. Ref. Data* 15 (1986) 735-909.
- [67] P. Nowak, R. Kleinrahm and W. Wagner, *J. Chem. Thermodyn.* 29 (1997) 1137-1156.
- [68] N. Pieperbeck, R. Kleinrahm, W. Wagner and M. Jaeschke, *J. Chem. Thermodyn.* 23 (1991) 175-194.
- [69] W. Duschek, R. Kleinrahm, W. Wagner and M. Jaeschke, *J. Chem. Thermodyn.* 20 (1988) 1069-1077.
- [70] J.H.W. Schamp, E.A. Mason, A.C.B. Richardson and A. Altman, *Physics of Fluids*, 1 (1958) 329-337.
- [71] N.J. Trappeniers, T. Wassenaar and J.C. Abels, *Physica* 98A (1979) 289-297.
- [72] D.R. Douslin, R.H. Harrison, R.T. Moore and J.P. McCullough, *J. Chem. Eng. Data* 9 (1964).
- [73] G. Handel, R. Kleinrahm and W. Wagner, *J. Chem. Thermodyn.* 24 (1992) 685-695.
- [74] T.K. Bose, J.M. St-Arnaud, H.J. Achtermann and R. Scharf, *Rev. of Sci. Instrum.* 57 (1986) 26-32.
- [75] H.J. Achtermann, T.K. Bose, H. Rögner and J.M. St-Arnaud, *Int. J. Thermophys.* 7 (3) (1986) 709-720.



- [76] J. Klimeck, R. Kleinrahm and W. Wagner, *J. Chem. Thermodyn.* 33 (2001) 251-267.
- [77] Personal Communication to S. Aparicio-Martinez, Texas A&M University, College Station, 2006.
- [78] O. Kunz, W. Wagner and M. Jaeschke, *Sixteenth Symposium on Thermophysical Properties*, Boulder, 2006.

## APPENDIX A

### FORCE TRANSMISSION ERROR ANALYSIS FOR TWO SINKER MAGNETIC SUSPENSION DENSIMETERS

McLinden et. al. [53] made a detailed analysis of the effect of FTE for the recently developed two sinker MSD [54] at NIST Boulder. This two sinker densimeter has been designed such that density determination is done by eight weighings in a symmetrical weighing design. The order is given by McLinden et. al. [53]:

- Tantalum (Ta) Sinkers, Titanium (Ti) Sinkers
- Calibration Weight
- Tare Weight (twice)
- Calibration Weight (again)
- Ti Sinkers, Ta Sinkers

The external weights are made of stainless steel. These weights have equal volumes to cancel the external air buoyancy force, but they have different masses. In measuring position 1, the first sinker is raised and weighs through the magnetic coupling between the permanent magnet and electromagnet using raising fork. At this point the forces on the balance for the weighing of sinker 1 are given as a sum of all the suspended parts:

$$W_1 = \alpha \left[ \phi \left( m_1 + m_{p-mag} - \rho_{fluid} (V_1 + V_{p-mag}) \right) + \left( m_{e-mag} - \rho_{air} V_{e-mag} \right) + W_{zero} \right] \quad (A.1)$$

where;

$\alpha$  = balance calibration factor

$\phi$  = coupling factor

$\rho_{fluid}$  = fluid density in pressure environment

$m_{p-mag}$  = mass of permanent magnet

$m_{e-mag}$  = mass of permanent magnet

$W_{zero}$  = balance reading when nothing else is on the balance pan or weighing hook

Subscript 1: sinker 1

The balance calibration factor drifts slowly with time as ambient temperature and pressure change. A coupling factor includes the apparatus magnetic effect as well as the fluid magnetic susceptibility and the relative position of the permanent magnet.

The electromagnet and the permanent magnet can be lumped together with the lifting fork because they are always weighed. On the other hand,  $W_{zero}$  is the same for each weighing. Therefore we can write;

$$\beta = \phi \{ m_{p-mag} - \rho_{fluid} V_{p-mag} \} + \{ m_{e-mag} - \rho_{air} V_{e-mag} \} + W_{zero} \quad (A.2)$$

After defining equation 10, we can simplify and re-write equation A.1 as:

$$W_1 = \alpha \left[ \phi \{ m_1 - \rho_{fluid} V_1 \} + \beta \right] \quad (A.3)$$

And similar to equation A.3, we can write the equation for a 2<sup>nd</sup> sinker  $W_{cal}$  and  $W_{tare}$  as follows:

$$W_2 = \alpha \left[ \phi \{ m_2 - \rho_{fluid} V_2 \} + \beta \right] \quad (A.4)$$

$$W_{cal} = \alpha \left[ m_{cal} - \rho_{air} V_{cal} + \beta \right] \quad (A.5)$$

$$W_{tare} = \alpha \left[ m_{tare} - \rho_{air} V_{tare} + \beta \right] \quad (A.6)$$

$W_1$  and  $W_2$  are the “ideal” balance readings when sinker 1 and 2 are weighed respectively.

Equations A.5 and A.6 are solved together to obtain  $\alpha$  and  $\beta$  values as:

$$\alpha = \frac{W_{cal} - W_{tare}}{(m_{cal} - m_{tare}) - \rho_{air} (V_{cal} - V_{tare})} \quad (A.7)$$

$$\beta = \frac{W_{cal}}{\alpha} - (m_{cal} - \rho_{air} V_{cal}) \quad (A.8)$$

By subtracting equation A.5 from equation A3, an intermediate expression for fluid density is;

$$\rho_{fluid} = \left[ (m_1 - m_2) - \frac{(W_1 - W_2)}{\alpha \phi} \right] / (V_1 - V_2) \quad (A.9)$$

If  $\alpha$  and  $\phi$  values are set to 1;

$$\phi = \frac{(W_1/\alpha) - \beta}{m_1 - \rho_{fluid}V_1} \quad (\text{A.10})$$

Finally, by substituting equation A.10, the fluid density is;

$$\rho_{fluid} = \left[ (m_1 - m_2) - \frac{(W_1 - W_2)m_1}{(W_1 - \alpha\beta)} \right] / \left[ (V_1 - V_2) - \frac{(W_1 - W_2)V_1}{(W_1 - \alpha\beta)} \right] \quad (\text{A.11})$$

The parameter  $\beta$  includes the buoyancy forces on the electromagnet, the permanent magnet and the zero shift of the balance  $W_{zero}$ ; it is a constant for density determination at a given point.  $\phi$  is the coupling factor that includes the apparatus magnetic effect as well as the fluid magnetic susceptibility.  $m_{cal}$  and  $m_{tare}$  are the masses of the external calibration weights and  $m_1$  and  $m_2$  are masses of sinker 1 and 2, and all these are measured in vacuum. When we take  $\alpha, \phi, \beta$  and buoyancy into account, we can say that  $W_1$  and  $W_2$  should be slightly different from actual balance readings. The effect of the FTE on density may be obtained by subtracting equation A.12 from itself when  $\phi$  is set as 1 and  $m_1 \approx m_2$  is assumed. Based upon these assumptions:

$$\frac{\Delta\rho}{\rho_{fluid}} \approx \phi - 1 \quad (\text{A.12})$$

Furthermore,  $\phi$  is proportional to the fluid density and the magnetic susceptibility of the fluid, and it is empirically [53]:

$$\phi = \phi_0 + \varepsilon_p \frac{\chi_s}{\chi_{s0}} \frac{\rho_{fluid}}{\rho_0} \quad (\text{A.13})$$

Both equations A.12 and A.13 are combined to give:

$$\frac{\Delta\rho}{\rho_{fluid}} = (\phi_0 - 1) + \varepsilon_p \frac{\chi_s}{\chi_{s0}} \frac{\rho_{fluid}}{\rho_0} \quad (\text{A.14})$$

After all the algebra described above, the balance factor  $\alpha$  is 1.00015 and the fluid specific effect is +0.0065% for air that is measured at 273 K and 35 MPa whereas the fluid specific effect is reported as +0.37% for pure oxygen with the NIST two sinker densimeter. Moreover, the apparatus portion of the FTE is reported as  $1.5 \cdot 10^{-6}$  or 15 ppm [53].

## APPENDIX B

### PRT CALIBRATION AND ITS-90 COEFFICIENTS

The International Temperature Scale (ITS-90) is designed to characterize the absolute thermodynamic scale in the range of 0.65 K to 1358 K. Thermodynamic equilibrium states of fourteen pure chemical elements and degassed water are used to determine reference temperature points in ITS-90 scale. These defined reference points are used to calibrate thermometers. Some formulas are used to interpolate between the reference points.

ITS-90 expresses the temperature in Kelvin in terms of the ratio of the measured resistance of the PRT at the temperature and its resistance at triple point of water; 273.16 K:

$$W(T) = \frac{R(T)}{R(273.16\text{K})} \quad (\text{B.1})$$

The deviation equation given by equation D.2 and reference function given by equation D.3 are used to calculate the temperature below 273.16 K.

$$W_{\text{ref}}(T) = W(T) - a_4[W(T) - 1] - b_4[W(T) - 1] \ln W(T) \quad (\text{B.2})$$

$$\frac{T}{273.16\text{K}} = B_0 + \sum_1^{15} B_i \left[ \frac{W_{\text{ref}}(T)^{1/6} - 0.65}{0.35} \right]^i \quad (\text{B.3})$$

The deviation equation given by equation B.4 and the reference function given by equation D.5 is used to calculate the temperature above 273.16 K.

$$W_{\text{ref}}(T) = W(T) - a_8[W(T) - 1] - b_8[W(T) - 1]^2 \quad (\text{B.4})$$

$$T - 273.15\text{K} = D_0 + \sum_1^9 D_i \left[ \frac{W_{\text{ref}}(T) - 2.64}{1.64} \right]^i \quad (\text{B.5})$$

The constants  $a_4$ ,  $b_4$ ,  $a_8$  and  $b_8$  were determined by Minco by calibrating the PRT at fixed temperature points defined by ITS-90. These constants and values of the constants  $B_i$  and  $D_i$  are given in Table B.1. The resistance of the PRT at the triple point of water measured during the original calibration done by Minco was  $R(273.16\text{K}) = 100.4244 \Omega$ .

TABLE B.1

Constants in Deviation Equations and Reference Functions of ITS-90.

$a_4$	-0.000418264140	$B_0$	0.183324722
$b_4$	0.000080228227	$B_1$	0.240975303
$a_8$	-0.000568113400	$B_2$	0.209108771
$b_8$	0.000260761350	$B_3$	0.190439972
		$B_4$	0.142648498
		$B_5$	0.077993465
$D_0$	439.932854	$B_6$	0.012475611
$D_1$	472.418020	$B_7$	-0.032267127
$D_2$	37.6844940	$B_8$	-0.075291522
$D_3$	7.472018	$B_9$	-0.056470670
$D_4$	2.920828	$B_{10}$	0.076201285
$D_5$	0.005184	$B_{11}$	0.123893204
$D_6$	-0.963864	$B_{12}$	-0.029201193
$D_7$	-0.188732	$B_{13}$	-0.091173542
$D_8$	0.191203	$B_{14}$	0.001317696
$D_9$	0.049025	$B_{15}$	0.026025526

## APPENDIX C

### PRESSURE TRANSDUCER CALIBRATION CALCULATIONS

A Ruska Instrument Corporation Dead Weight Gauge (DWG model: 2450-701, serial number: 19851) that uses a Ruska oil and gas Differential Pressure Indicator (DPI - model: 2411.1, serial number: 8886), allows us to perform *in-situ* pressure transducer calibrations. In the DPI, oil is in the upper portion and gas is in the lower portion. The oil side is connected to the DWG, and the gas side is connected to the pressure transducer. The DWG has an operating range of 275.79 MPa, and the DPI has a pressure range of 103.42 MPa. We can read pressure differential as low as 0.275 kPa with the DPI electronic null indicator. A stainless steel 303, class 'S' weight set (model: 2450-707-00, serial number: 23353) manufactured by Ruska is used to balance the fluid pressure on the piston cylinder assembly.

The cross sectional area of the piston cylinder assembly at 296.15 K [73.4 °F, 23 °C],  $A_0$  and the mass of each weight of the weight set were calibrated in June 2003 and are traceable to NIST (Ruska Instruments Corporation, 2003). Atmospheric pressure is recorded from Paroscientific Barometer (model: 740-16B, serial number: 55782) during calibrations. The following corrections are applied to calibration parameters during pressure transducer calibration

- i.* The effect of gravity and air buoyancy force on the masses.
- ii.* Pressure head between the DWG reference plane of measurement and the DPI diaphragm.
- iii.* The taring components and oil surface tension effects as described by Ruska Instruments Corporation (1977).

Estimated total uncertainty in pressure transducer calibration caused by the DWG and DPI setup is  $\pm 0.005\%$ , and the total uncertainty of the Paroscientific pressure transducers are  $\pm 0.01\%$  of full scale for the 6,000 psi one and  $\pm 0.02\%$  for the 30,000 psi one.

The following corrections should be applied during pressure transducer calibrations:

1. Elastic distortion of the cylinder: The net change in the area of the piston/cylinder assembly at a constant temperature of 23 °C could be expressed as a polynomial function of the applied pressure:

$$A_e = A_{0(t=23)}(1 + b_1 p + b_2 p^2) \quad (C.1)$$

where,

$A_e$ : The effective area at a pressure P.

$A_{0(t=23)}$ : The area of the piston at a reference pressure of zero psig and at a reference temperature of 23 °C.

$b_1, b_2$ : Elastic distortion coefficients that are determined experimentally.

2. Effect of temperature: Dead-weight gages are temperature sensitive and should be corrected to a common temperature.

$$A_{0(t+\Delta t)} = A_{0(t=23)}(1 + C\Delta t) \quad (C.2)$$

where,

$A_{0(t+\Delta t)}$  : The area corrected to the working temperature

C: The coefficient of superficial expansion

3. Buoyant effect of the air: If X is the calibrated mass,  $M_X$  is the true mass in vacuum and  $(M_A)_X$  is the apparent mass in air because of buoyancy, then:

$$\begin{aligned} (M_A)_X &= M_X - V_X \rho_{air} \\ &= M_X (1 - \rho_{air} / \rho_X) \end{aligned} \quad (C.3)$$

where,

$V_X$ : Volume of the calibrated mass.

If  $\rho_{air}$  and  $\rho_x$  are the densities of air and calibrated mass, respectively,  $g_c$  is a conversion constant and  $F$  is the force due to apparent mass, then:

$$\begin{aligned} F &= (M_A)_X \frac{g}{g_c} \\ &= M_X (1 - \rho_{air} / \rho_X) \frac{g}{g_c} \end{aligned} \quad (C.4)$$



$(M_A)_{X \text{ wrt brass}}$ , apparent mass of X with respect to brass standards has been defined such that

$$F = (M_A)_{X \text{ wrt brass}} \left(1 - \rho_{air} / \rho_{brass}\right) \frac{g}{g_c} \quad (C.5)$$

where,

$\rho_{brass}$ : Density of the brass standards (approximately 8.4 g/cm<sup>3</sup>).

TABLE C.1

Parameter values from the calibration report of DWG.

Parameter	Value
$A_0$ (at 23 °C)	1.301632e-2 [in <sup>2</sup> ]
$b_1$	-1.54e-8 [psi <sup>-1</sup> ]
$b_2$	-1.35e-13 [psi <sup>-1</sup> ]
C	9.1e-6 [C <sup>-1</sup> ]
L1	6.141 [in]

TABLE C.2

Component weights from the calibration report of DWG.

Component	Apparent Mass [lbs]
Piston	0.0191751
Surface Tension	1.2e-4
Weight Tare	0.761864
Total Tare	0.781159

TABLE C.3  
Instruments used during pressure transducer calibration.

<b>Pressure Measurement for Magentic Suspension Densitometer</b>				
<b>Equipment</b>	<b>Manufacturer</b>	<b>Model</b>	<b>Serial Number</b>	<b>Range</b>
Quartz Crystalline Pressure Transducer	Paroscientific	46K-101	84267	6,000 psi
Differential Pressure Indicator (DPI) - Oil Gas System	Ruska Instrument	2411.1	8886	15,000 psi on either side
Dead Weight Gauge (DWG)	Ruska Instrument	2450-700-00	19851	40,000 psi
Dead Weight Gauge Weight Set (Standard 'S' Class)	Ruska Instrument	2450-707-0	23353	40,000 psi
Barometer	Paroscientific	740-16B	55782	11.5 - 16 psi
Hand Pump - Oil	Ruska Instrument	2427-801	23940	40,000 psi
Hand Pump - Gas	High Pressure Equipment	37-6-70	-	30,000 psi

TABLE C.4  
Corrections that are used during pressure transducer calibration.

<b>Factors Affecting Performance of the DWG and the Corresponding Corrections</b>					
Serial Number	Description	Unit	Quantity	Relation used	
<b>Temperature of the piston and cylinder</b>					
1	Reference temperature for piston cylinder (t)	°C	23	$A_{o,t+\Delta t} = A_{o,t=23} * (1+C*\Delta t)$	
	Area of piston at zero psig and reference temperature ( $A_{o,t}$ )	inch <sup>2</sup>	0.01301632		
	Coefficient of expansion of piston-cylinder material - tungsten carbide (C)	inch <sup>2</sup> /inch <sup>2</sup> /°C	9.1E-06		
	Difference between working and reference temperature ( $\Delta t$ )	°C	-		
	Area corrected to the working temperature ( $A_{o,t+\Delta t}$ )	inch <sup>2</sup>	-		
<b>Elastic distortions of the piston and cylinder</b>					
2	Coefficient of elastic distortion of piston cylinder assembly (B)	inch <sup>2</sup> /inch <sup>2</sup> /psi	-1.54E-08	$A_e = A_{o,t+\Delta t} * (1+B*p)$	
	Effective area of piston at working pressure (p) and temperature ( $A_e$ )	inch <sup>2</sup>	-		
<b>Effect of gravity on the masses</b>					
3	Mass of weights placed on the gauge piston (M)	lb <sub>m</sub>	-	$F = k * M * g_l$	
	Elevation of Room R1012	m	141.7		
	Local acceleration due to gravity (g <sub>l</sub> )	cm/s <sup>2</sup>	979.32668		
	Unit conversion factor (k)	-	1.01972E-03		
	Force acting on gauge piston (F)	lb <sub>f</sub>	-		
<b>Buoyant effect of air</b>					
4	Mass of load on gauge piston reported as 'apparent mass versus brass standards' ( $M_a$ )	lb <sub>m</sub>	-	$F = M_a * (1 - (\rho_{o_a} / \rho_{o_b})) * k * g_l$	
	Density of air ( $\rho_{o_a}$ )	g/cm <sup>3</sup>	0.0012		
	Density of brass ( $\rho_{o_b}$ )	g/cm <sup>3</sup>	8.4		
	Force acting on gauge piston (F)	lb <sub>f</sub>	-		

TABLE C.4 (con't)

<b>Factors Affecting Performance of the DWG and the Corresponding Corrections</b>					
Serial Number	Description	Unit	Quantity	Relation used	
<b>5</b>	<b>Pressure head between gauge reference plane of</b>				
	Specific gravity of Spinnestic 22 oil used in DWG (15.6 °C/ 15.6 °C)	-	0.86		
	Density of water at 15.6 °C	kg/m <sup>3</sup>	999.007		
	Density of Spinnestic 22 oil ( $\rho_{oil}$ )	kg/m <sup>3</sup>	859.146		
	Pressure conversion factor ( $k_p$ ) for 1psi	N/m <sup>2</sup>	6894.757		$h_{oil} = k_p / (\rho_{oil} * g)$
	Head of Spinnestic 22 oil equivalent to 1 psi pressure (h oil)	m	0.82		
<b>6</b>	Head of Spinnestic 22 oil between DWG reference plane of measurement and DPI diaphragm	inch	8.5		
	Pressure due to Spinnestic 22 oil head	psi	0.263		
	<b>Taring components and oil surface tension effects</b>				
	Apparent mass of piston assembly	lb <sub>m</sub>	0.0191751		
		g	8.70		
	Apparent mass of weight loading table	lb <sub>m</sub>	0.761864		
g		345.58			
Surface tension due to Spinnestic oil	lb <sub>m</sub>	0.00012			
	g	0.05			
Total taring component ( $M_{tare}$ )	lb <sub>m</sub>	0.7811591			
	g	354.33			
<b>7</b>	<b>Barometric pressure</b>				
	Barometric pressure to be added to DWG pressure for absolute pressure	psia	-		$p = P_{barometric} + P_{DWG}$

## APPENDIX D

### DIGITAL WEIGHING BALANCE CALIBRATION

We calibrated the Mettler Toledo digital weighing balance in July of 2005 using calibrated Ruska weights. Calibration weighing readings are given in table D.1.

TABLE D.1

Mettler Toledo balance calibration.

Ruska Weight Serial Number	Weight of External Ruska Weights	1 <sup>st</sup> Weighing	2 <sup>nd</sup> Weighing	3 <sup>rd</sup> Weighing
32	5.9084	5.90811	5.90816	5.90850
31	11.8134	11.81352	11.81351	11.81354
30	23.6351	23.63531	23.63531	23.63531
29	23.6275	23.62765	23.62775	23.62772
28	59.0550	59.005568	59.05568	59.05570
32+31	17.7218	17.72200	17.72210	17.72207
32+30	29.5435	29.54375	29.54383	29.54386
32+29	29.5359	29.63627	29.53617	29.56616
31+30	35.4485	35.44878	35.44882	35.44896
31+29	35.4409	35.44126	35.44127	35.44123
30+29	47.2626	47.226298	47.26302	47.262303
32+31+30	41.3569	41.35729	41.35735	41.35738
32+31+29	41.3493	41.34957	41.34970	41.34978
31+30+29	59.076	59.07665	59.07645	59.07667
32+30+29	53.171	53.17156	53.17159	53.17154

Measurements are taken at 21 °C, at ambient pressure of 14.5018 psi and with relative humidity of 50%. We also measured our calibrated sinker directly on the balance weighing pan. These measurements are given on table D.2.

TABLE D.2

Sinkers weighings on Mettler Toledo balance pan.

Reading #	Weight [g]	Zero Shift [g]	
		Beginning	End
1	30.38811	0.00000	-0.00001
2	30.38814	-0.00002	0.00007
3	30.38805	0.000000	0.00005
4	30.38792	0.00001	-0.00007
5	30.38796	-0.00001	-0.00006
6	30.38788	-0.00001	-0.00005
7	30.38801	0.00000	-0.00003
8	30.38809	0.00000	0.00006
9	30.38817	0.00000	0.00005
10	30.38814	0.00000	0.00004
11	30.38812	0.00000	0.00003
12	30.38808	0.00001	0.00000
13	30.38809	0.00000	-0.00004
14	30.38813	0.00002	0.00000
15	30.38814	0.00002	0.00001
16	30.38814	0.00001	0.00005
17	30.38818	0.00001	0.00007
18	30.38805	0.00000	-0.00001
19	30.38814	0.00000	-0.00003
20	30.38821	0.00001	0.00006
21	30.38818	0.00000	0.00002
22	30.38813	0.00002	0.00002
23	30.38815	0.00000	0.00004
24	30.38803	0.00000	-0.00011
25	30.38824	0.00000	0.00010
26	30.38807	-0.00004	0.00000
27	30.38808	-0.00001	0.00005
28	30.38811	0.00000	-0.00003
29	30.38802	0.00000	0.00001
30	30.38811	0.00000	0.00005

## APPENDIX E

### LABVIEW PROGRAM SCREENSHOTS

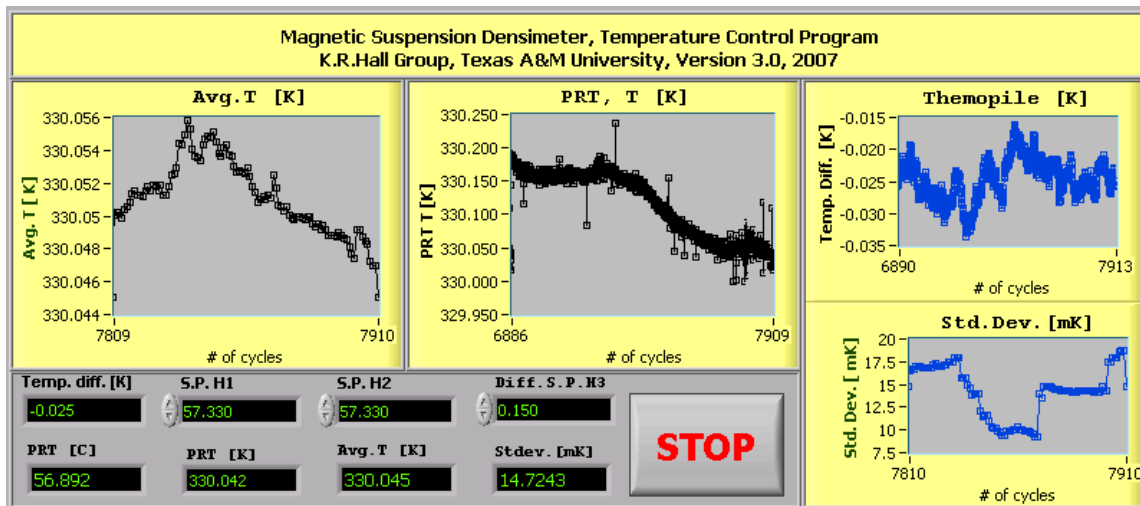


FIGURE E.1. Temperature control program screenshot.

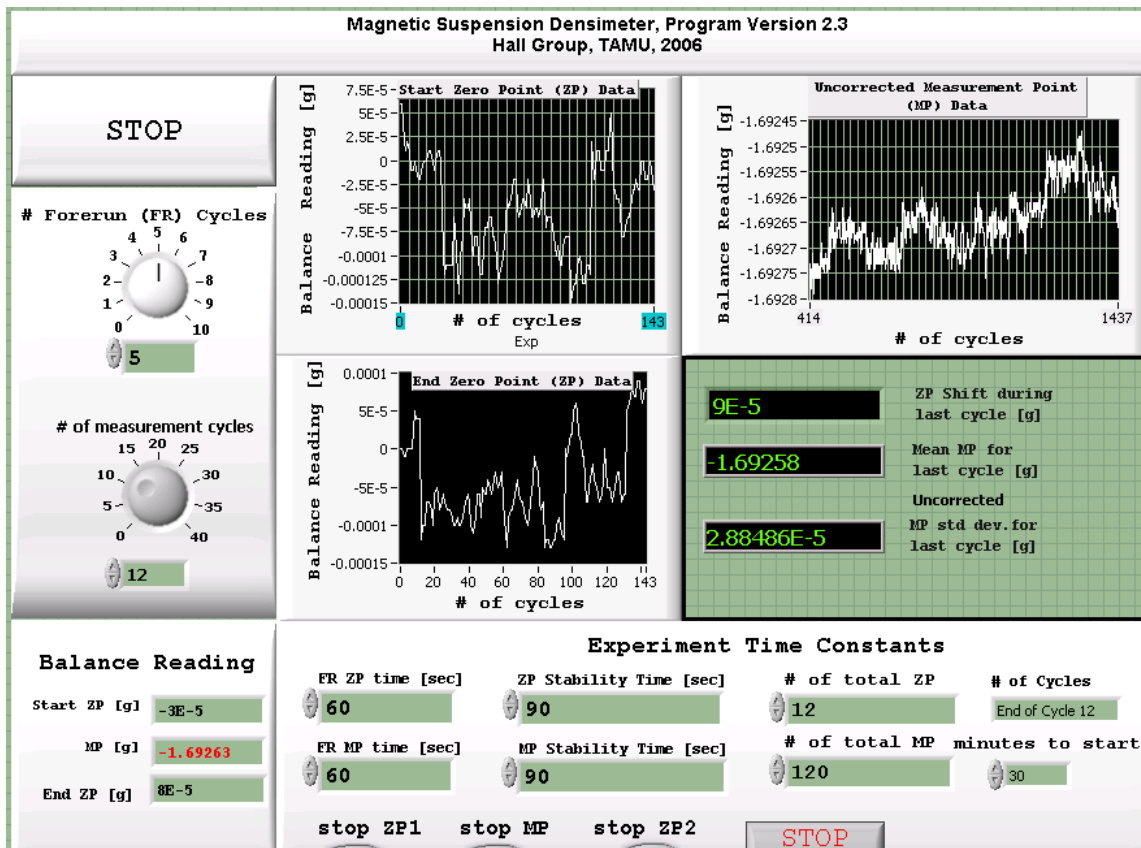


FIGURE E.2. Automatic balance control and data acquisition program screenshot.



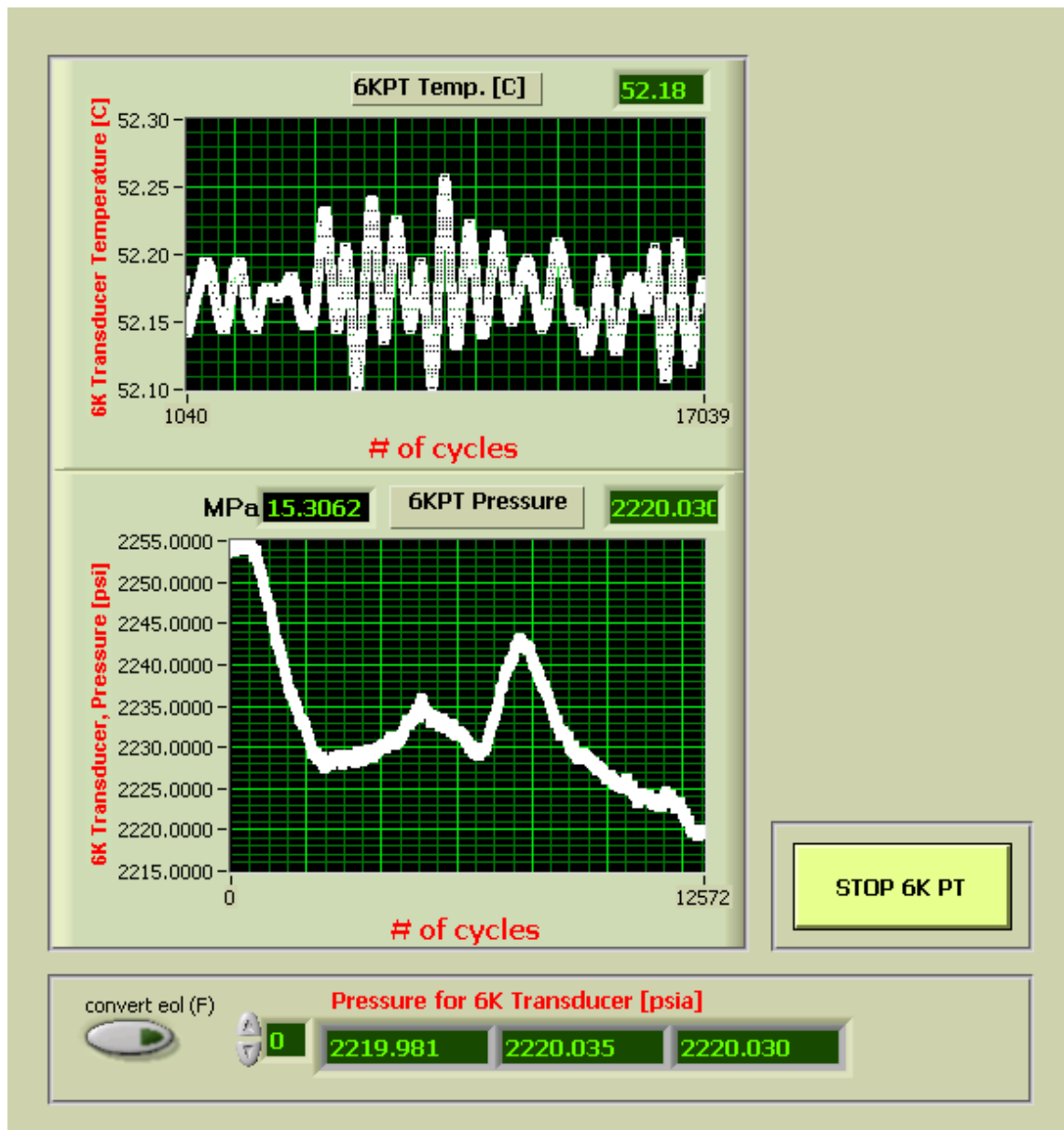


FIGURE E.3. Pressure transducer program screenshot.

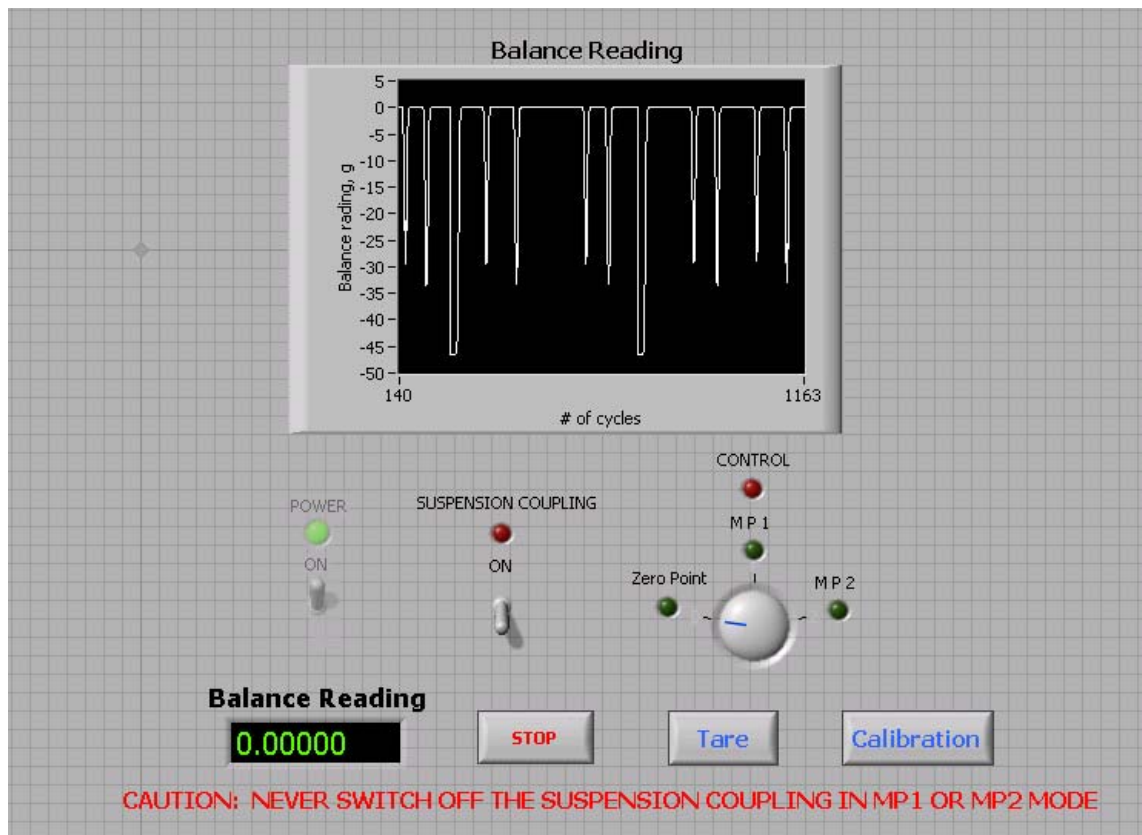


FIGURE E.4. Manual balance control program screenshot.

## APPENDIX F

### TOTAL UNCERTAINTY ANALYSIS FOR DENSITY MEASUREMENTS

The total error in density measurements is a combination of random errors and systematic errors. Uncertainty in pressure and temperature measurement, molar compositional analysis (in case of a mixture), and measurement of sinker mass under vacuum and at pressure contribute to random error. Systematic error is caused by uncertainty in sinker volume. This includes uncertainty in sinker volume determination at a reference temperature and pressure, as well as uncertainty in the functional dependence of sinker volume on temperature and pressure. Force transmission error also contributes to systematic error.

The random error in density caused by pressure, temperature and composition can be expressed as:

$$\Delta \rho = \left\{ \left[ \left( \frac{\partial \rho}{\partial P} \right)_{T,x} \Delta P \right]^2 + \left[ \left( \frac{\partial \rho}{\partial T} \right)_{P,x} \Delta T \right]^2 + \sum_{i=1}^C \left[ \left( \frac{\partial \rho}{\partial x_i} \right)_{P,T,x_{j \neq i}} \Delta x_i \right]^2 \right\}^{1/2} \quad (\text{F.1})$$

where C is the number of components.

The following procedure should be used for error analysis:

1. Convert experimental isotherms of density data to density at nearest round figures of pressure and temperature using any EOS as temperature and pressure deviations are very small. These temperatures and pressures will serve as reference; i.e. densities at all near-by pressures and temperatures will be converted to densities at this pressure and temperature.

2. At each isotherm, get a functional relationship between  $\rho$  vs.  $P$  and calculate the derivative at each value of  $P$ . This will give us  $\left(\frac{\partial \rho}{\partial P}\right)_{T, m_v, m_a, x}$  at each experimental point.
3. Similarly, at each isobaric point, get the functional relationship between  $\rho$  vs.  $T$  and calculate the derivative at each value of  $T$ . This will give us  $\left(\frac{\partial \rho}{\partial T}\right)_{P, m_v, m_a, x}$  at each experimental point.
4. For original composition of gas, calculate the densities at all temperatures and pressures using any good EOS (GERG02 or AGA8-DC92 or Peng-Robinson). Then, very slightly change the composition of only one component and normalize so that  $\sum x_i = 1$ . Calculate the densities again using the EOS. Change the composition of the same component again and calculate densities. Repeat the steps, say six times. Now we have, for each set of pressure and temperature points, seven densities (including that of original composition). Similar to step 2 and 3, calculate  $\left(\frac{\partial \rho}{\partial x_i}\right)_{P, T, m_v, m_a, x_{j \neq i}}$  for each set of temperature and pressure point.
5. Repeat steps 4 for all other components in the mixture, one at a time.
6. As supplied by the manufactures:  $\Delta T = 10$  mk,  $\Delta P = 0.02$  %\* Full Scale = 1.2 psi for 6,000 psi transducer.  $\Delta x_i$  is found from calibration certificate supplied by DCG Partnership and Accurate Gas Products.

We did an uncertainty analysis for a natural gas mixture sample that was previously studied by Patil [22]. Table F.1 shows the mixture compositions and component uncertainties provided by the supplier. We did uncertainty analyses on our pressure and temperature measurements and mixture composition as well. Uncertainties caused by temperature and pressure measurements are given in figure F.1 and figure F.2 respectively.

TABLE F.1

M91C1 mixture composition and component uncertainties.

Compound	Final Concentrations*
Nitrogen	2.031±0.000552
Carbon Dioxide	0.403±0.000351
Methane (UHP)	90.991±0.0960
Ethane (UHP)	2.949±0.0512
Propane	1.513±0.000349
Iso-Butane	0.755±0.000266
N-Butane	0.755±0.000264
Iso-Pentane	0.299±0.000212
N-Pentane	0.304±0.000214

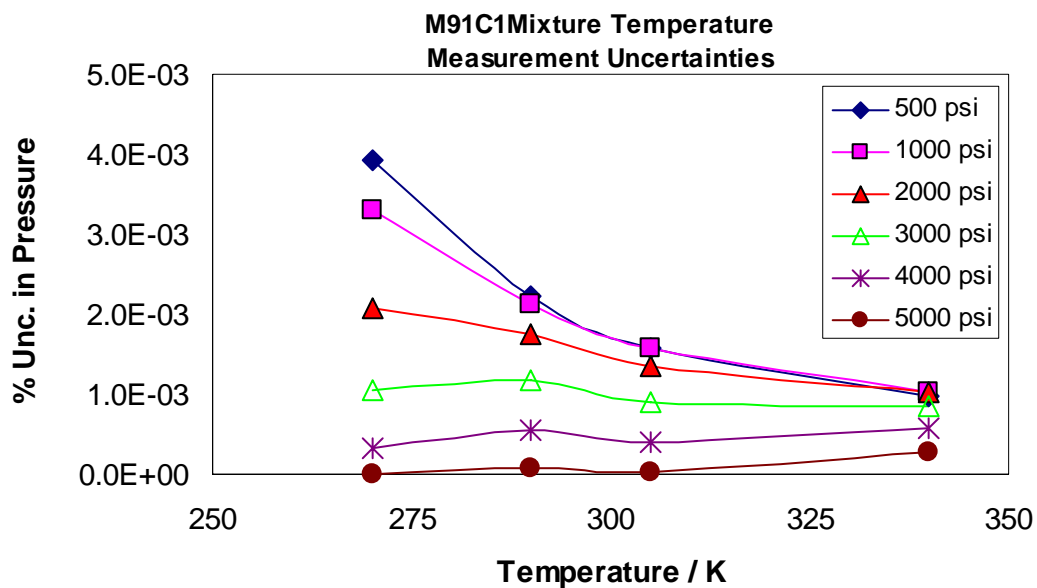
\* Component uncertainties are given as  $3\sigma$ .

FIGURE F.1. M91C1 mixture measurements uncertainties due to temperature.

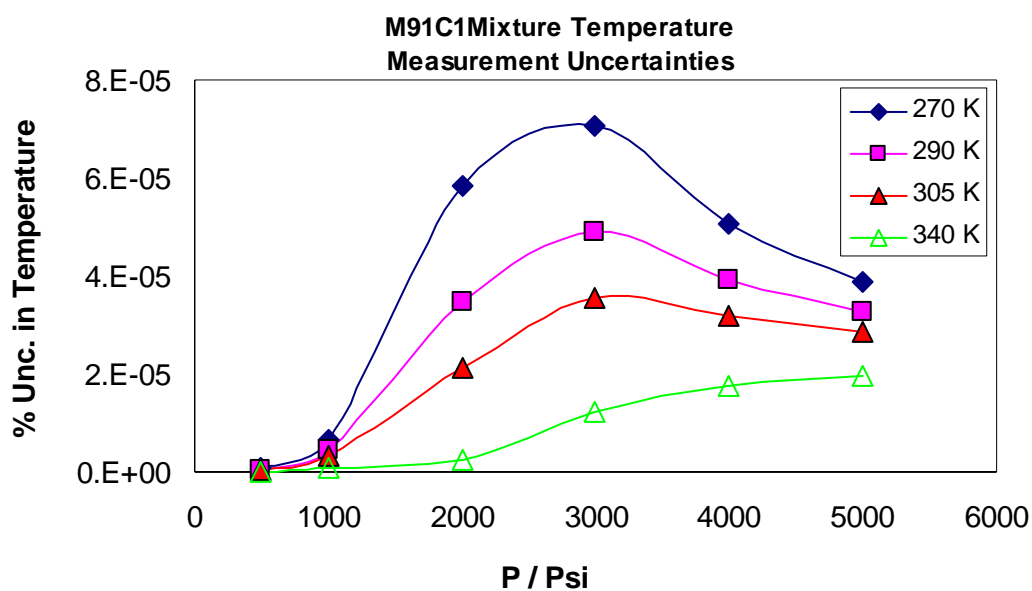


FIGURE F.2. M91C1 mixture measurements uncertainties due to pressure.

TABLE F.2

Percentage uncertainty due to temperature, pressure and compositions.

	T/P	500	1000	2000	3000	4000	5000
<b>AGA8</b>	<b>270</b>	0.053865	0.065012	0.07618	0.057918	0.047555	0.042157
	<b>290</b>	0.050435	0.057119	0.067728	0.058612	0.049305	0.043688
	<b>305</b>	0.048486	0.05354	0.062108	0.057485	0.049852	0.044409
	<b>340</b>	0.046237	0.048637	0.053722	0.05319	0.049265	0.045059
<b>PR</b>	<b>270</b>	0.054276	0.064227	0.069219	0.055102	0.04685	0.042083
	<b>290</b>	0.050896	0.057169	0.063221	0.055084	0.048122	0.043377
	<b>305</b>	0.049046	0.053758	0.059138	0.054295	0.04828	0.043922
	<b>340</b>	0.046624	0.049058	0.052493	0.051013	0.047547	0.044321
<b>GERG</b>	<b>270</b>	0.053441	0.063915	0.074877	0.056377	0.045931	0.040459
	<b>290</b>	0.050151	0.05659	0.066898	0.057581	0.048231	0.04248
	<b>305</b>	0.04831	0.053182	0.061677	0.056906	0.048988	0.043454
	<b>340</b>	0.046182	0.048463	0.053722	0.052984	0.048754	0.04458

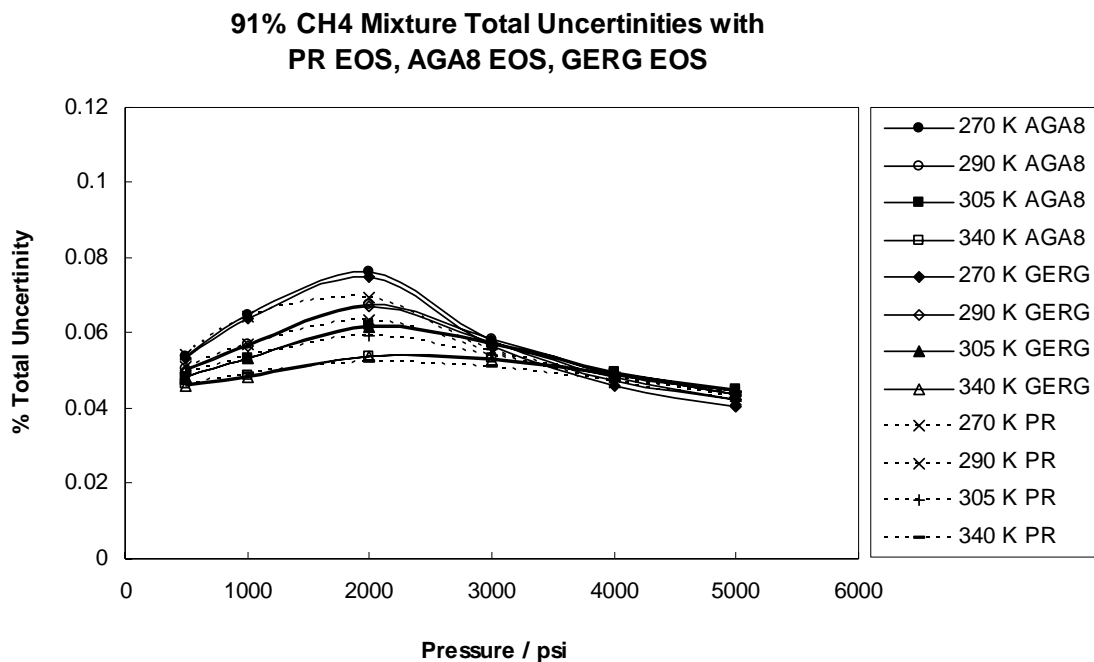


FIGURE F.3. M91C1 percentage uncertainty caused by temperature, pressure and compositions.

The total uncertainty caused by the balance, force transmission error and sinker volume, as a function of temperature and pressure is

$$u(k=2) = \left\{ 25^2 + \left[ 2 \cdot 10^{-7} \cdot T^2 - 0.0001 \cdot T + 0.0159 \right]^2 + [1.25p]^2 \right\}^{0.5} (\text{ppm})^{-1} \\ + \left[ 0.0018 + 4.45 \cdot 10^{-6} (T - 293.15) \right] (\text{kg} \cdot \text{m}^{-3})^{-1}$$

The uncertainty caused by the MSA and balance, such as sinker volume, balance weighings, force transmission error, etc are shown in table F.3.

TABLE F.3

Uncertainties due to MSA and balance such as sinker volume, balance weighings, etc.

	Temperature		
	264.8 K	293.15 K	350 K
Random scatter in weights	10 $\mu\text{g}$	10 $\mu\text{g}$	20 $\mu\text{g}$
Balance linearity	3 $\mu\text{g}$	3 $\mu\text{g}$	3 $\mu\text{g}$
Drift in mass of sinker	15 $\mu\text{g}$	15 $\mu\text{g}$	15 $\mu\text{g}$
<i>Relative Errors</i>			
Sinker volume @ reference T = 293.15 K	19 ppm	19 ppm	19 ppm
Sinker volume As $f(T)$ , P = 0.1 MPa	300 ppm	0	200 ppm
Average fluid specific Force Transmission Error	4 ppm	36 ppm	101 ppm
Sinker volume As $f(T)$ , P = 35 MPa	44 ppm	44 ppm	44 ppm
<i>Balance Calibration and non linearity minimization</i>			
Uncertainty in sinker mass	1 ppm	1 ppm	1 ppm
Uncertainty in Ti and Ta weights	5 ppm	5 ppm	5 ppm



## VITA

Mert Atilhan is a son of Atilla Atilhan, Nefise Muzaffer Atilhan and younger brother of Cevat Rifat Atilhan.

He received his Bachelor of Science degree in Chem. Eng. from Ege University, Turkey in 2002 with highest undergraduate GPA. He was admitted to Texas A&M University, College Station for his Master of Science degree in 2002. He received the Master of Science degree in Chem. Eng. from Texas A&M University in 2004. Later he enrolled in the PhD program in the Department of Chem. Eng. at Texas A&M in 2004. He completed the PhD program in the summer of 2007.

His research area includes high accuracy thermophysical properties measurements of gas mixtures and theoretical studies on developing equation of state for natural gas custody transfer.

Mert is married with Selma Atilhan. His wife is also pursuing a PhD degree in the Department of Chemical Engineering at Texas A&M University.

His permanent address in Turkey is:

1738 Sokak, No:134

Daire:6, Sefa Apt.

Karsiyaka, Izmir, TURKEY

PK: 35540

Phone: +90-532-446-8781

In the USA, he can be reached through Dr. Kenneth R Hall, Department of Chemical Engineering, Texas A&M University, College Station, TX 77843-3122.